LIGHT PROPAGATION IN MULTILAYER METAMATERIALS

Cover: A ray tracing image of a metal dielectric multilayer structure and a glass sphere, formed by hypothetical negative index glass. At the back are two glass spheres, one with a positive index (left) and one with a negative index (right).

Ph.D. Thesis University of Amsterdam, September 2015
Light propagation in multilayer metamaterials
Ruben Cornelis Maas

ISBN 978-90-77209-93-6

A digital version of this thesis can be downloaded from http://www.amolf.nl.

LIGHT PROPAGATION IN MULTILAYER METAMATERIALS

Lichtpropagatie door multilaag-metamaterialen

ACADEMISCH PROEFSCHRIFT

ter verkrijging van de graad van doctor
aan de Universiteit van Amsterdam
op gezag van de Rector Magnificus
prof. dr. D.C. van den Boom
ten overstaan van een door het college voor promoties
ingestelde commissie,
in het openbaar te verdedigen in de Agnietenkapel
op 25 september 2015 te 14:00 uur

door

Ruben Cornelis Maas

geboren te Den Burg

Promotiecommissie

Promotor:	Prof. dr. A. Polman
Overige Leden:	Prof. dr. A. Alù
	Prof. dr. H. J. Bakker
	Prof. dr. T. Gregorkiewicz
	Prof. dr. J. Knoester
	Prof. dr. P. C. M. Planken

Faculteit der Natuurwetenschappen, Wiskunde en Informatica

This work is part of the research program of the 'Stichting voor Fundamenteel Onderzoek der Materie' (FOM), which is financially supported by the 'Nederlandse organisatie voor Wetenschappelijk Onderzoek' (NWO). It is also funded by the European Research Council (ERC).

Contents

1

Introduction

Light as a physical phenomenon is all around us. It is used to observe our surroundings, it is applied in long-range telecommunications, it forms the largest renewable energy resource available to us. In all applications, the interaction between light and matter is crucial. A transparent dielectric material such as glass is a typical example of a material that is used to engineer the phase fronts and propagation direction of light. This control over light has enabled us to fabricate a wide variety of optical elements such as lenses, optical fibers and prisms.

These optical elements rely on the fact that light propagates through the dielectric medium with a velocity lower than the speed of light in vacuum, as dictated by the material refractive index. At the smallest length scales, materials are built up from atoms. A wave of light interacts with an atom by coupling between the oscillating electromagnetic field of the wave and the atomic charge distribution. The strength of this coupling is indicated by the polarizability of the material. However, due to the large characteristic length scale difference between the the atomic structure of the material and the wavelength of light, we usually treat a material as an effectively homogeneous slab described by a refractive index. Glass typically has a refractive index of around $n = 1.5$. A material with one of the lowest refractive indices known is magnesium fluoride, at $n = 1.37$. Semiconductors are typically characterised by a higher refractive index, such as $n = 4.5$ for silicon, but this high refractive index is often accompanied with strong absorption of light. One of the main reasons why glass is used in so many different optical elements is its extremely low absorption, allowing for instance propagation through glass optical fibers with an attenuation of only 0.2 dB/km.

Our ability to manipulate light was originally limited to naturally occurring materials. However, as light can be described as a propagating wave, it was soon

realized that by structuring materials on a length scale larger than the atomic (Angstrom) length scale, but equal to or below the wavelength of light, novel interactions between light and materials can be achieved. One of the first examples was the design of a new type of radio wave antenna, in which the antenna was built up from closely spaced metal plates [1]. Such structures, then called "artificial dielectrics", were used to create an effective medium which showed a refractive index smaller than unity [2].

These demonstrations were designed to operate for radio waves, with a typical wavelength in the centimeter or meter range. Because of this long wavelength, fabricating sub-wavelength features in the material was still relatively straightforward. The recent advances in nanofabrication, primarily in electron beam lithography and focussed ion beam milling, have enabled a spectacular scaling down of the typical dimensions at which materials can be structured. These advances have been primarily driven by the semiconductor industry, in its efforts to fabricate smaller transistors and memory elements. Today, the minimum achievable feature size has reached the nanometer length scale. This has enabled the fabrication of structures with features which are sub-wavelength for visible light. Apart from improved top-down fabrication techniques, a large effort has been devoted to developing self assembly driven, bottom-up fabrication techniques. One specific example of bottom-up fabrication is called DNA origami [3], where DNA molecules are folded in a controlled manner, enabling the fabrication of a structure with a tailored optical response [4].

Such artificially structured materials are called metamaterials. Here meta, from the Greek word for "beyond", implies that structuring a material on a scale below the wavelength of light can lead to new effective properties beyond those found in natural materials. One example of such an effective property is a negative refractive index. In the 1960's [5], the Russian scientist Veselago considered how light would propagate through a negative-index material. This negative-index material was supposed to have a negative permittivity and a negative permeability. He found that a slab of such a material would act as a flat lens, creating an image of an object without using curved surfaces, but taking advantage of negative refraction. In 1999, the British theoretical physicist John Pendry showed two possible practical designs how to fabricate metamaterials with a negative magnetic permeability, which opened a practical route towards the realization of negative-index metamaterials. One geometry was the split ring resonator design shown in Figure 1.1a. This original work [6] inspired a large research effort by many groups all over the world.

The first experimental demonstration of a negative-index metamaterial was in the GHz range [7]. Here, the dimensions of the unit cell, formed by a metallic wire lattice combined with split ring resonators, were chosen such that the effective permittivity and permeability of this metamaterial were negative in the same frequency regime, leading to a negative effective index. This was experimentally verified by measuring the refraction angle from a prism constructed from this metamaterial [8]. Since then, advances in fabrication techniques and design of metamaterials have led to the demonstration of negative-index metamaterials also in the

infrared [9, 10], and the near-infrared [11].

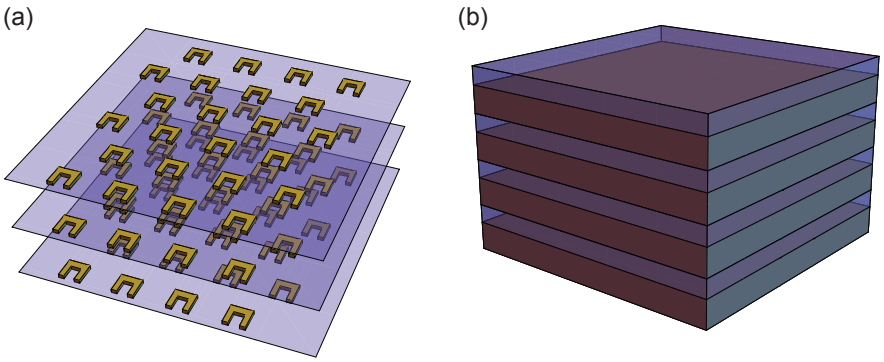

Figure 1.1: a, Sketch of a split ring resonator metamaterial operating in the near-infrared and at longer wavelengths. **b**, 3D Metal-dielectric coupled waveguide metamaterial operating in the UV and visible spectral range.

Obviously, fabrication of a three-dimensional metamaterial composed of resonant nanostructures becomes much more challenging as the wavelength of operation is reduced [12]. Furthermore, optical losses due to Ohmic dissipation strongly increase for shorter wavelength. As a result, practical metamaterials based on the split-ring resonator design in the UV/visible spectral range have not been realized. One solution is to limit the sub-wavelength structures to a single interface, as is done in the field of metasurfaces, which have demonstrated interesting phenomena such as anomalous refraction [13], wavefront shaping [14] and three-dimensional holography [15].

A new method to realize metamaterials at high frequencies uses a fundamentally different design, based on coupled plasmonic waveguides. A metal-dielectric interface supports guided waves, formed by longitudinal charge density oscillations in the metal, called surface plasmon polaritons (SPPs) [16]. Such SPPs are characterized by a specific propagation constant and lateral field profile. Away from the interface the fields decay exponentially. If two metal-dielectric interfaces are brought in close vicinity, the SPPs travelling over the two surfaces can couple, to form symmetric or anti-symmetric SPP waves. A dielectric core cladded by metal then acts as a waveguide [17]. Because part of the field of the waveguide mode overlaps with the metal regions, which are characterized by a negative permittivity (in a certain spectral range), completely new propagation characteristics can be achieved, such as propagation with a negative modal index [18]. Such a negative-index waveguide mode has been experimentally observed in a 2D planar geometry [19], and the dispersion of different coupled plasmonic waveguide geometries has been systematically studied theoretically [20].

The waveguide geometries considered above consisted of two-dimensional de-

signs, where light is guided along two coupled interfaces. To achieve a 3D metamaterial at first sight these 2D waveguides seem unsuited as building blocks. It was realized however, that by closely stacking multiple metal-dielectric-metal waveguides onto each other and by engineering the adjacent coupling, also propagation of light in the third dimension can be achieved [21], rendering the coupled waveguide geometry a three-dimensional metamaterial. In fact, it was shown that by appropriate design of the unit cell geometry, the propagation constant can be made negative for TM-polarization and for all angles of propagation in the metamaterial. Such a multilayer structure then acts as a 3D metamaterial with a negative effective index.

The multilayer design has several advantages. First of all, the fabrication of the geometry is relatively straightforward. The deposition of thin films is a process that can be routinely carried out in a cleanroom facility, using thermal evaporation, sputter coating or atomic layer deposition. Furthermore, because light is no longer coupled to a localized resonance but rather a waveguide mode that resides mainly in the dielectric film, losses can be significantly reduced [21, 22]. Finally, due to the metal-dielectric-metal waveguide mode dispersion, the geometry can be engineered to exhibit a negative-index mode at very high frequencies [20], operating in the blue or ultraviolet spectral range. Figure 1.1b shows a sketch of the multilayer design.

While the coupled waveguide design enables 3D isotropic properties, the same geometry also enables optical properties which are strongly anisotropic when different layer thicknesses are considered. Taking advantage of the structural asymmetry in metal-dielectric waveguides, such geometries have been used in the realization of hyperbolic metamaterials [23, 24]. Hyperbolic metamaterials are artificial materials where the permittivity is described by a tensor; the permittivity along the longitudinal directions (parallel to the waveguides) has an opposite sign to the permittivity in the lateral direction (normal to the waveguides). This response is realized in 3D metal dielectric waveguide arrays, where light propagating as a waveguide mode along the interfaces probes a different effective permittivity than light propagating normal to the interfaces in the form of a Bloch wave. Hyperbolic metamaterials have unique features, such as a very high local density of optical states [25] and can serve to enhance the radiative decay of localized emitters [26]. They enable the conversion of evanescent waves in air to propagating waves, a feature that has been exploited to create hyperlenses, which are able to resolve sub-diffraction limit features in the far-field [27, 28].

1.1 Wave vector diagrams

In the description of wave propagation through a multilayered medium, a comprehensible way of presenting the directions of propagation is the wave vector diagram [29]. In such a diagram, the allowed combinations of wave vectors are shown at one frequency. Therefore these diagrams are referred to as isofrequency contours (IFCs). For the 3D planar designs considered here, only two wavevector directions

must be considered, by symmetry. Figure 1.2a shows a wave vector diagram for homogeneous media, for which the dispersion relation is: $n^2 k_0^2 = k_x^2 + k_z^2$ in the two-dimensional plane considered here, with $k_0 = 2\pi/\lambda_0$, where λ_0 is the free-space wavelength. The IFC is calculated for $\lambda_0 = 364$ nm. The inner green circle refers to wave propagation in air, $n = 1$. The outer green circle corresponds to propagation through a $n = 1.5$ material, such as glass. The red and blue circles are IFCs for slightly red and blue shifted frequencies. The IFC is a circle as light propagates with the same wave vector in all directions in a homogeneous medium. Increasing (decreasing) the frequency leads to a larger (shorter) wave vector.

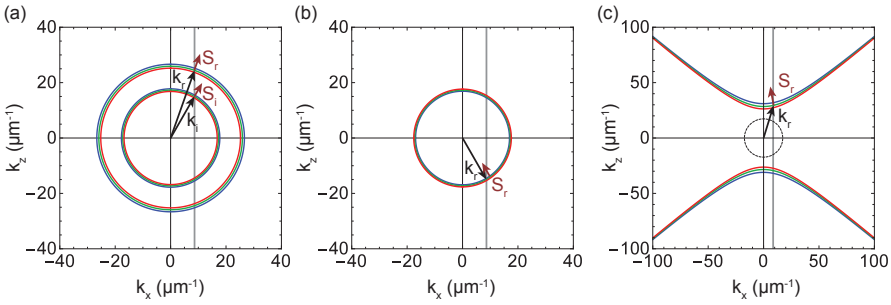

Figure 1.2: **a**, Wave vector diagram showing the isofrequency contours for two homogeneous media. The inner green circle refers to light propagation with a wavelength of $\lambda_0 = 364$ nm ($k_0 = 17.3\ \mu m^{-1}$) through air. The outer green circle refers to propagation through a medium with $n = 1.5$. The vertical gray line indicates the parallel wave vector momentum k_x of a plane wave with an angle of incidence in air of 30 degrees. The red and blue circles correspond to a small modulation to lower frequencies (red) and higher frequencies (blue). Refraction at an interface between air and an $n = 1.5$ medium can be constructed using this diagram. **b**, The isofrequency contour corresponding to a homogeneous negative-index material. The red and blue circles are inverted when compared to (a), and the Poynting vector is now oriented inward. As the direction of the z component of the Poynting vector is preserved, the x component changes sign, corresponding to negative refraction. **c**, IFC for a hyperbolic metamaterial. This metamaterial supports very high wavevectors, and the refracted Poynting vector S_r exhibits negative refraction.

The refraction of a plane wave at an air/glass interface can easily be constructed from such a wavevector diagram. The incident plane wave, propagating in the positive z direction, is described by an incident wavevector k_i and Poynting vector S_i, which are colinear in a lossless, homogeneous medium. At the interface, the parallel wavevector momentum k_x is conserved, as indicated by the vertical gray line in Fig. 1.2a. The intersection between this line and the outer circle determines the refracted wavevector in glass. Note that there are two intersections between the outer circle and the line of conserved k_x, which correspond to upward and downward propagating waves. The direction of energy propagation will determine which solution is valid. The incident plane wave has a positive vertical component

of S_i, meaning light propagates in the positive z direction. The group velocity is given by $v_g = \partial\omega/\partial k$, and in the absence of losses, it can be shown that the group velocity is equal to the energy velocity $v_g = v_e$ [30]. The energy velocity is colinear with the Poynting vector, which represents the energy flux direction. Therefore, the orientation of the Poynting vector will be normal to the tangent of the wavevector diagram, oriented towards IFCs corresponding to higher frequencies. Based on this, we see that for the case of a normal dielectric interface in Fig. 1.2a the Poynting vector is oriented outwards, and light propagation in the dielectric is described by the top intersection between the line of conserved k_x and the outer IFC, as there the vertical component of S_r is positive.

Next, we use the wavevector diagram to consider light propagation through a metamaterial with an isotropic negative index ($n = -1$), such as the coupled waveguide geometry proposed in [21]. Figure 1.2b shows the IFC for this metamaterial. The radius for the IFC is the same for the metamaterial and vacuum. However, the IFCs for the higher (blue) and lower (red) frequencies are now inverted. This means that the Poynting vector is now oriented inwards. Following the same construction as in Fig. 1.2a, with the incident light again propagating in the positive z direction, the correct solution for k_r is now the bottom intersection between the IFC and the line of conserved k_x (gray), as in that case S_r is oriented in the positive z direction. This means k_r and S_r are anti-parallel, as sketched in the figure. As a consequence, this structure exhibits negative refraction, since the x-component of S changes sign over the interface.

Fig. 1.2c shows the wavevector diagram of a hyperbolic metamaterial (HMM). This IFC is clearly very different from the homogeneous structures considered in Figs. 1.2(a,b). Similar to the homogeneous metamaterial in Fig. 1.2b, the hyperbolic geometry shows negative refraction of energy as indicated by the fact that the Poynting vector in the metamaterial S_r points in the negative x-direction. However, the wave vector k_r is not anti-parallel with S_r, in contrast to the case in Fig. 1.2b. Hyperbolic metamaterials allow wavevectors with a very large magnitude, that carry very fine spatial details, enabling the fabrication of hyperlenses, which resolve features which are sub-diffraction limit [27, 28]. Another remarkable feature of these HMMs is that at high wavevectors, all waves propagate in the same direction, normal to the hyperbole, as indicated by S_r.

1.2 Outline of this thesis

In this thesis, we study the design and experimental realization of 3D metal-dielectric multilayer metamaterials. The goal of this research is to achieve fundamental insight in wave propagation in these metamaterials, to fabricate them, to experimentally determine their effective properties, and to apply these novel properties to demonstrate a flat lens. The following chapters present the results of this research.

Chapter 2 describes a multilayer metamaterial composed of a stack of thin Ag

and SiN multilayers. We determine the effective permittivity of this metamaterial from interferometric transmission measurements. In this experiment, light propagates along the waveguides, probing the negative permittivity of the metal and the positive permittivity of the dielectric. By changing the filling fraction of Ag in the unit cell, we tune the effective permittivity. We use this tunability to create a metamaterial of which the permittivity, or epsilon, crosses zero at a desired wavelength in the visible. Epsilon-near-zero (ENZ) metamaterials have the unique feature that light propagates with no phase advance through the material. We investigate the range of unit cell sizes for which this metamaterial can be fabricated, and study the angular response of the ENZ metamaterial.

In Chapter 3 we study how light propagates through a periodic metal dielectric multilayer structure, focussing on the Bloch-wave solutions to the wave equation in the z direction. We study the effective optical properties of a metal dielectric multilayer structure with an isotropic negative index for the fundamental Bloch harmonic. We find that most of the energy is carried by a higher order, positive index harmonic. The theoretical findings are corroborated by a metamaterial prism refraction experiment, where the prism is sculpted from a Ag/TiO_2 multilayer stack using focussed ion beam milling.

In Chapter 4 we demonstrate a flat lens, fabricated from a Ag/TiO_2 multilayer. Due to negative refraction of energy, light from an object is focussed by a flat slab of such a material. Rather than using the double-periodic structure that has first been proposed to fabricate a flat lens, we show that by appropriately designing a single-periodic metal dielectric multilayer structure, an angle-independent effective negative index response can be achieved. Confocal transmission microscopy and near-field scanning optical microscopy are used to experimentally characterize the image formed by the flat lens.

While the Chapters 2-4 focussed on the propagation of light inside the metamaterial, Chapter 5 addresses the coupling efficiency of light into a metal-dielectric waveguide array metamaterial. Due to the large mismatch between the spatial field distribution of the incident plane wave and the complex field profiles in the metamaterial, light incoupling is normally quite inefficient. We design a dielectric coupling metamaterial that transforms the incident plane wave to a symmetric waveguide mode with strong field gradients. By controlling the relative position of the coupling metamaterial with respect to the waveguide array and by optimizing the coupling metamaterial dimensions, we achieve perfect coupling to an antisymmetric waveguide mode, which would not be excited by a plane wave without the coupling metamaterial. We show that even up to very large angles of incidence, a large fraction of incident light can be efficiently coupled into the waveguide mode of interest by appropriately designing the coupling metamaterial.

Chapter 6 discusses potential applications of the multilayer metamaterial design described in this thesis. We propose a flat lens for the near-infrared telecom wavelength band, and discuss an electrically tunable flat lens. We show that a hyperbolic metamaterial combined with a special cavity design creates a wave-attracting cavity resonance at optical frequencies. We describe how for circularly

polarized light the plasmonic spin-Hall effect could be exploited to achieve a deterministic wave attractor for arbitrary light emission around the cavity. Finally, we show how a dielectric multilayer structure can act as an angular filter, and how this can be used to control the emission characteristics of light-emitting diodes.

Overall, this thesis describes the effective optical properties of metamaterials formed by multilayer structures. Propagation of light through very thin metallic and dielectric layers exhibits unexpected behaviour, which we study using analytical calculations and numerical simulations. Based on this, we fabricate samples using cleanroom techniques, and characterize the effective optical response using phase-sensitive transmission measurements, angular refraction experiments and by confocal and near field microscopy. The results of these measurements help us further understand the interaction between light and new metamaterials, designed to operate in the UV and visible spectral range.

2

Experimental realization of an epsilon-near-zero metamaterial at visible wavelengths

Optical materials with a dielectric constant near zero have the unique property that light advances with almost no phase advance. Although such materials have been made artificially in the microwave and far-infrared spectral range, bulk threedimensional epsilon-near-zero (ENZ) engineered materials in the visible spectral range have been elusive. Here, we present an optical metamaterial composed of a carefully sculpted parallel array of subwavelength silver and silicon nitride nanolamellae that shows a vanishing effective permittivity, as demonstrated by interferometry. Good impedance matching and high optical transmission are demonstrated. The ENZ condition can be tuned over the entire visible spectral range by varying the geometry, and may enable novel micro/nanooptical components, for example, transmission enhancement, wavefront shaping, controlled spontaneous emission and superradiance.

2.1 Introduction

Optical metamaterials have been the topic of intense study in recent years because they enable the realization of optical properties that do not occur in natural

materials. Metamaterials are composed of elements with subwavelength scales in one or more dimensions. For this reason, metamaterials have been studied in the microwave spectral range, where index near-zero [31] and epsilon-near-zero (ENZ) behaviours have been predicted theoretically [32–34] and demonstrated experimentally [35–40]. With the appearance of advanced ion- and electron-beam nanolithography methods, the realization of ENZ metamaterials in the visible spectral range has now come within reach. Recently, a one-dimensional waveguide nanochannel with ENZ behaviour was demonstrated in the visible [41]. If three-dimensional ENZ metamaterials could be made in the visible, entirely new forms of waveform shaping [33, 42], light tunnelling [34] and spontaneous emission enhancement [43] would become possible over this technologically important spectral range.

Here, we present a metamaterial design composed of alternating layers of Ag and SiN with subwavelength layer thicknesses (Fig. 2.1, inset). This geometry has been studied previously to construct hyperbolic wavevector diagrams and increase the photonic density of states [23, 25, 44–46]. In the limit of deep subwavelength layer thicknesses, and for transverse electric (TE) polarized light (that is, the electric field parallel to the waveguides), the effective permittivity of this metamaterial equals the geometrically averaged permittivity [23], $\epsilon_{\mathrm{av}} = \rho\epsilon_m + (1-\rho)\epsilon_d$, where ρ is the metal filling fraction and ϵ_m and ϵ_d are the permittivity of metal and dielectric, respectively. Figure 2.1a shows experimentally determined values of the real (ϵ', solid lines) and imaginary (ϵ'', dashed lines) values of the permittivity for a thin Ag layer. The plot for ϵ' demonstrates the well-known decreasing trend towards strongly negative values due to the Drude-type response of free electrons in metal at long wavelengths. The effective permittivity of SiN is also shown in the figure and is positive and only slightly dispersive. The imaginary part of the permittivity of both Ag and SiN is measured to be very small over the entire visible range (Supplementary section "Ellipsometry").

Figure 2.1b shows the calculated effective permittivity for TE polarized light for a metamaterial composed of deep subwavelength Ag and SiN layers with ρ = 20, 30 and 50 %, based on the optical constants in Fig. 2.1a. With these metal filling fractions, the ENZ condition occurs at λ = 662, 545 and 428 nm, respectively, demonstrating the ENZ condition can be controlled over a broad spectral range by varying the composition. At the same time, the imaginary part of the effective permittivity ϵ'' is close to zero (< 0.2) over the entire visible range, indicating low loss.

The permeability of the metamaterial is assumed to be unity throughout the entire visible spectrum, as there is no magnetic resonance in the system. This means that when ϵ' = 1 the metamaterial is completely matched to free space, and almost no light would be reflected. Figure 2.1b shows that the wavelength at which this condition is met can be tuned throughout the visible range by varying ρ. As an example, for ρ = 30% we find ϵ' = 1 at λ = 491 nm. Interestingly, the losses are relatively low in this case (ϵ'' <0.1), even though a significant portion of the metamaterial consists of metal, and the optical frequency is quite close to the bulk

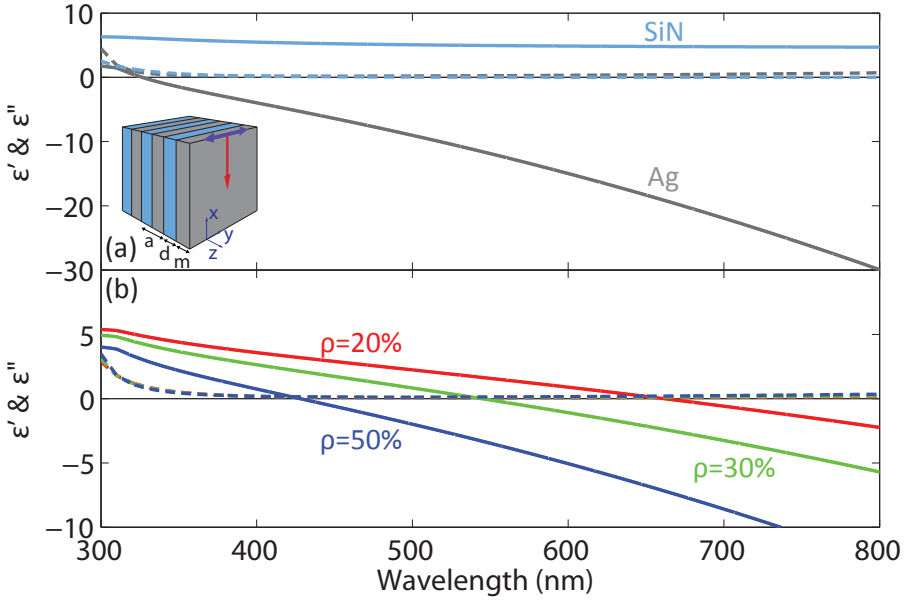

Figure 2.1: Metamaterial optical constants. **a**, Measured real (ϵ', solid line) and imaginary (ϵ'', dashed line) permittivity of Ag (grey) and SiN (blue). Inset: schematic of the multilayered metamaterial structure composed of Ag and SiN layers (a, d and m are unit cell dimension and dielectric and metal layer thicknesses, respectively). Light is incident along the x-direction and polarized along the y-direction. The dashed lines for Ag and SiN coincide. **b**, Effective permittivity of an Ag/SiN multilayered metamaterial with metal filling fraction ρ = 20% (red), 30% (green) and 50% (blue), calculated using an effective medium approximation. The real (ϵ', solid lines) and imaginary (ϵ'', dashed lines) parts of the permittivity are shown. The dashed lines for the three filling fractions coincide.

plasma frequency of the metal.

Probing the ENZ condition on this layered metamaterial requires samples that are optically accessible along the planar layers (x-direction), which cannot be achieved using geometries made by thin-film evaporation. Here, we demonstrate a layered metamaterial architecture composed of vertically oriented parallel lamellae of Ag and SiN, fabricated from a SiN membrane using a combination of focused ion beam (FIB) milling, reactive ion etching and thermal evaporation of Ag. This configuration allows us to isolate the ENZ condition using TE polarized light. Note that TE and transverse magnetic (TM) polarized light are degenerate when incident normal to the layers. Moreover, in the latter geometry, higher order Bloch harmonics can complicate the analysis. Figure 2.2a shows a top-view scanning electron micrograph (SEM) of a completed metamaterial sample (see Supplementary section "Fabrication", for more details). The 8 μm × 8 μm

waveguide arrays are highly regular, and the Ag and SiN layers are clearly visible as bright and dark bands, with layer thicknesses of 110 nm and 130 nm, respectively. A cross-section of the metamaterial structure is shown in Fig. 2.2b. The metamaterial layer can be clearly seen, on top of a remaining underlayer of SiN.

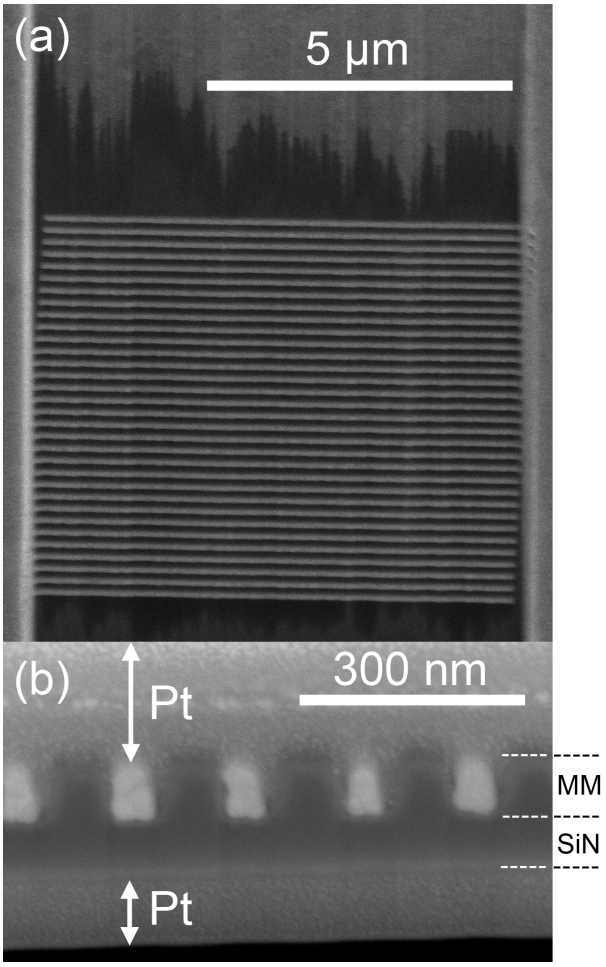

Figure 2.2: Metamaterial sample. **a**, SEM top view of the completed metamaterial structure. The Ag and SiN layers are visible as bright and dark bands, with layer thicknesses of 110 nm and 130 nm, respectively. **b**, SEM view of a cross-section showing the metamaterial (MM) layer, with alternating layers of Ag (bright) and SiN (dark), as well as a continuous SiN layer under the metamaterial. Pt layers are deposited to emphasize the top and bottom interface.

A total of 16 different multilayered metamaterial samples were fabricated. The exact waveguide dimensions, metamaterial thickness and underlayer thickness of

each sample were determined from cross-sections made using FIB. The metal layer thickness was varied from 40 to 150 nm, and the dielectric layer thickness between 36 and 135 nm. In this way, the metal filling fraction ρ was systematically varied between 30 and 80% to study its effect on metamaterial dispersion. The unit cell size was varied between 85 and 280 nm to investigate the transition from an effective medium material to that of a waveguide-based metamaterial.

2.2 Interferometric phase measurements

To determine the effective optical properties of each multilayered metamaterial, we used a specially designed Mach-Zehnder interferometer to measure the optical path length of the metamaterial structures [9] (Supplementary section "Interferometry"). The optical path length was determined from the difference between the phase of light focused through the metamaterial and light focused through an air reference hole made in the same sample.

Figure 2.3a shows the measured phase shifts for metamaterials composed of a unit cell of a thin metal layer (40, 58 nm) in combination with a thin (45 nm, blue) and thick (135 nm, red) dielectric layer, respectively. Figure 2.3b shows similar data for a thick metal layer (155 nm, 150 nm) in combination with thin (36 nm, blue) and thick (130 nm, red) dielectric layers. The experimental data, taken at seven different wavelengths, show a gradual transition from a large phase shift at short wavelengths to a small phase shift at longer wavelengths.

Figure 2.3 (solid lines) also shows finite-difference time-domain simulations (FDTD Solutions 8.0, Lumerical Solutions) of the phase shift as a function of wavelength. In these simulations, the metamaterial waveguide dimensions determined from cross sections are used to define a periodic unit cell, and the experimentally determined optical constants of Ag and SiN (Fig. 2.1a) are used, so no fitting parameters are applied. Figure 2.3 shows very good agreement between experiment and simulations for all four samples. The gradual decrease in phase shift for longer wavelengths is clearly reproduced by the simulations. Also, the distinct feature in the data around $\lambda = 480$ nm for the largest unit cell in Fig. 2.3b is well reproduced. Its origin will be discussed in the following.

To determine the effective permittivity of the metamaterial from the measured phase shift, a transfer matrix method was applied to a double-layer structure composed of the metamaterial sample and the SiN underlayer, surrounded by air. This model expresses the effective complex transmission coefficient t_{eff} of the combined metamaterial and underlayer structure in terms of their respective thickness and (effective) permittivity. The phase shift of light transmitted through the metamaterial relative to that through the reference hole $\Delta\phi = \phi_s - \phi_r$ directly follows using $\phi_s = \arg(t_{\text{eff}})$ and $\phi_r = k_0(d_s + d_{\text{SiN}})$, where k_0, d_s and d_{SiN} are the free-space wavevector, the thickness of the metamaterial sample and the thickness of the SiN underlayer, respectively. From the measured phase shift, the known thickness of metamaterial and SiN underlayer and the known permittivity of SiN, the effective

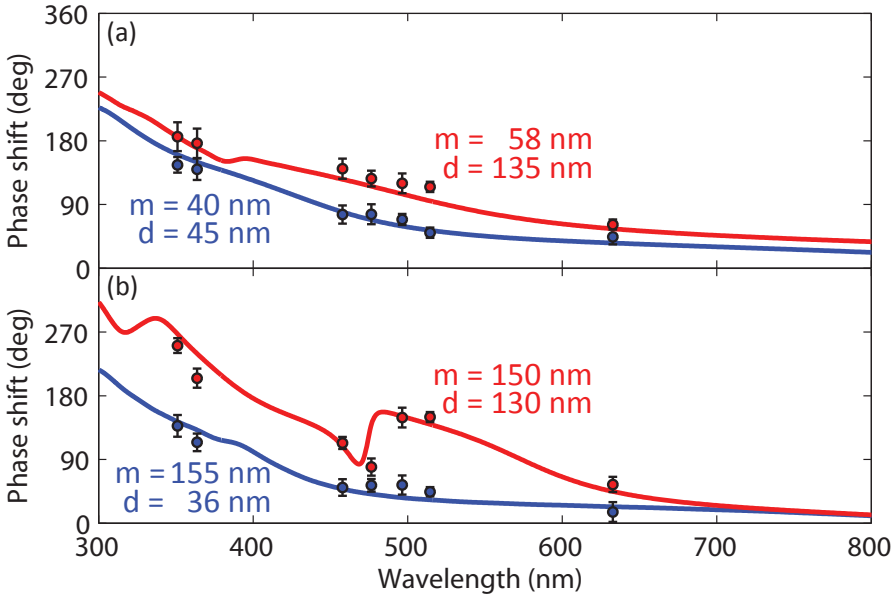

Figure 2.3: Metamaterial phase measurements. Measured (data points) and simulated (solid lines) phase shift of metamaterials with different metal (m) and dielectric (d) layer thicknesses. **a**, Thin metal layer and varying dielectric thickness. **b**, Thick metal layer and varying dielectric thickness. Error bars correspond to the standard deviation of the collection of 20 consecutive phase measurements.

permittivity of the metamaterial can be derived. This procedure is illustrated by the inset in Fig. 2.4a, which shows the phase shift calculated as described above for a metamaterial sample (d_s = 45 nm; d_{SiN} = 93 nm, in blue) at λ = 633 nm as a function of metamaterial permittivity. The imaginary part of the effective permittivity is assumed to be $\epsilon'' = 0$. The validity of this assumption is discussed in the Supplementary section "Effective permittivity". Also shown in the inset is the measured phase shift for this geometry (horizontal red line). The effective permittivity then directly follows from the intersection between the two lines. The phase shift was measured 20 times for each metamaterial sample at each wavelength, and every measured phase shift was separately converted to an effective permittivity. The mean of this distribution was taken to be the effective permittivity of the sample, with the standard deviation of the distribution an indicator for the error. For metamaterial thicknesses greater than 15 nm, using simulations, we verified that the effective permittivity is independent of thickness (Supplementary section "Thickness dependence").

2.3 Changing effective parameters

Figure 2.4a shows the effective permittivity derived in this way for three different metamaterials, with each structure having the same unit cell size of 200 nm, and the metal filling fraction varied (ρ = 30, 60 and 80%). For all filling fractions a clear trend of decreasing permittivity with wavelength is observed. The measured permittivity ranges from $\epsilon' = 6.0 \pm 1.2$ at λ = 364 nm for the lowest filling fraction to $\epsilon' = -13 \pm 3.4$ at λ = 633 nm for the highest filling fraction. Figure 2.4a also shows analytical calculations of the metamaterial effective permittivity (solid lines). This effective permittivity is determined by calculating the supported eigenmodes of a planar waveguide array using a transfer matrix formalism for a periodic unit cell [21, 29]. The eigenmodes are calculated assuming light propagation parallel to the waveguides, with the electric field parallel to the metal-dielectric interfaces (TE polarization). Only the fundamental mode (characterized by the lowest propagation losses) is assumed to contribute to wave propagation through the metamaterial. The calculations are in good agreement with the experimental trends. The strong difference in dispersion between the three geometries is also well represented by the calculations, confirming that the wavelength at which the effective permittivity of the metamaterial becomes zero can be controlled by the metal filling fraction. This cutoff condition occurs at λ = 807, 567 and 394 nm for the three geometries, respectively.

Figure 2.4b shows the measured and calculated effective permittivity of three structures with an approximately constant metal filling fraction ρ = 50%. Here, the unit cell size is varied (a = 85, 170 and 280 nm). The experimental trends are well reproduced by the calculations for the 85 and 170 nm layer thicknesses. For the 280 nm layer thickness, differences are observed between calculations and experiment that are attributed to the excitation of higher-order waveguide modes that are not included in the calculation. This aspect will be discussed shortly. The black dashed curve in Fig. 2.4b shows the geometrically averaged permittivity ϵ_{av}, calculated based on the effective medium theory assuming ρ = 50%. Clearly, the experimental data and the results of the analytical calculation are strongly redshifted compared to this simple model. Indeed, in our metamaterial geometry, with metal thicknesses larger than the skin depth, the electric field is partially excluded from the metal region, causing the effective medium approximation to be invalid. Because of this exclusion, the metal filling fraction is effectively lowered, resulting in a redshift. The data in Fig. 2.4 show how the ENZ condition can be controlled through the 400-800 nm spectral range for any given unit cell size by an appropriately chosen metal filling fraction.

To further study the metamaterial dispersion, we measured the transmission spectra for each metamaterial structure. Data were taken using a white-light source and a spectrograph equipped with a charge-coupled device (CCD) detector, and the spectra were normalized to the transmission through a reference hole. Figure 2.5a-d shows the transmission spectra for the four structures represented in Fig. 2.3. In all cases, the transmission is highly wavelength dependent; the transmission peaks

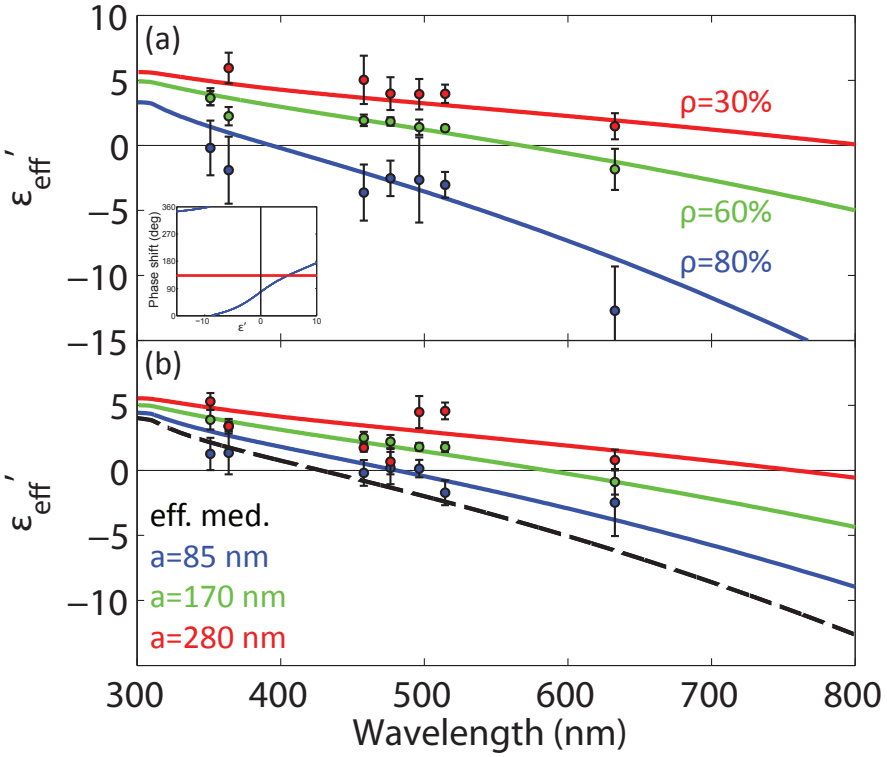

Figure 2.4: Metamaterial effective permittivity. **a**, Measured (data points) and calculated (solid lines) effective permittivity for 200 nm unit cell structures with metal filling fraction ρ = 30% (red), 60% (green) and 80% (blue). Inset: calculated phase shift (solid lines) as a function of effective metamaterial permittivity for a metamaterial sample (d_s = 45 nm; d_{SiN} = 93 nm, in blue) at λ = 633 nm. The measured phase shift is indicated by the horizontal red line. **b**, Measured and calculated effective permittivity for structures with a metal filling fraction of ρ = 50% and different unit cell size a = 280 nm (red), 170 nm (green) and 85 nm (blue). The effective permittivity based on the geometric average is also shown as the black dashed line. Error bars correspond to the standard deviation of the measured phase shifts converted to effective permittivity.

at a value as high as 90% for the 58 nm Ag/135 nm SiN metamaterial. Figure 2.5 also shows the simulated transmission (solid green lines) for the measured waveguide dimensions, taking into account the SiN underlayer. Overall, the experimental peak wavelengths are well reproduced by the simulation. The lower transmission for the 155 nm Ag/36 nm SiN metamaterial is also reproduced in the calculations. We attribute the difference in spectral shape between measurement and simulation to variations in waveguide dimensions across the sample. The reduced signal-to-noise ratio observed for wavelengths below 400 nm is caused by the low sensitivity of the CCD detector in this regime.

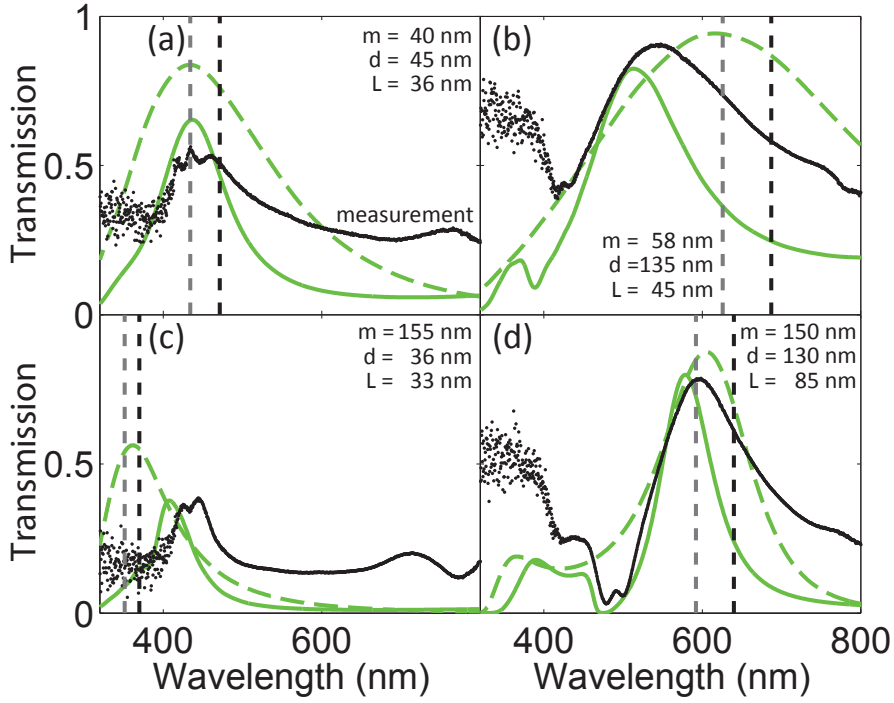

Figure 2.5: Transmission spectra and matching condition. Measured (black) and simulated (solid green) transmission spectra for four different metamaterial structures. The simulated transmission without the SiN underlayer (dashed green line) peaks at the same wavelength where the effective permittivity of the structure is around 1 (vertical grey dashed line), corresponding to air. The wavelength at which the effective permittivity is near zero is indicated by the vertical black dashed line.

To explain the origin of the transmission maximum, we also simulated the transmission of the same metamaterial geometries, but now without the SiN underlayer (dashed green lines). Also indicated in Fig. 2.5 are the wavelengths

at which the calculated effective permittivity of the metamaterial equals 1 (vertical grey dashed lines). In all cases, the wavelength at which $\epsilon' = 1$ agrees well with the wavelength of the peak in transmission (when there is no SiN underlayer), indicating that the transmission maximum results from a matched effective permittivity of the metamaterial to the surrounding air. The measured transmission peaks occur at slightly blueshifted wavelengths because, with the SiN underlayer present, the metamaterial sample effectively acts as an antireflection coating for the SiN underlayer. Indeed, such optimum impedance matching occurs for a metamaterial permittivity between that of air and SiN, which is in the blueshifted spectral range.

The vertical black dashed lines in Fig. 2.5 indicate the wavelengths at which the metamaterials reach the ENZ condition. The calculated transmission for the case without the SiN underlayer is still very high (for example, $T = 87\%$ in Fig. 2.5b), although somewhat reduced compared to the transmission at the impedance-matched $\epsilon' = 1$ condition wavelength. This is caused by an increased impedance mismatch and a reduced propagation length (Supplementary section "Propagation length"), leading to both increased reflection and increased absorption.

2.4 Size and angular dependence

An important criterion for metamaterials is that the constituent elements are sub-wavelength. Therefore, it is interesting to study how the effective optical properties change with unit cell size. As Fig. 2.4b demonstrates, a distinct redshift of the dispersion is observed for larger unit cell sizes with the same filling fraction. To further quantify this effect we calculated the supported waveguide eigenmode for different unit cell sizes. Figure 2.6a shows the calculated effective mode index using the same transfer matrix method described above, for a periodic unit cell with a constant metal filling fraction of 30%, and a unit cell size ranging from $a = 1$ nm to 600 nm at a free-space wavelength of $\lambda = 515$ nm. As can be seen, the real part of the mode index of the fundamental mode (solid black line) clearly converges to the expected index based on the effective-medium theory (dashed green line) for small unit cell dimensions ($n'_{\mathrm{eff}} = 0.75$ for this geometry). For large unit cell dimensions, the mode index approaches the SiN index (dashed blue line), as most of the light is excluded from the thick metal layers. The same behaviour is observed for the imaginary part of the index, as can be seen in Fig. 2.6b.

Around a unit cell size of a 250 nm, the first higher-order waveguide mode is no longer cut off at $\lambda = 515$ nm. The effective index for this mode is also shown in Fig. 2.6a as the solid grey line. Figure 2.6b shows that, for a unit cell larger than 300 nm, the imaginary part of this mode becomes comparable to that of the fundamental waveguide mode. The presence of higher-order modes limits the maximum unit cell dimensions allowed in the design of this metamaterial. Interestingly, the first higher-order mode was in fact observed in the measured and simulated phase shift for the largest fabricated unit cell ($a = 280$ nm), as can be seen in Fig. 2.3b. The

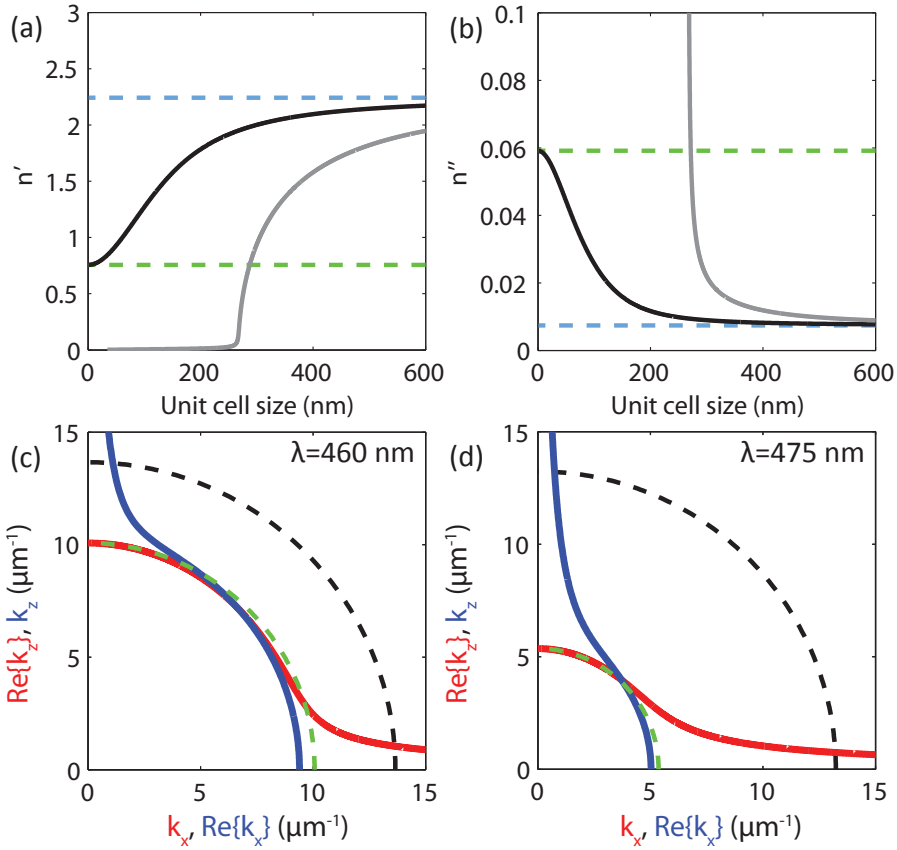

Figure 2.6: Isotropic index. **a,b**, Real (*a*) and imaginary (*b*) part of the mode index of the fundamental TE waveguide mode (black) and the first higher-order mode (grey) calculated versus unit cell size. For small unit cell sizes the effective index approaches the geometrically averaged index (green dashed lines), and for large unit cell sizes the mode index approaches the refractive index of SiN (blue dashed lines). **c**, Wavevector diagram for λ = 460 nm (a = 85 nm, ρ = 47%), demonstrating an effective index that is independent of angle. The green dashed curve corresponds to the expected isotropic index, and the black dashed curve is the wavevector in free space. **d**, Wavevector diagram calculated for λ = 475 nm. The mode index is reduced and still angle independent.

distinct oscillatory feature observed around 480 nm is due to a transition between the fundamental and the first higher-order mode.

So far, we have considered normally incident light. Next, we address the response of our three-dimensional ENZ metamaterial in the angular range between parallel incidence (along x) and perpendicular incidence (along z). Figure 2.6c shows the calculated wavevector diagram for light in the $x-z$ plane (free-space wavelength $\lambda = 460$ nm), for $a = 85$ nm and $\rho = 47\%$. To determine the response of the metamaterial for all incident angles, we performed two different calculations [21]. The first calculation determines the fundamental waveguide mode for a given small ($k_z < k_0$), real-valued k_z component (shown in blue). This calculation determines the wave propagation for light mainly along x. The second calculation determines the fundamental Bloch wavevector, assuming a small real-valued wavevector component along x ($k_x < k_0$) (shown in red). This situation represents wave propagation mainly along z. Also shown is the wavevector diagram of light propagation in air (black dashed line), and light propagation with an isotropic index equal to the waveguide mode index when $k_z = 0$ (green dashed line). The fact that the calculated wavevector diagram follows the isotropic index in their respective regions of interest indicates that for a unit cell of $a = 85$ nm the effective index of the structure is nearly angle independent. A small unit cell is required to obtain an angle independent refractive index, as light propagation normal to the waveguide interfaces (along z) is described by a Bloch wave composed of a series of harmonics, separated by the reciprocal lattice constant $\Lambda = 2\pi/a$ (ref. [29]): Λ must then remain much larger than wavevector k_z.

Figure 2.6d shows a wavevector diagram at a free-space wavelength of $\lambda = 475$ nm. Here, the mode index is strongly reduced because the metamaterial approaches cutoff, yet the response is still angle independent. When the mode index further approaches zero, the wavevector diagram will no longer be spherical, and the calculated value of k_x (k_z) will become independent of the k_z (k_x) component.

2.5 Conclusions

In conclusion, we have designed, fabricated and characterized an optical multilayered metamaterial consisting of thin Ag and SiN layers with an effective permittivity in the visible spectrum ranging from $\epsilon' = 6.0 \pm 1.2$ to $\epsilon' = -13 \pm 3.4$. The metamaterial is highly dispersive through the $\lambda = 400 - 800$ nm spectral range, and the dispersion is determined by the layer thicknesses and relative filling fraction. The epsilon-near-zero condition is experimentally demonstrated at wavelengths in the range $\lambda = 351 - 633$ nm. The optical transmission of the metamaterial is as high as 90% percent, and impedance matching to air is observed when $\epsilon' = 1$. The experimental data correspond well with analytical calculations and simulations. The transition from an effective medium material for small unit cell size to that of a coupled waveguide material for larger dimensions is studied. For the unit

cell size a = 85 nm, calculations show that the effective index is independent of angle. This highly dispersive metamaterial may find applications in transmission enhancement, wavefront shaping, control of spontaneous emission and superradiance.

2.6 Methods

Metamaterial samples were fabricated from a SiN membrane. The waveguide pattern was written in a Cr masking layer (20 nm) using FIB milling at normal incidence. The pattern was transferred to the SiN using an anisotropic CHF_3/O_2 reactive ion etch recipe. The etched channels were in-filled with Ag using physical vapour deposition. The surface of the metamaterial was then polished using FIB milling at oblique incidence.

The optical path length of the metamaterial sample was measured in a Mach-Zehnder interferometer. Light was focused through the metamaterial, and the length of the reference arm was changed with a piezo-electrically driven mirror, causing a sinusoidally oscillating intensity at the output. Light was then focused through a reference hole in the membrane, and the same reference mirror movement was performed. The sinusoidal signal was now displaced by a phase shift, caused by the optical path length of the metamaterial sample.

The simulated phase shift was obtained from FDTD simulations (Lumerical). We recorded the phase and amplitude of the transmitted plane wave after propagation through the structure. First the structure consisted only of a single SiN layer. The thickness of this SiN layer was increased from zero to the realized thickness, in steps of 1 nm. The thickness of the metamaterial on top of the SiN layer was then increased to the fabricated thickness.

2.7 Supplementary information

2.7.1 Phase advance

To illustrate how light propagates through an ideal ENZ material we have calculated the normalized field profile of a plane wave incident on an ENZ slab 400 nm thick with a permittivity $\epsilon = 10^{-4}$ and $\mu = 1$ for a free-space wavelength $\lambda_0 = 500$ nm. Figure 2.7(a) shows the real part of the H_z and E_y field profile. The magnetic field is constant inside the slab, and the electric field has a linear dependence on the position in the slab, as expected from Ref. [34] of the main text. Figure 2.7(b) shows the extracted phase shift and absolute amplitude of light transmitted through the slab as a function of slab thickness L. The phase converges to 90 degrees while the amplitude vanishes. This initial change in phase is caused by a changing field at the first interface of the slab due to an increased reflected wave. Eventually this phase change becomes thickness independent.

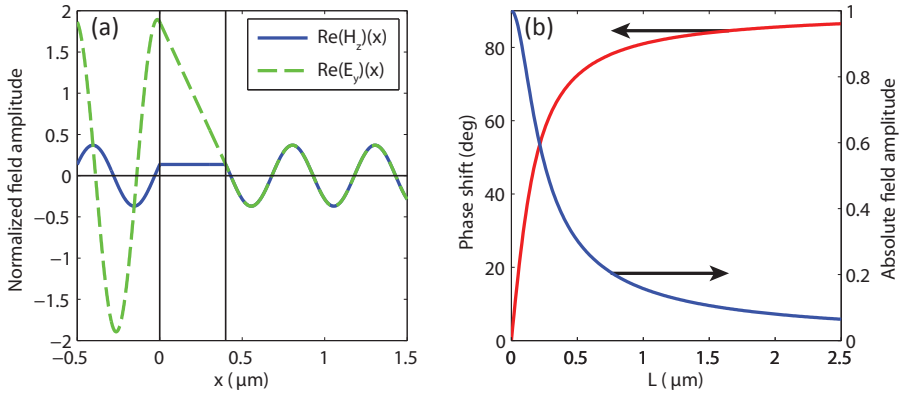

Figure 2.7: Phase advance. **a**, Calculated field profile of a plane wave propagating through an ENZ slab. The slab has a thickness of 400 nm, and assumed permittivity and permeability $\epsilon = 10^{-4}$ and $\mu = 1$, the free-space wavelength for the calculation is taken to be 500 nm. **b**, Calculated phase shift and absolute amplitude of the plane wave transmitted through the slab as a function of slab thickness L.

2.7.2 Ellipsometry

The optical constants of thin Ag and SiN layers given in Fig. 2.1(a) were determined using variable-angle spectroscopic ellipsometry (VASE, J.A. Woollam Co., Inc.). For these measurements Ag layers of different thicknesses (30 - 60 nm) were deposited on a silicon wafer using thermal evaporation. A point by point fit was used to obtain the optical constants of the evaporated metal layers. The optical constants of the SiN layer were determined using VASE by measuring on a part of the silicon window frame, which was covered by the same SiN membrane as was freestanding in the middle of the window. A Cauchy model was used to fit the refractive index of the SiN dielectric layer to the measured data, and good agreement was observed.

2.7.3 Fabrication

We fabricated the multilayered metamaterial starting with a commercially available 200-nm-thick low-stress SiN membrane grown with low - pressure chemical vapor deposition (Norcada Inc.). The membrane is covered by a 20 nm Cr masking layer using thermal evaporation. An array of parallel linear slots is written in the masking layer using a 1.5 pA, 30 keV Ga^+ ion beam focused to a diameter of 10 nm, as sketched in Fig. 2.8(a). Subsequently the pattern is transferred into the SiN layer by anisotropic reactive ion etching using a CHF_3/O_2 mixture. As shown in Fig. 2.8(b-c), after the etching process there still is a thin layer of SiN left underneath the etched waveguide stripes. This underlayer provides mechanical stability for the otherwise freestanding SiN stripes.

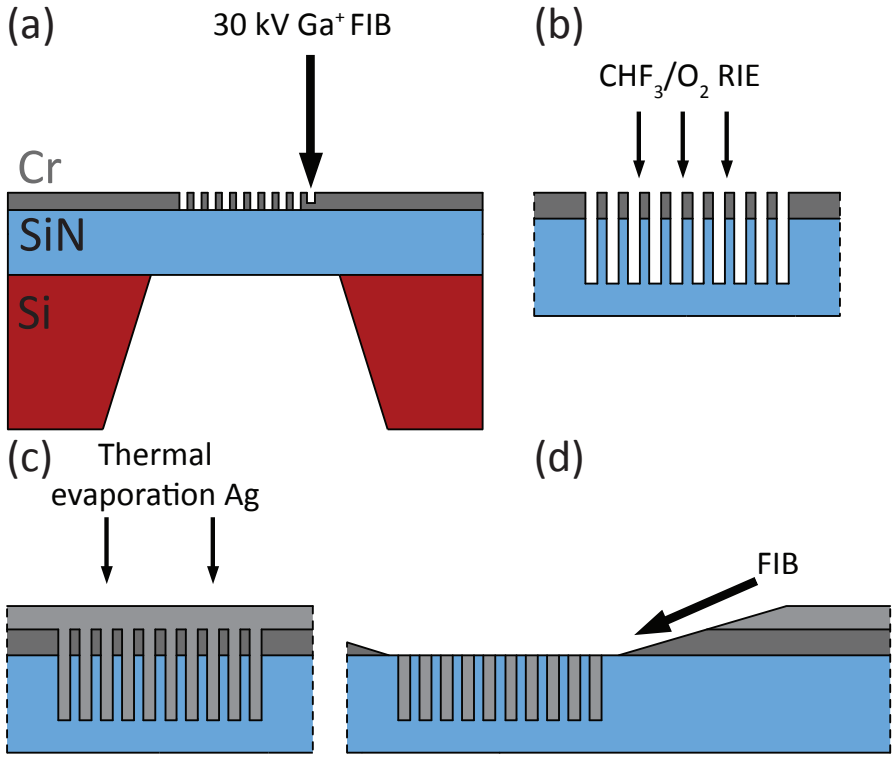

Figure 2.8: Metamaterial fabrication. **a**, Patterning of the Cr masking layer using FIB. **b**, Anisotropic etching of the SiN membrane with an anisotropic reactive ion etching recipe. **c**, Thermal deposition of Ag over the entire sample surface. **d**, FIB polishing of the metamaterial surface to remove excess metal.

The channels etched in the SiN layer are then infilled with Ag using thermal evaporation at a pressure of 10^{-6} mbar. By carefully aligning the sample in a direct line of sight to the source the channels were completely filled with metal. As a result of the deposition process, the entire membrane surface is covered with an optically thick metal layer. To allow access to the metamaterial, the metal layer on top of the metamaterial is polished with a focused ion beam at an oblique angle of incidence ($\theta \approx 3°$), see Fig 2.8(d). This polishing is continued until the multilayered metamaterial structure is revealed. Square reference holes are placed at a distance of 5 μm away from the exposed metamaterial structures by FIB milling through the entire Ag/SiN layer stack at normal incidence. After the optical measurements SEM cross sections of the metamaterial samples were made using focused ion beam milling. To enhance contrast, the metamaterial was first covered with Pt using electron-beam induced deposition at the top and bottom side of the membrane.

2.7.4 Interferometry

Figure 2.9(a) shows a sketch of the interferometer setup. Light from either an Ar+ or HeNe laser is split into a reference and a sample path using a 50/50 beam splitter. Microscopes objectives (numerical aperture NA = 0.45) are used to focus and collect light from the metamaterial. The spot size was around 5 μm, illuminating 20 to 60 unit cells, depending on the exact geometry of the metamaterial. The transmitted beam is interfered with the reference beam using a second 50/50 beam splitter. The intensity of the interfering beams is measured on a photodiode placed behind this beam splitter. A piezo-electrically driven mirror in the reference arm is continuously displaced using a saw tooth driving function, leading to a constant advance of the phase of the reference beam with time. Typical interference oscillations versus time are shown in Fig. 2.9(b) when light is focused through the metamaterial sample (red) and for light transmitted through a reference hole through the membrane (blue). A second piezo-electric stage is used to switch between measurements through the metamaterial area and through the reference hole. A sine wave is fitted to both interference traces, and the relative phase shift $\Delta\phi = \phi_s - \phi_r$, where ϕ_s and ϕ_r are the phases for sample and reference trace respectively. This phase shift is a direct measure for the optical path length of the metamaterial. The entire measurement cycle alternating between the metamaterial area and the reference hole is synchronized and computer controlled, and is repeated multiple times to allow for an accurate determination of the phase shift.

Figure 2.9(c) shows a histogram of phase shifts determined from 400 measurements on a metamaterial structure at a free-space wavelength $\lambda = 633$ nm (in red). The average phase shift of these measurements is $37\pm10°$. The error is caused by the reproducibility of the piezo mirror position, which varies by approximately 25 nm. Figure 2.9(c) also shows a histogram of phase shifts measured on the same metamaterial structure at $\lambda = 364$ nm (purple). To determine the full dispersion of the metamaterial structure the phase shift is measured using six different lines of an Ar+ laser (in the range $\lambda = 351$-515 nm) and a HeNe laser ($\lambda = 633$ nm). The coherence length of these light sources is sufficiently long to allow us to observe interference in the setup where the sample and reference beam paths of the interferometer are of different length. All phase shifts reported in the main text are measured relative to an air reference hole.

2.7.5 Phase shifts and effective permittivity

The inset of Fig. 2.4(a) shows the dependence between the effective permittivity of a metamaterial sample and the measured phase shift. In this model, it is assumed that the imaginary part of the permittivity is zero, such that only the real part of the permittivity contributes to the measured phase shift. We justify this assumption by the observation that the imaginary part of the geometrically averaged permittivity ϵ'' <0.2 in the $\lambda = 400-650$ nm spectral range (Fig. 2.1(b)). To study the effect of a non-negligible imaginary part, we plot the same graph as the inset of Fig. 2.4(a)

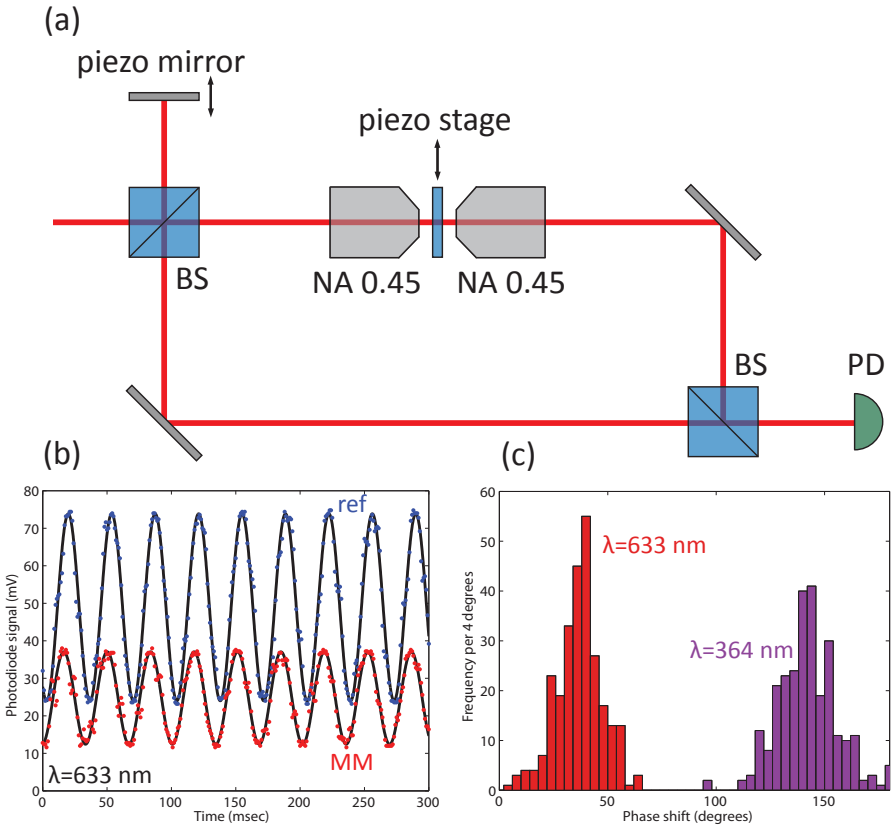

Figure 2.9: Interferometry. **a**, Sketch of the Mach-Zehnder interferometer setup used to measure the optical path length of the metamaterial samples. **b**, Interference signal on photodiode as the mirror position is varied over time. The fitted sinusoidal function through the metamaterial data (red) has a different phase than the fitted sinusoidal function of the reference measurement (blue). **c**, Histogram of 400 measurements demonstrating a distinct difference in average phase shift between measurements at $\lambda = 633$ nm (red) and $\lambda = 364$ nm (purple).

for four different ϵ'': 0, 0.1, 0.5 and 1. The effect of adding this imaginary part can be seen in Fig. 2.10(a). The relation between the calculated phase shift and the effective metamaterial permittivity is only slightly shifted by adding an imaginary part to the permittivity. This shift is most pronounced in the regime where ϵ' <<0. However, this paper mainly focuses on the regime where $\epsilon' \approx 0$. To demonstrate the effect of a nonzero imaginary part in this ENZ regime, we have calculated the expected phase shift in this regime, with an imaginary part $0 < \epsilon'' < 1$. Figure 2.10(b) shows the result of this calculation. The calculated phase shift only changes by a few degrees in this range, well within the experimental error of our setup.

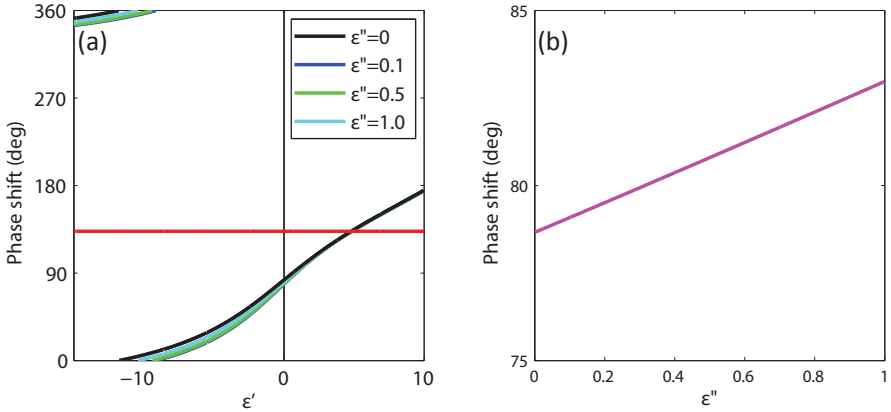

Figure 2.10: Phase shift and permittivity. **a**, Effect of a nonzero imaginary part of the permittivity. The relation between the calculated phase shift and effective metamaterial permittivity is slightly shifted for higher imaginary parts. The effect is most pronounced in the regime where the real part is negative. **b**, The calculated effect on phase shift at the ENZ condition ($\epsilon' \approx 0$), which shows only a change of a few degrees.

2.7.6 Thickness dependence

The effective optical properties of a metamaterial should be independent of thickness. To determine the effective permittivity as a function of thickness, we use a parameter retrieval method, where we utilize the simulated complex reflection and transmission coefficients in order to extract the material parameters [47]. The extracted permittivity and permeability are calculated as a function of metamaterial thickness and free-space wavelength, to ensure the correct branches of the solution are used.

Figure 2.11(a) shows the extracted real part of the permittivity as a function of metamaterial thickness. This permittivity is calculated for a unit cell with dimensions m=40 nm and d=45 nm, at three different wavelengths. As can be seen for λ =

475 nm and λ = 650 nm, the permittivity becomes almost thickness-independent for metamaterials thicker than 15 nm. Note, the experiments were preformed for thicknesses well beyond this thickness. This indicates that the effective measured permittivity is indeed determined by the waveguide dispersion. The oscillation in the calculation for λ = 350 nm is attributed to interference inside the layer that results from the relatively high effective permittivity at this wavelength (ϵ' = 3.0).

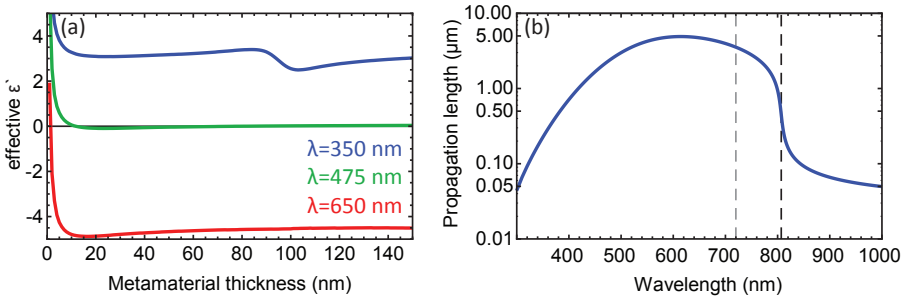

Figure 2.11: Thickness dependence and propagation length. **a**, Calculated real part of the effective permittivity as a function of thickness. **b**, Propagation length as a function of wavelength, calculated for a unit cell with m = 58 nm and d = 135 nm. The vertical gray line indicates the wavelength at which the free-standing metamaterial is impedance matched to free-space, and the vertical black line indicates the ENZ condition.

2.7.7 Propagation length

In the main text we demonstrated high transmission through the fabricated metamaterial samples. The observed maximum in transmission was attributed to an optimized impedance leading to low reflection. There is however also absorption in the metamaterial, which attenuates the electromagnetic wave as it propagates through the sample. To determine this attenuation, we calculate the propagation length, defined as $L_p = 1/(2 * \mathrm{Im}(k_{wg}))$, where k_{wg} is the wavevector of the waveguide mode in a periodic system. Figure 2.11(b) shows the calculated propagation length as a function of wavelength. The vertical gray line indicates the wavelength at which this metamaterial is impedance matched to air, and the vertical black line indicates the wavelength at which the effective permittivity becomes zero.

As is evident from this figure, the propagation length is strongly reduced as the ENZ condition is approached. As the ENZ point is crossed, the material becomes increasingly metallic, explaining the reduced propagation length. However, very close to this ENZ condition, the propagation length is approximately 500 nm, well beyond the thickness of the film, in agreement with the relatively high transmission observed from the metamaterial.

3

Negative refractive index and higher-order harmonics in layered metallodielectric optical metamaterials

We study the propagation of light in a three-dimensional double-periodic Ag/TiO_2 multilayer metamaterial composed of coupled plasmonic waveguides operating in the visible and UV spectral range. For these frequencies, light propagation in the plane of the waveguides is described by a negative phase velocity, while for the orthogonal direction light propagation is described by a Bloch wave composed of a large number of harmonics. As a result, the material cannot generally be described by a single phase index: by decomposing the Bloch wave into different harmonics, we show that for the wavelength range of interest the positive index $m = 1$ harmonic dominates the propagation of light in the orthogonal direction. These results are corroborated by numerical simulations and optical refraction experiments on a double-periodic Ag/TiO_2 multilayer metamaterial prism in the $380 - 600$ nm spectral range, which shows that positive refraction associated with right-handed harmonics dominates. By studying the isofrequency contours, we find that despite the occurrence of multiple harmonics the double-periodic structure can act as a flat lens: for a slab consisting of an integer number of unit cells, all harmonics are degenerate and constructively interfere at the image plane. This work identifies important considerations relevant to the design of many three-dimensional periodic metamaterials.

3.1 Introduction

Negative-index or "left-handed" metamaterials are structures in which light propagates with opposite phase and energy velocities, [48] enabling an entirely new class of optical components such as, for example, flat lenses, [5] potentially allowing an image resolution below the diffraction limit. [49–52] In the past decade, negative-index metamaterials have been fabricated for a broad range of frequencies. [53] The first demonstration was achieved in the microwave regime, [8] and since then, scaling down of the unit cell size enabled by advances in nanofabrication has led to metamaterials with operation frequencies toward the visible spectral range. [54]

Most metamaterial design architectures are based on resonant geometries such as, for example, split rings, [7] fishnet structures, [10] and others. [55] Recently, our group has proposed a three-dimensional, negative-index metamaterial based on a double-periodic metal/dielectric multilayer geometry, operating in the UV spectral range. [21] It is based on a multilayer stack of negative-index waveguides, [18, 20, 56] where TM-polarized light couples to surface plasmon polaritons at the metal/dielectric interfaces. By careful design of the coupling between adjacent waveguides, an angle-independent negative fundamental mode index can be achieved, implying that light propagation in the plane of the waveguides and normal to it is characterized by the same (negative) propagation constant. An experimental realization of this geometry has been used to study negative refraction of energy and to show flat lensing behavior. [57]

To further investigate the behavior of this multilayer metamaterial geometry, it is important to evaluate the role of other (higher-order) harmonics, aside from the fundamental harmonic. The solution of the wave equation in a periodic medium is a Floquet-Bloch wave, composed of a superposition of multiple plane waves with different propagation constants. Previous work on photonic crystals shows how the periodicity of the geometry leads to an ambiguity in the determination of an effective phase index. [58, 59] In this paper, we study these harmonics and quantify their propagation characteristics, specifically for a metal-dielectric multilayer structure, which exhibits strong dispersion and significant absorption in the UV-visible spectral range. First, we use a transfer matrix formalism to determine the exact properties of the Bloch wave in a theoretical infinitely thick periodic medium. The decomposition into harmonics shows that the fundamental harmonic (located in the first Brillouin zone) is not the most dominant in the system. Comparing this decomposition with isofrequency contours (IFCs) we show that the dominant harmonic is not characterized by a left-handed response. Second, we study the implications of this result for phase and energy refraction in finite structures, with analytical calculations, numerical simulations, and finally, by performing refraction experiments using a metamaterial prism.

3.2 Field decomposition

A sketch of the geometry studied here is shown in Figure 3.1a. A multilayer stack is formed by alternating Ag and TiO_2 layers. Light incident on the side of this stack will couple to waveguide modes. The layer thicknesses are optimized such that at frequencies above the surface plasmon resonance frequency there is only a single negative index waveguide mode supported by the system. [20] As light propagates parallel to the waveguides, it experiences a constant environment and propagates with a negative waveguide mode wavevector. This causes phase and energy to travel in antiparallel directions, a key characteristic of left-handed materials. The fact that the metal layers are alternatingly thin and thick causes the coupling constant between adjacent unit cells to be negative [21] such that phase and energy velocities are antiparallel for a wide range of angles.

However, for wave propagation in any direction other than parallel to the waveguides, the periodically varying permittivity experienced by light physically changes the nature of wave propagation. To study this, we consider the extreme limit of light traveling normal to the waveguides. Using a transfer matrix method, we calculate how light propagates through an infinitely periodic multilayer structure. We adopt the notation of Russell [29] and calculate the field in this periodic unit cell from the transfer matrix, assuming TM polarization. We express the magnetic field profile in a single layer as*

$$H_{y,j}^N(z) = a_j^N \cos(k_{z,j}(z - z_j^N)) + b_j^N \frac{n_j^2}{a k_{z,j}} \sin(k_{z,j}(z - z_j^N)) \tag{3.1}$$

where $k_{z,j}$ is the wavevector component along z, defined by $k_{z,j} = \sqrt{n_j^2 k_0^2 - k_x^2}$, z_j^N is the center of layer j in unit cell N, n_j is the refractive index of layer j, and a is the unit cell size. From this magnetic field profile, also the electric field profile can be determined using the Ampere-Maxwell law. The coefficients a_j^N and b_j^N are related by

$$\begin{pmatrix} a_j^{N+1} \\ b_j^{N+1} \end{pmatrix} = M_{trans} \begin{pmatrix} a_j^N \\ b_j^N \end{pmatrix} \tag{3.2}$$

The coefficients of the first layer in unit cell N can be defined as [29] $a_1^N = \sqrt{(M_{trans})_{12}}$ and $b_1^N = \pm\sqrt{(M_{trans})_{21}}$, where $M_{trans} = M_{14}M_{43}M_{32}M_{21}$, and the matrix M_{ji} relates the coefficients in adjacent layers through $\begin{pmatrix} a_j^N \\ b_j^N \end{pmatrix} = M_{ji} \begin{pmatrix} a_i^N \\ b_i^N \end{pmatrix}$, such that the boundary conditions are fulfilled. This definition of M_{trans} imposes periodic boundary conditions, leading to an infinitely periodic, closed system. The eigenvalues $\lambda_\pm$ of the transfer matrix are related to the complex Bloch wavevector in the first Brillouin zone as $\lambda_\pm = \exp(\pm i k_{Bl} a)$. In the above, $\pm$ refers to a

*For off-normal incidence the field expression has an additional factor $\exp(ik_x x)$. Coefficients a_j, b_j, and $k_{z,j}$ are also functions of k_x, the parallel wavevector momentum.

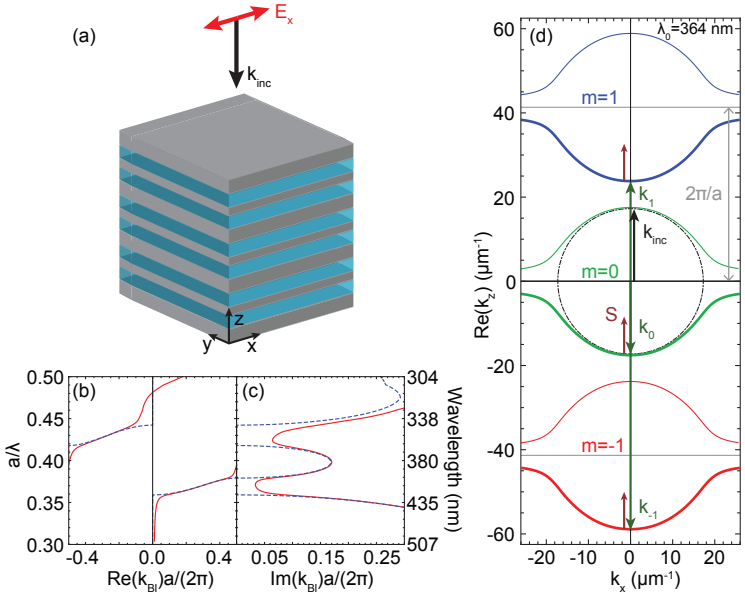

Figure 3.1: **a**, Sketch of the experimental double periodic geometry. Gray layers correspond to Ag and blue layers to TiO_2. **b**, Calculated band diagram of the double-periodic metamaterial. The unit cell size is a = 152 nm. Solid (dashed) lines correspond to the geometry with (without) losses. Wave frequency (in units of a/λ_0) is plotted vs the real (b) and imaginary (c) part of the Bloch wavevector. The sign of the wavevector is chosen such that $\mathrm{Im}(k_{Bl}) > 0$ at every frequency, corresponding to the forward energy propagation direction. Two transmission bands are observed at λ_0 = 345-365 and 400-425 nm. **d**, Isofrequency contours for the Ag/TiO_2 double-periodic multilayer metamaterial (x and z are in-plane and normal components, respectively). Data are shown for fundamental (m = 0) and higher-order (m = -1, 1) harmonics at a free space wavelength of λ_0 = 364 nm. The Poynting vector is normal to the isofrequency contour, with the direction determined by the sign of $\partial\omega/\partial k$ derived from IFC calculations at multiple frequencies. Bold-plotted IFC branches correspond to energy propagation in the positive z direction. A negative refractive index occurs when the wavevector is antiparallel to the time-averaged Poynting vector which is the case for the m = -1, 0 harmonics but not for the dominant m = 1 mode.

wave with energy travelling in the $+z$ or $-z$ direction. We perform calculations for a $Ag/TiO_2/Ag/TiO_2$ double-periodic geometry, using optical constants and layer thicknesses from Xu et al. [57] (see Table 3.1). We consider waves with energy propagating in the $+z$ direction, such that $\mathrm{Im}(k_{Bl}) \geq 0$. At a wavelength $\lambda_0 = 363.8$ nm and for normal incidence we find $k_{Bl} = -17.17 + 4.05i\,\mu m^{-1}$, where the negative real part reflects that phase propagates backward as energy propagates forward for the fundamental harmonic.

We repeat this calculation for a whole range of wavelengths to determine the band diagram for this geometry. In this calculation we use optical constants experimentally determined from variable-angle, spectroscopic ellipsometry on individual Ag and TiO_2 layers, deposited on a Si substrate using physical vapor deposition. The first Brillouin zone is shown in Figure 3.1b, where the solid lines correspond to the calculation, taking losses into account. From the band diagram we can identify two regimes where the imaginary part of the Bloch wavevector (shown in Figure 3.1c) is relatively low, corresponding to weak attenuation. Also shown is the band structure for the same geometry, but with the imaginary part of the permittivity set to zero (dashed lines). Two propagation bands are clearly observed at $\lambda_0 = 345-365$ and $400-425$ nm and correspond to the two regimes of low attenuation in the geometry with absorption.

The field profile of the Bloch wave, known from Eq. 3.1, can be expanded as

$$H_y(z) = \exp(i\,k_{Bl}\,z) \sum_{m=-\infty}^{\infty} h_{y,m} \exp(i\frac{2\pi}{a} m z) \tag{3.3}$$

where $h_{y,m}$ represents the amplitude of the plane wave (harmonic) indicated by index m, with wavevector $k_m = k_{Bl} + (2\pi/a)m$. The amplitude $h_{y,m}$ can be found by performing a simple Fourier decomposition:

$$h_{y,m} = \frac{1}{a} \int_0^a H_y(z) \exp(-i\,k_{Bl}\,z) \exp(-i\frac{2\pi}{a} m z)\,dz \tag{3.4}$$

	model	**experiment**
d_1 TiO_2	28 nm	44 nm
d_2 Ag	30 nm	32 nm
d_3 TiO_2	28 nm	44 nm
d_4 Ag	66 nm	50 nm
ϵ_{Ag} (364 nm)	-2.522 + 0.250i	-2.214 + 0.262i
ϵ_{TiO_2} (364 nm)	7.838 + 0.280i	7.566 + 0.175i

Table 3.1: Optical constants and layer thicknesses. **a**, Layer thicknesses and optical constants in the model are taken from Ref. [57]. The layer thicknesses of the multilayer structure in the experiment were optimized for operation at a free-space wavelength of $\lambda_0 = 410$ nm. The optical constants of deposited Ag and TiO_2 layers were experimentally determined using variable-angle spectroscopic ellipsometry.

This shows that only considering the first Brillouin zone, as in Figure 3.1b, does not capture the full propagation characteristics of the Bloch wave. Instead, all harmonics with their corresponding weights should be taken into account. The different harmonics can be plotted in a wavevector diagram, where the Bloch wavevector is calculated at a fixed frequency, but now for different angles of propagation (so different values of k_x). The interface boundary conditions are angle-dependent, leading to a change in the Bloch wavevector. In the calculation, the parallel wavevector component k_x is chosen to be real valued.

The wavevector diagram is given in Figure 3.1d, where we show the real part of k_z plotted against k_x, at a free-space wavelength of 364 nm. Here we include not only the fundamental isofrequency contour, but also that of the first higher orders (m = -1, 0, 1; red, green, blue). From the band diagram (Figure 3.1b) we determine that the time and unit cell averaged Poynting vector is directed inward [21, 60] for this frequency. The bold isofrequency contours correspond to the Bloch wave propagating in the positive z direction. The $m = 0$ and m = -1, -2, ... IFCs in Figure 3.1d show left-handed behavior as wavevector k_m and Poynting vector S (indicated by arrows in the figure) are antiparallel. In contrast, the $m = 1, 2, ...$ IFCs do not show such behavior and do not satisfy the criterion $k_m \cdot S < 0$. Thus, $m \geq 0$ harmonics can be called "left handed", and $m > 0$ can be called "right handed".

From the wavevector diagram we have identified that different harmonics can be associated with either a left- or right-handed response. Therefore, it is important to know the exact contribution of each harmonic to the total Bloch wave. We determine these contributions by decomposing the Bloch wave using Eq. 3.4. The result of this decomposition is shown in Figure 3.2a for the range $-10 < m < 10$. As is clear from this figure, a large number of harmonics have a significant amplitude. This implies that to properly describe light propagation in this multilayer metamaterial geometry a large number of harmonics must be taken into account. This is contrary to earlier work where only the fundamental $m = 0$ harmonic was considered. [61, 62] Interestingly, the $m = 1$ harmonic has an amplitude higher than that of the fundamental harmonic. We performed the same analysis for the electric field component E_x; the amplitude coefficients for these harmonics are also shown in Figure 3.2a, where a similar trend is found. As an illustration, we show the real part of the calculated Bloch wave in Figure 3.2b (top) and the individual harmonics following from the decomposition of the Bloch wave (bottom).

The fact that a large number of harmonics contribute significantly to the Bloch wave implies that the phase index of the structure cannot be unambiguously defined: each harmonic has a different propagation wavevector k_m and, therefore, a different phase velocity $v_{ph,m} = (\omega / k_m)$. Note that the Bloch wavevector is always complex valued (we write $k_m = k'_m + i k''_{Bl}$), such that the phase velocity is also complex valued. As the propagation wavevector always appears in an exponential term, the imaginary part corresponds to an attenuation factor $\exp(-k''_{Bl} z)$, and the real part determines the phasor term $\exp(i k'_m z)$. Therefore, the phase velocity can be defined as $v_{ph,m} = (\omega / k'_m)$.

To determine the energy density carried by the different harmonics, we first

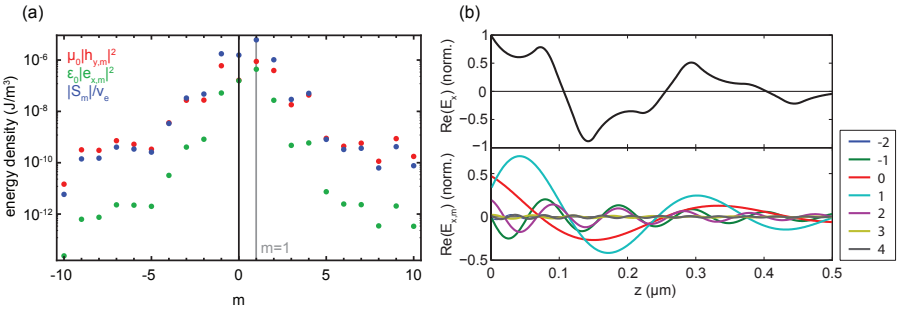

Figure 3.2: **a**, Calculated amplitude of harmonics in the range $-10 < m < 10$ for the periodic electric and magnetic field profiles at a free space wavelength of $\lambda_0 = 364$ nm. The decomposition of the unit cell averaged Poynting vector is also shown. A large number of harmonics have a significant amplitude, and for all decompositions, the $m = 1$ harmonics has the highest amplitude. **b**, Calculated real part of the electric field profile inside the multilayer structure (top). Real part of seven harmonics of the electric field (bottom).

calculate the energy velocity [30] $v_e = \langle\langle S(z)\rangle_t\rangle_{UC} / \langle\langle U(z)\rangle_t\rangle_{UC}$. We determine the time and unit cell averaged Poynting vector S and energy density U of the Bloch wave from the $E_x(z)$ and $H_y(z)$ field profiles. Because there is significant dispersion and loss, we use $U(z) = \frac{1}{4}(\frac{\partial(\omega\epsilon(\omega,z)\epsilon_0)}{\partial\omega}|\vec{E}(z)|^2 + \mu\mu_0|\vec{H}(z)|^2)$ from Ref. [63]. The result is shown in Figure 3.3: the energy velocity is always positive and increases in the regions of low loss. The calculated Poynting vector is a property of the complete Bloch wave and not of individual harmonics. This is due to the fact that the calculation of the Poynting vector contains a multiplication of E and H fields, leading to cross terms relating different harmonics. However, integrating the Poynting vector over the unit cell leads to a cancellation of these cross terms, so the unit-cell averaged Poynting vector can, in fact, be decomposed into separate harmonics. Performing this decomposition, we find that the $m = 1$ harmonic component has the highest amplitude, similar to what we found for the decomposition of the E_x and H_y field profiles. The result of the unit-cell averaged Poynting vector decomposition is also included in Figure 3.2. The absolute value of the components is divided by the energy velocity to arrive at the energy density.

The $m = 1$ component carries 58% of the energy, whereas the fundamental $m = 0$ component only accounts for 15% of the total energy carried by the Bloch wave. All right-handed components of the Bloch wave combined contain 68% of the wave energy, see Table 3.2. The fact that multiple higher-order harmonics carry a significant amount of the energy indicates that the structure cannot be described by a single refractive index. Figure 3.4 shows the total energy fraction carried by all right-handed harmonics combined as a function of wavelength. As can be seen, this fraction is larger than 50% for all wavelengths, indicating this is a broadband effect. Furthermore, we have performed the same decomposition for different unit

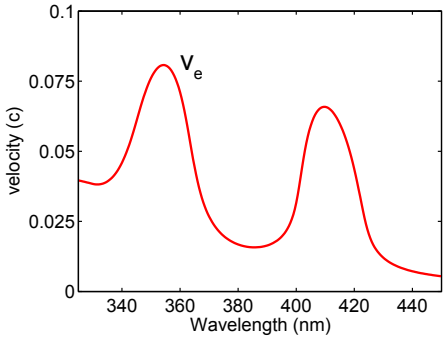

Figure 3.3: Calculated energy velocity for the multilayered metamaterial. The energy velocity is significantly higher in the two propagation bands where the attenuation is relatively low: $\lambda_0 = 345 - 365$ and $400 - 425$ nm.

cell sizes (see Figure 3.4b), and we note that, although the angle-independent nature of the metamaterial is highly dependent on the exact layer thicknesses, the distribution of energy over right-handed harmonics remains between 60 and 70% if the unit cell size is scaled by ±10%

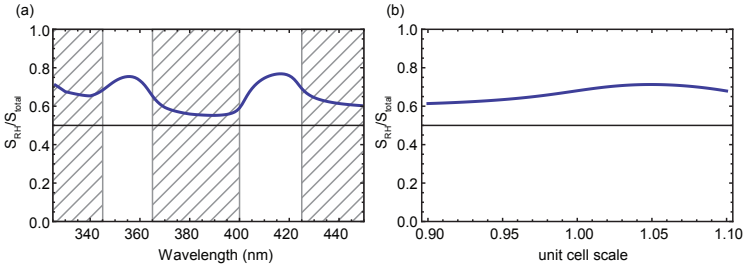

Figure 3.4: **a**, Calculated total energy fraction carried by all right-handed harmonics combined, as a function of wavelength. Shaded regions correspond to wavelength at which the multilayer structure shows strong absorption. **b**, Right-handed harmonic energy fraction calculated for a changing unit cell scale.

3.3 Finite-sized multilayer structures

In the above, we have analytically studied light propagation through an infinitely periodic multilayer structure. Next, we shall investigate how light interacts with different finite-sized structures to show that the above considerations have a pronounced impact on the optical response of finite-sized multilayer structures. First,

m	$k_m(\mu\text{m}^{-1})$	$\lvert S_m\rvert/S_{total}$
-2	$-99.85+4.05i$	0.0045
-1	$-58.51+4.05i$	0.1653
0	$-17.17+4.05i$	0.1463
1	$24.16+4.05i$	0.5762
2	$65.50+4.05i$	0.0965

Table 3.2: Wave vector and Poynting vector amplitude decomposition. **a**, Calculated for a free-space wavelength of 363.8 nm, using the layer thicknesses and material constants in Table 3.1. S_{total} is defined as $S_{total} = \sum_{m=-\infty}^{\infty} |S_m|$. The positive index $m = 1$ harmonic has the highest amplitude. Furthermore, the sum of $|S_m|/S_{total}$ for $m = 1, 2, ...$ equals 68%, indicating that most of the energy of the Bloch wave is carried by right-handed harmonics.

we perform exact transfer-matrix calculations of the phase accrue of a normal-incident plane wave transmitted through a Ag/TiO_2 multilayer slab. This phase advance is determined at the vacuum side of the exit interface, relative to the phase at the vacuum side of the first interface. The transmitted phase is calculated for a slab with a gradually increasing thickness. Figure 3.5a shows calculations for three different wavelengths. For a wavelength of $\lambda_0 = 364$ and 410 nm, the phase advance in Figure 3.5a has a positive overall slope. At a wavelength of $\lambda_0 = 450$ nm, there is no overall increase of the transmitted phase.

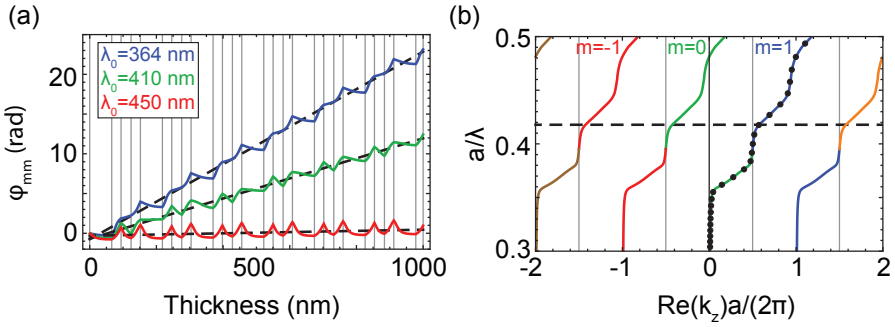

Figure 3.5: a, Calculated phase shift as a function of multilayer stack thickness for free-space wavelengths of $\lambda_0 = 364, 410$, and 450 nm. The vertical gray lines indicate the metal/dielectric interfaces. A linear function (dashed black line) is fitted to the calculated phase shift and shows a positive slope for $\lambda_0 = 364$ and 410 nm. **b**, Band structure showing the different harmonics. Frequency is expressed in units of a/λ_0, with $a = 152$ nm the unit-cell lattice constant. $m = -1, 0, 1$ bands are shown in red, green, and blue, respectively. Solid dots are effective wave vectors determined from calculations as in (a). The dashed horizontal line at $0.42a/\lambda_0$ corresponds to a free space wavelength of $\lambda_0 = 364$ nm.

As we have seen in the periodic structure, a large number of harmonics contribute to wave propagation. Here, the phase increases along a single slope, with small deviations due to multiple internal reflections in individual layers. If we approximate this phase advance by a single effective wavevector, we can fit a linear function $\phi(L) = k_{\text{eff}}L$ to the data of Figure 3.5a and similar calculations in the $0.3 - 0.5a/\lambda_0$ frequency range. The results are shown as solid dots in the band diagram of the metamaterial (Figure 3.5b). The colors of the bands correspond to the different harmonics ($m = -1, 0, 1$). As can be seen for longer wavelength ($a/\lambda_0 < 0.4$), the $m = 0$ harmonic is dominant; however, at these wavelengths, the fundamental harmonic is described by right-handed behavior. For shorter wavelengths ($a/\lambda_0 > 0.4$), the fundamental harmonic is characterized by a left-handed response, but the (right-handed) $m = 1$ harmonic dominates. This is in good agreement with the decomposition of the Bloch wave for different wavelengths; the overall phase advance is determined by the harmonic with the highest amplitude.

At normal incidence, the harmonic wavevectors are all aligned. However, when the Bloch wave meets an interface at an angle, [64] refraction is determined by the conservation of the parallel projection of the wavevector on this interface (Figure 3.6a). Therefore, each harmonic will refract with a different angle. Using finite-difference time-domain simulations, we study a Ag/TiO_2 prism composed of 15 unit cells, truncated by an output facet at an angle of 5°; layer thicknesses and optical constants are as in Table 3.1 (model). Figure 3.6b shows the far-field angular distribution of the electric field intensity. For a plane wave at normal incidence multiple refraction peaks are observed, corresponding to the different harmonics. The expected refraction angles from the different harmonics are constructed using the IFCs in Figure 3.1d and are indicated by vertical dashed lines. The simulated refraction peaks correspond very well to these constructed refraction angles. We note that the refraction angles are the same as the diffraction orders from the grating formed by our output facet. While the grating could thus in principle redistribute the various harmonics in the metamaterial among the different refraction peaks, it is striking that the peak amplitude distribution is similar to the harmonic decomposition of the electric field shown in Figure 3.2. The fact that the $m = 1$ harmonic is the dominant refraction component from the metamaterial prism is a strong indication for the dominance of this harmonic in the internal Bloch wave.

In order to study refraction experimentally, a 6μm×6μm microprism was sculpted from a Ag/TiO_2 multilayer stack. This multilayer stack consisted of 2.5 periods of a Ag/TiO_2/Ag/TiO_2 unit cell with layer thicknesses given in Table 3.1, optimized for operation at a free-space wavelength of 410 nm. This stack was deposited on a freestanding SiN membrane using physical vapor deposition. Using focused ion beam milling with a 30 kV Ga^+ beam at an oblique angle, an output facet with an angle of 4.1° with respect to the layers was fabricated, forming a prism in the multilayer stack. A scanning electron micrograph side view of this output facet is shown in the inset of Figure 3.7b.

Refraction by the metamaterial sample was measured in a Fourier microscope (Figure 3.7a). Spectrally filtered light from a Xe-arc lamp was incident on the flat

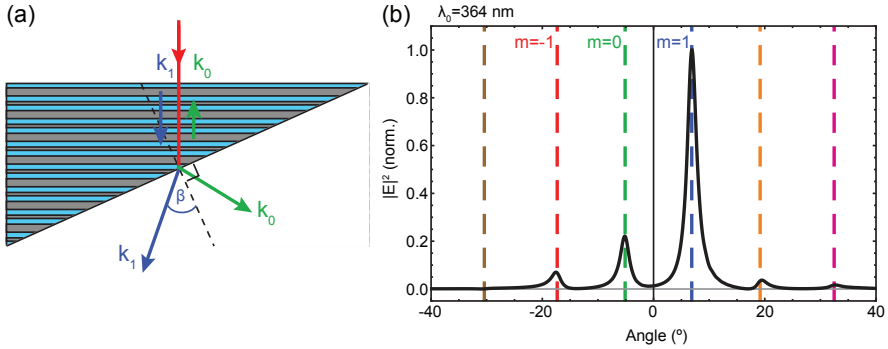

Figure 3.6: a, Sketch of metamaterial prism. The simulated prism consisted of 15 unit cells and had an output facet at 5° from the interfaces. Light is normally incident on the flat side and couples to different harmonics in the multilayer structure. Here, the wave vectors of the $m = 0$ and 1 harmonics are shown schematically. The harmonics refract with different angles due to the orientation and magnitude of the wave vector. **b**, Finite-difference time-domain simulation of the angular distribution of light refracted from a Ag/TiO_2 multilayer metamaterial prism at a free-space wavelength of 364 nm (layer thicknesses in Table 3.1). Light refracts under well-defined angles from the prism, directly probing the phase velocity inside the prism. The dominant peak, corresponding to the $m = 1$ harmonic, has a positive refraction angle, corresponding to a positive harmonic phase index.

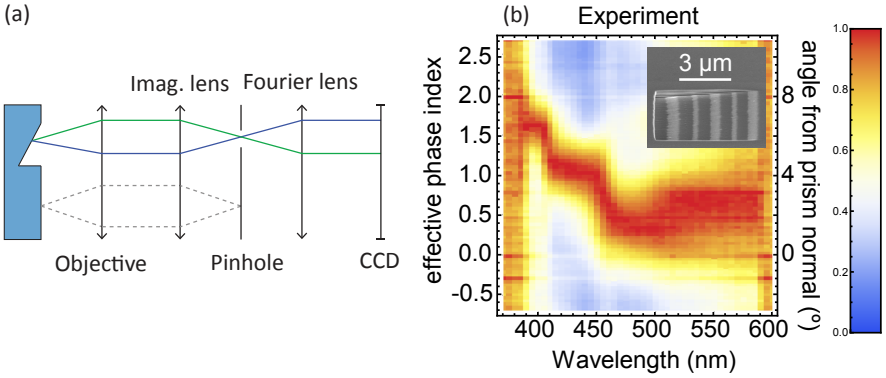

Figure 3.7: a, Sketch of the Fourier microscope used in the experiment. Light transmitted from the sample is filtered using a pinhole after an imaging lens. The back focal plane of the objective is observed by the 2D imaging CCD camera. **b**, Measured normalized light intensity as a function of refraction angle relative to the normal of the sloped side of the prism and as a function of free-space wavelength. The angle is converted to an effective phase index using Snell's law. The inset shows a SEM image of the fabricated microprism. Light refraction is governed by a positive effective index, which increases in a stepwise manner for decreasing wavelength, in agreement with the trend in Figure 3.5b

side of the metamaterial prism. The transmitted light was collected using a 20X 0.45 NA microscope objective, and first spatially filtered using a pinhole in the image plane of the collection objective. The back-focal plane of the objective was then directly imaged onto a Si CCD detector. Figure 3.7b shows the measured normalized angular distribution of refracted light relative to the normal of the output facet. The angular distribution is converted to an effective prism phase index inside the metamaterial using Snell's law. As can be seen, most light is refracted to angles that correspond to a positive effective phase index (ranging from $1.5 > n_{eff} > 0.5$) over the 370−570 nm spectral range: for decreasing wavelength the index is increasing to progressively larger values in a stepwise manner similar to the calculation in Figure 3.5b. The stepwise behavior is caused by the fact that the magnitude of the real part of the Bloch wave vector remains approximately constant when the frequency is at the band edge. As the refraction angle is determined by the parallel projection of the wave vector, this leads to a constant refraction angle between 410 and 450 nm.

Finally, we note that the fact that the phase index cannot be uniquely defined for the multilayer stack does not prevent flat lensing. [64–67] The spatial phase profile at the exit interface of the metamaterial that results in the construction of an image at a position beyond the slab of a point source at the entrance interface is the same for every harmonic, as it is related only to the curvature of the IFC, which is the same for every harmonic; see Figure 3.1d. This is comparable to using the curvature of the hyperbolic dispersion of anisotropic right-handed media for imaging. [64, 67] Flat lensing, which has been experimentally observed by Xu et al. for the layer geometry studied here, thus, is the result of image reconstruction due to the coherent superposition of refracted light from multiple harmonics in the metamaterial. The image is formed due to negative refraction of energy, invoked by the shape of the isofrequency contour and not by the left-handed nature of the fundamental harmonic. As demonstrated above, light propagation is dominated by right-handed harmonics with a positive phase index.

3.4 Conclusions

We have studied the propagation of light in the $300-500$ nm spectral range in a double-periodic Ag/TiO_2 multilayer metamaterial. Based on calculations and simulations we conclude that light propagation in the metamaterial is governed by multiple harmonics with either a positive or negative phase index. We find that positive index ("right-handed") harmonics dominate in the wavelength range of interest. More than half of the energy is carried by positive-index harmonics. Flat lensing in the material is the result of the coherent superposition of multiple refracted harmonics, dominated by "right-handed" harmonics, and is similar in nature to that of hyperbolic metamaterials. Nonetheless, there is a marked difference between hyperbolic metamaterials and the geometry considered here; the effective optical properties are determined by coupling to negative index waveguide modes. Our work is confirmed by experiments and numerical simulations on a

multilayer metamaterial microprism from which the multiple refracting harmonics are directly resolved, with a positive-index harmonic dominating. The striking differences between individual harmonics of the same Bloch waves require careful consideration, not only for the metamaterial design outlined in this work, but more generally for other periodic metamaterials as well.

4

Planar single periodic metal/dielectric multilayer UV flat lens

We demonstrate a flat lens formed by a multilayer stack of 53 nm silver and 25 nm titanium dioxide films. The multilayer stack is designed to exhibit negative refraction of energy in the UV (λ_0 = 364 nm) spectral range. The metal and dielectric multilayer stack is fabricated using physical vapour deposition. Confocal microscopy is used to directly observe the image of a narrow slit formed above the lens surface, 790 nm from the object. The lens focus has an in-plane full width half maximum of 350 nm, in good agreement with calculations. Near field scanning optical microscopy measurements are performed to observe the 2D image of a 10 μm long slit. The simple planar multilayer design has several unique features such as a submicron thickness, the absence of an optical axis, and a lens-image separation in the 100 nanometer range.

4.1 Introduction

The refraction of light at an interface between two dielectrics is determined by the refractive index of the two media. A simple and elegant law, drafted by the Dutch scientist Snellius in the 17th century, relates the incident and outgoing angles of light at an interface to the ratio of the two refractive indices:

$n_1/n_2 = \sin(\theta_2)/\sin(\theta_1)$. Snell's law is valid for any refractive index provided by natural materials, typically in the range $n = 1.0 - 4.5$. Most recently, this range of indices has been expanded, with the advent of optical metamaterials: engineered composite materials of which the effective optical properties are determined by the bulk properties of the constituent materials in combination with a suitably designed sub-wavelength material architecture [68]. For example, a metamaterial composed of a sub-wavelength stack of dielectric rods can have an effective refractive index near zero [69]. An array of metal/dielectric thin films can be characterized by an effective permittivity close to zero, as was shown in Chapter 2. Also, materials with an effective index that is negative have been experimentally realized [8–10]. Even for these new materials with an unusual refractive index Snell's law still describes how light is refracted at an interface.

In the 1960s, Veselago realized that, given Snell's law, a thin slab of negative-index material would act as a flat lens [5]. Light incident from free space on a negative-index material slab will show negative refraction (i.e. refraction towards the same side of the surface normal as the incident beam, see Fig. 4.1a), at both the incoming and the outgoing interface. As a result, an initially diverging beam of light originating from an object refracts at the flat lens surfaces and will leave the negative-index slab as a converging beam, creating a focus on the other side. Such a lens design has many appealing aspects. First of all, it enables the lens to be very thin, as opposed to a conventional lens that operates based on the refraction of light at a convexly or concavely shaped lens surface, and which typically has a thickness in the millimeter range. In contrast, a flat negative-index lens will create a focus even if it is only a wavelength thick. Second, the object does not have to be placed at the focal length to obtain an image, but rather can be placed over a range of distances from the lens. Third, for a negative-index flat lens the image is a linearly translated copy of the object, while for a conventional lens the image has an inverted orientation. And fourth, a flat lens has no fixed optical axis, so an entire 2D plane can be imaged.

Optical metamaterials showing negative refraction have been demonstrated by several groups, first in the microwave range [7, 8], and later in the infrared [9, 10] and near-infrared spectral range [11]. Such materials are sometimes also referred to as "left-handed" metamaterials, as the E, H and k vectors form a left-handed system. These materials were made using resonant plasmonic nanostructures such as split ring resonators and fishnet structures. An alternative metamaterial design, based on coupled plasmonic waveguides arranged in a metal/dielectric multilayer stack was designed by Verhagen et al. [21] This geometry operates at much shorter wavelength, in the blue and ultraviolet spectral range, and exhibits negative refraction and flat lensing [57] for TM polarized light.

Hyperbolic metamaterials (HMMs) also show negative refraction [67, 70–73]. The effective permittivity of these metamaterials is anisotropic, with a tangential and longitudinal permittivity of opposite sign. This anisotropy leads to a hyperbolic dispersion relation describing light propagation through the metamaterial. The occurrence of negative refraction is easily visualised in a wavevector diagram (see

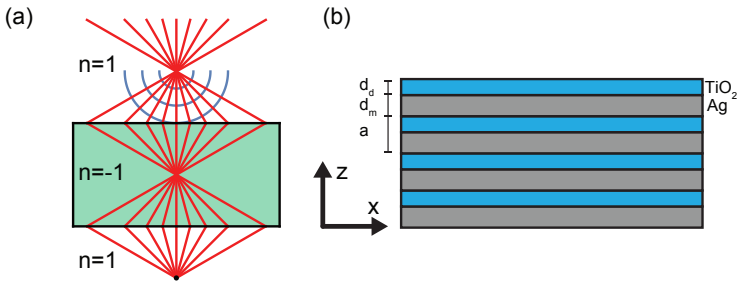

Figure 4.1: a, Sketch of a flat lens formed by a hypothetical $n = -1$ material. **b**, Schematic of the multilayer metamaterial structure considered here; gray layers correspond to Ag, with thickness d_m and blue layers to TiO_2 with thickness d_d. The unit cell size is defined as a.

Fig. 1.2c). The permittivity tensor is:

$$\overleftrightarrow{\epsilon} = \begin{pmatrix} \epsilon_t & 0 & 0 \\ 0 & \epsilon_t & 0 \\ 0 & 0 & \epsilon_z \end{pmatrix} \tag{4.1}$$

where $\epsilon_t \epsilon_z < 0$. The dispersion relation is given by $k_0^2 = k_z^2/\epsilon_t + k_x^2/\epsilon_z$. For a metal dielectric stack with a deeply sub-wavelength unit cell size, ϵ_t and ϵ_z are given by effective medium theory as; $\epsilon_t = (\epsilon_d d_d + \epsilon_m d_m)/(d_d + d_m)$ and $\epsilon_z = ((\epsilon_d^{-1} d_d + \epsilon_m^{-1} d_m)/(d_d + d_m))^{-1}$ [24, 74]. Figure 4.1b shows a sketch of the geometry considered in the following; an Ag layer of thickness d_m and a TiO_2 layer of thickness d_d form the unit cell of the periodic multilayer.

Figure 4.2a shows the calculated wavevector diagram $k_z(k_x)$ obtained from the effective medium theory (red) for an infinite Ag/TiO_2 multilayer stack with very thin layers (the unit cell size is $a = d_m + d_d = 1$ nm, with $d_m = 3d_d$) for a freespace wavelength of 364 nm. We take measured values for the permittivity of Ag ($\epsilon_m = -1.762 + 0.269i$), and TiO_2 ($\epsilon_d = 7.270 + 0.163i$) at $\lambda_0 = 364$ nm. First, we assume the lossless case, so we neglect the imaginary parts. The Bloch wavevector corresponding to this multilayer structure is determined as a function of parallel wavevector momentum k_x using transfer matrix calculations (green). This result agrees very well with effective medium theory. The arrows drawn in Fig. 4.2a indicate the constructed refraction using this wave vector diagram for light incident from air at 30° on a semi-infinite region of this HMM geometry. As parallel wavevector momentum is conserved, the intersection of the dashed line in Fig. 4.2a with the isofrequency contour gives the refracted wavevector k_{refr} (red). The Poynting vector S_{refr} (purple) direction is given by the derivative $\partial\omega/\partial k$, which is normal to the tangent at this point. This direction is determined by calculating the wavevector diagram at different λ_0 (not shown). As can be seen, the Poynting vector is oriented in the negative x direction, indicating negative refraction of energy.

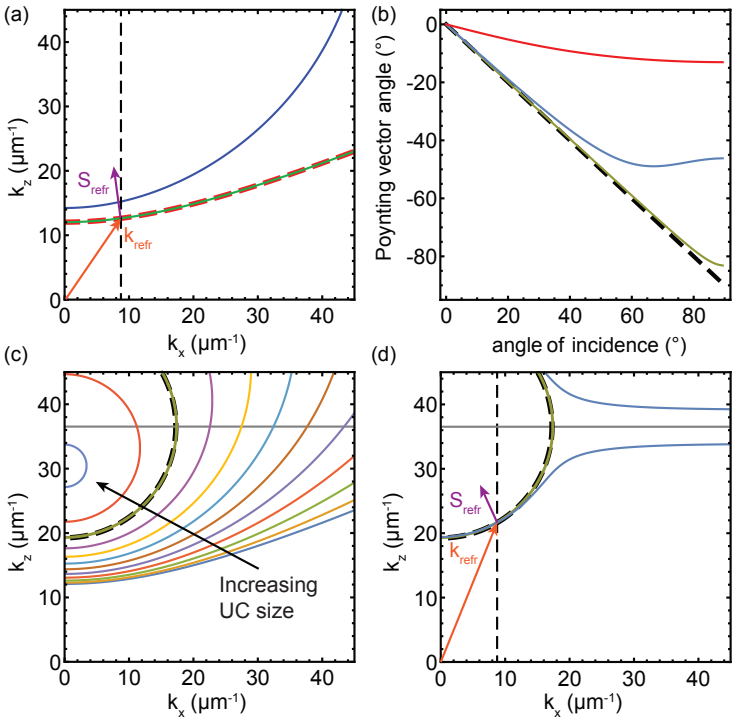

Figure 4.2: **a**, Hyperbolic IFC calculated for λ_0 = 364 nm (k_0 = 17.3 μm^{-1}) described by effective medium theory (red), a periodic Ag/TiO_2 multilayer structure with a 1 nm unit cell (green), with $d_m = 3d_d$ and excluding losses. Increasing the unit cell to 50 nm bends the IFC away from a hyperbole (blue). The vertical dashed line corresponds to the parallel momentum of a plane wave in air incident at 30°. The Poynting vector shows negative refraction. **b**, Calculated Poynting vector angle for the hyperbolic metamaterial (red), ideal spherical IFC (green) and realistic geometry including losses (blue). The black dashed line corresponds to the ideal case $\theta_{refr} = -\theta_{inc}$ **c**, Increasing the unit cell size from a = 1 nm to a = 100 nm changes the curvature of the IFC. For a unit cell size of a = 86.0 nm, with d_m = 64.6 nm and d_d = 21.4 nm the curvature is spherical, with a radius equal to k_0 (black dashed curve). **d**. Including losses, the IFC changes shape (blue, green is lossless from c), but up to large angles (55°) the curvature is the same.

The Poynting vector angle (−7°) strongly deviates from the incident angle (30°). Fig. 4.2b shows the calculated refraction angle as a function of angle of incidence for the HMM (red line). The ideal case, required for flat lensing, given by $\theta_{\text{refr}} = -\theta_{\text{inc}}$ is indicated by the black dashed line. As is clear from the figure, a HMM does not satisfy this requirement. This makes a hyperbolic metamaterial design unsuitable to realize a flat lens, as it would exhibit strong aberrations, leading to a poorly defined focus [50, 75, 76].

To solve this problem, we investigate the effect of increasing the unit cell size. Figure 4.2a (blue) shows the IFC for a HMM in which the unit cell size is increased by a factor 50. Now, the IFC no longer agrees with the effective medium result. The deviation is more pronounced for large wavevectors, as then the internal field is more sensitive to the microscopic structure of the metamaterial. Fig. 4.2c shows how the IFC changes when gradually increasing the unit cell size from 1 to 100 nm, maintaining the ratio of metal and dielectric thickness fixed. The curve transforms from hyperbolic to spherical, centered around the band edge, $k_z = \pi/a$. Interestingly, if the layer thicknesses and material permittivity are chosen correctly, the curvature of the IFC can be matched very well to that of free space, given by a circle of radius $k_0 = 2\pi/\lambda_0$ (dashed line). At a wavelength of $\lambda_0 = 364$ nm, the optimum is found for $a = 86.0$ nm, with $d_m = 64.6$ nm and $d_d = 21.4$ nm. The realized spherical IFC implies that for all incident angles energy will be refracted with a negative angle equal in magnitude to the positive angle of incidence. The green line in Fig 4.2b shows the calculated Poynting vector angle for the optimum geometry. The angular response is indeed very close to the ideal curve for a large range of angles.

The IFC of this metamaterial design is fundamentally different from the IFC of the coupled waveguide design [21, 57]. There, the IFC of the fundamental harmonic is also spherical in shape, but oriented around the origin of the wavevector diagram. For the new design proposed here, the IFC is centered around the band edge. This means that in our design no guided modes exist along the metal/dielectric interfaces. However, for the purpose of creating a flat lens, the response is the same, with the exception that our new design has a phase difference between object and image, as will be discussed further on.

It should be noted that a similar multilayer geometry was considered earlier [77]. In that work, the IFC was also designed to be spherical, but with a radius of curvature larger than that of freespace. This has the advantage of also allowing the propagation of evanescent waves, which are attenuated in our design. However, a flat lens with such an IFC has aberrations, and can only produce a partial focus.

The above calculations were performed for lossless materials. Next, we consider realistic material losses, taking into account the complex permittivity of Ag and TiO_2. Fig. 4.2d shows the IFCs of this lossy multilayer geometry with layer thicknesses $d_m = 64.6$ nm and $d_d = 21.4$ nm (blue). The lossless case is also plotted again for reference (green). As can be seen, the IFC is nearly spherical for $k_x < 14\,\mu m^{-1}$, corresponding to an angle of incidence of about 55°. At larger angles, the IFC significantly deviates from the spherical shape. In this wavevector regime, most of the field is localized in the metal layers, which are strongly absorbing. The

calculated Poynting vector angle for this geometry is shown in Fig. 4.2b (blue). As expected, it is very close to the ideal curve (black dashed) for angles of incidence below 55°.

To evaluate the imaging performance of this metamaterial design, we investigate the precise shape of the IFC, and define the deviation from an ideal spherical IFC as:

$$D = \frac{1}{k_0} \int_0^{k_0} |\pi / a - \sqrt{k_0^2 - k_x^2} - k_{Bl}(k_x)| dk_x \tag{4.2}$$

Figure 4.3 shows the value of D as a function of metal and dielectric layer thickness. As can be seen, there is a wide band of combinations of d_m and d_d for which D is very low. All points on this band lead to an IFC with a curvature very close to that of free space, corresponding to an angle-independent response. This emulates the negative refraction observed in a $n = -1$ material for propagating waves, and enables the realization of a flat lens.

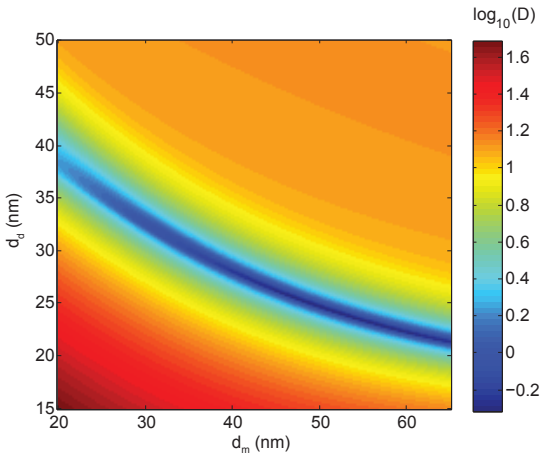

Figure 4.3: Plot of deviation D from the ideal IFC curve as a function of metal (d_m) and dielectric (d_d) layer thickness. Optimization of the layer thicknesses reveals a broad band of combinations of metal and dielectric layer thicknesses achieving an isofrequency contour which is very close to ideal (blue). These structures have an IFC with a spherical shape and radius k_0.

4.2 Poynting vector angle

Analysis of the Poynting vector angle as above strictly holds only for lossless and infinitely periodic structures [30]. To investigate how light refracts and propagates in a lossy, finite sized, multilayer system, we calculate the Poynting vector angle

from the lateral shift of a quasi plane wave propagating through the flat lens. It has been shown that the lateral shift is proportional to the derivative of the phase of the transmitted electric field with respect to the parallel wavevector component [60, 74, 78]: $\Delta = \partial(-\arg(t(k_x)))/\partial k_x$, where the phase is given by the argument of the transmission coefficient t. The Poynting vector refraction angle is then defined as $\tan(\theta_t) = \Delta/L$, where L is the total slab thickness.

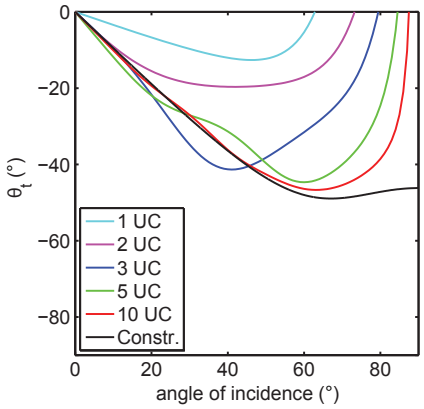

Figure 4.4: Construction of the Poynting vector angle from $S \parallel \partial\omega/\partial k$ for the ideal geometry with losses (black). The colored lines correspond to the Poynting vector angle defined as $\tan(\theta_t) = \Delta/L$, where Δ is the lateral shift and L is the total slab thickness, calculated for a changing number of unit cells (UC).

Figure 4.4 shows the result of this calculation. The Poynting vector angle is calculated for a different number of unit cells in the range 1-10. The Poynting vector angle constructed from the IFC is shown for reference (black). As can be seen, when only one or two unit cells are considered the refraction angle deviates significantly from the curve obtained from the IFC. For a larger number of unit cells (≥ 5), both analyses yield quite similar results for angles up to 60°. This further confirms that the metamaterial structure exhibits negative refraction when losses and a finite structure are taken into account. The deviations in Fig. 4.4 for the case of a small number of unit cells are due to multiple reflections inside such a finite slab; for a larger metamaterial thickness the back reflected waves are attenuated by absorption. Note that calculating the Poynting vector angle directly from the microscopic fields will neglect the macroscopic magnetization and therefore give a different result [79–81].

4.3 Phase condition

In the previous section, we have shown how energy refracts negatively, allowing flat lensing. Apart from the direction of energy propagation, indicated by the Poynting vector, the direction of phase propagation, indicated by the wave vector, is also critical to realize a flat lens as the interference at the focal point should be constructive for all angles of incidence. If we first consider a hypothetical slab of left-handed ($k \cdot S < 0$) $n = -1$ material, as Veselago did originally, it is easy to see how this condition is fulfilled. Figure 4.5 shows a sketch of the geometry. Light is emitted from a source at (x_s, z_s), and propagates with angle θ_i towards the $n = -1$ slab. Parallel wave vector conservation over the $n = 1/n = -1$ interface completely determines refraction. From the construction it is clear that $L = d_s + d_i$, with L the lens thickness, d_s the lens-source separation, and d_i the lens-image separation. The wave vector k_{mm} inside the slab is oriented exactly anti-parallel to the direction of propagation of energy. If we decompose the phase advance, the lateral x-component drops out, as there is no net propagation in that direction. The total phase advance in the longitudinal z-direction is also zero, as the vertical component k_z changes sign inside the slab; $k_z = -\sqrt{k_0^2 - k_x^2}$. Therefore the positive phase advance $\phi_a = k_z(d_s + d_i)$ in the air region is compensated by the negative phase accrue in the $n = -1$ slab; $\phi_s = -k_z L$. Following the construction in Fig. 4.5, it is clear the phase at the image position (x_s, z_i) is equal to the phase at the source position (x_s, z_s): $\phi_t = \phi_a + \phi_s = 0$.

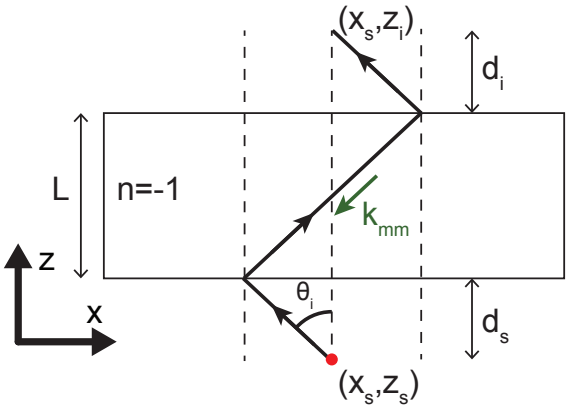

Figure 4.5: Sketch of the propagation of light from a source (red) through a hypothetical $n = -1$ metamaterial slab. Negative refraction occurs over the air/$n = -1$ interfaces, and in the $n = -1$ slab the phase (indicated by k_{mm}) is propagating anti-parallel to energy (black arrows). The total slab thickness L is equal to the sum of the lens-source separation d_s and the lens-image separation d_i.

From Fig. 4.2d we can evaluate the relative orientation of k and S in the mul-

tilayer structure. As is clear, $k \cdot S > 0$ for all angles, so this metamaterial is right-handed. However, when the IFC of the multilayer geometry is spherical, the structure can fulfil the condition of constructive interference at the image position. In the wavevector diagram k_z is given by $k_z = k_{Bl} + \frac{2\pi}{a}m$. Here, k_{Bl} is the Bloch wave vector, m is an integer corresponding to the Bloch wave harmonic [82], and a is the unit cell size. In the ideal case we can simplify $k_{Bl} = \pi/a - \sqrt{k_0^2 - k_x^2}$. The total phase advance from source to image will then be: $\phi_t = k_z(d_s + d_i) + (\pi/a - \sqrt{k_0^2 - k_x^2} + \frac{2\pi}{a}m)L$. If the multilayer structure is constructed from an integer number of unit cells; $L = ja$, then $\phi_t = \pi j(1 + 2m)$. The phases in source and image thus differ by πj. Importantly, the phase difference is independent of angle, and therefore interference at the image position is constructive.

The analysis above indicated that although light propagation through the metal/dielectric multilayer is very different from propagation through a hypothetical homogeneous $n = -1$ slab, it will act as a flat lens. In the next section, we show how we fabricate and characterize this multilayer lens.

4.4 Sample fabrication

The optimized metamaterial geometry was designed for a wavelength of operation of λ_0 = 364 nm, with d_m = 53.2 nm and d_d = 25.0 nm. These layer thicknesses are slightly different than those in section 4.2, as they are optimized for the dielectric constants observed for the deposited layers. We deposit multilayer stacks consisting of an integer number of unit cells using physical vapor deposition (PVD). Here, a 10 kV electron beam is used to heat Ag and Ti_3O_5 pellets placed in separate crucibles. During deposition, the layer thickness is monitored using a quartz crystal thickness monitor, which we calibrated by depositing single films on separate Si substrates. The optical constants and thickness of these individual reference layers were then measured using spectroscopic ellipsometry. After this calibration a complete multilayer stack is deposited. Figure 4.6a shows a scanning electron microscope (SEM) image of a cross section of a 4-unit-cell stack deposited on a SiN film on Si, made using focused ion beam (FIB) milling. The bright bands correspond to the Ag layers, and the darker bands to TiO_2. The multilayer was covered with Pt before milling to obtain a clear cross section.

Figure 4.6b shows an optical microscope image of a multilayer stack deposited on top of a 50 nm thick silicon nitride membrane (Norcada NX5025A), which has a clear window of 250 μm × 250 μm, allowing optical transmission measurements. Before deposition of the multilayer stack, the SiN membrane was first covered with 800 nm of MMA and 80 nm of PMMA. Patches of 25 μm by 25 μm were then exposed using electron beam lithography and developed using MIBK:IPA. This allows us to lift off part of the deposited multilayer structure, in order to obtain a reference in the flat lens experiment. The rear side of the silicon nitride membrane was sputter-coated with 150 nm of Cr, acting as an optically thick masking layer. FIB

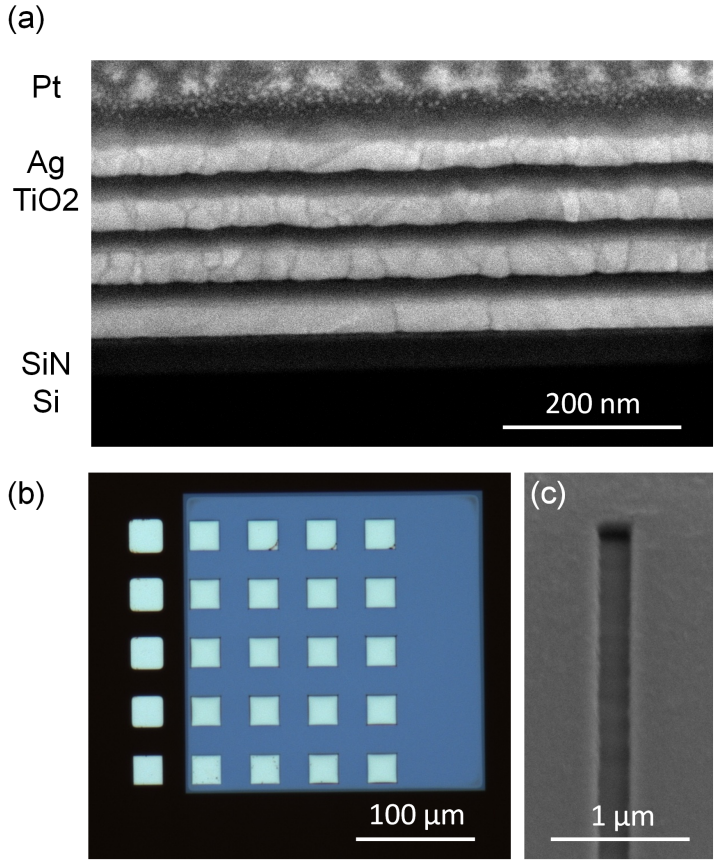

Figure 4.6: **a**, SEM image of a cross section of a fabricated multilayer structure. Four unit cells of Ag (light) and TiO_2 (dark) are clearly visible. The top TiO_2 layer is capped by Pt to make the FIB cross-section. This sample was studied using NSOM. **b**, Optical microscope image of multilayer structures (25 × 25 μm) deposited on a SiN membrane window. The other regions of the multilayer stack are removed by lift off. The opposite side of the membrane window is coated with a Cr masking layer, in which slits are written using FIB, acting as an object. This sample was studied using confocal microscopy. **c**, SEM image of a 200 nm wide slit in the Cr masking layer. The underlying SiN is exposed.

milling was then used to create 100 nm wide and 10 μm long slits through the opaque Cr layer. Figure 4.6c shows a SEM image of a slit through the Cr masking layer. These slits serve as the objects for the flat lens: the light scattered by the slit propagates through the thin SiN membrane, and is then negatively refracted by the flat lens. A focus is formed in the air region above the flat lens, establishing an image. As a reference, we have also written slits in the Cr layer at positions of the membrane where the deposited multilayer stack was lifted off. Here, the scattered light propagates through the 50 nm SiN, and then further diverges in free space.

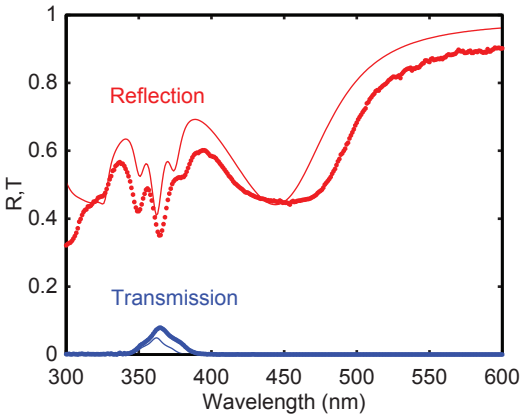

Figure 4.7: Measured reflection (red) and transmission (blue) of fabricated 4-unit-cell Ag/TiO_2 multilayer deposited on a glass microscope slide. The thin solid line corresponds to the calculated result, based on deposited layer thicknesses and optical constants. A slightly lower reflection and higher transmission is observed in the experimental data, which is attributed to surface roughness in the metal layers.

To study the optical properties of the fabricated multilayer, we perform specular reflection and transmission measurements at an angle of incidence of 20° on a multilayer sample consisting of four unit cells deposited on a glass microscope slide. Figure 4.7 shows the measured data (dots). Overall, the trends in the observed reflection and transmission spectra agree very well with the data from a transfer matrix calculation (thin lines). These calculations used layer thicknesses and optical constants experimentally determined from spectroscopic ellipsometry measurements on individual reference layers. The differences in absolute values are attributed to surface roughness, especially in the thin metal films, which is inherent in the PVD process. Scattering from this roughness is not taken into account in our calculations.

4.5 Experiments

To characterize the focusing properties of the metal dielectric multilayer stack, we measure the image of the slit milled in the Cr film on the other side of the SiN membrane. The total lens thickness is 390 nm, and the distance from the object to the lens is 50 nm (the SiN membrane thickness). Therefore we expect a lens-image separation of 340 nm. We use a Witec alphaSNOM confocal microscope to weakly focus λ_0 = 364 nm light from an Ar ion laser on the object slit (see Fig. 4.8a). The transmitted light is imaged on a fiber core (25 μm diameter), and sent to a spectrometer. The sample is scanned using a piezo-electric stage in the x-direction, normal to the slit. The incident beam and collection objective are kept fixed, such that the lateral transmission dependence is probed. Furthermore, the upper microscope body is scanned in height, to determine the vertical dependence of the image plane. The transmitted light is collected using a 100x objective (Zeiss Epiplan-NEOFLUAR 100X/0.9) providing a lateral resolution of approximately 200 nm at λ_0 = 364 nm. The result of this confocal measurement can be seen in Figure 4.8b. A clear focus is observed, confirming that the single-periodic multilayer structure acts as a flat lens. The minimum width of the focus coincides with a maximum in transmitted amplitude. We analyze the focal shape by taking a line cut for fixed microscope z-axis height. A Gaussian profile is fitted to the recorded signal, which is a good approximation to the focus shape near the focal position. The minimum full width half maximum (FWHM) we find is approximately 350 nm. As a comparison, we use analytical Green's tensor calculations in a multilayer structure to calculate the spatial field formed by a horizontal dipole placed below the multilayer structure, and find a very similar FWHM. Furthermore, using Lumerical FDTD we have simulated the effect of changing the slit width, and see no significant change in the FWHM for a slit width below 200 nm.

To determine the vertical position of the focus above the lens surface, we image two object slits in a single scan. The first object slit is positioned underneath the flat lens. The second object slit is positioned at a region of the SiN membrane where the multilayer structure has been lifted off, as indicated by the sketch in Fig. 4.8a. By measuring the transmitted light from both slits in a single scan, we can accurately determine the focal position relative to the lens surface. Figure 4.9a shows the result of such a scan, with the amplitude plotted on a logarithmic scale. Light from the reference slit is much more intense as it is directly transmitted (left), whereas the light from the slit underneath the lens is partially reflected and partially absorbed, reducing the transmitted light intensity (right). The spatial intensity distribution is analyzed by taking line cuts through the data at a fixed height z. Figure 4.9b,c show the normalized fitted amplitude and Gaussian width of both the reference (red) and the sample (blue) signal. As can be seen, the maximum amplitude and minimum width correspond to the same position for both reference and sample. Taking the peak in amplitude and minimum in width of the reference signal as the height where the object slit is in focus, we find that the focus formed by the flat lens is positioned 790 nm away from the object, which is 350 nm above the top

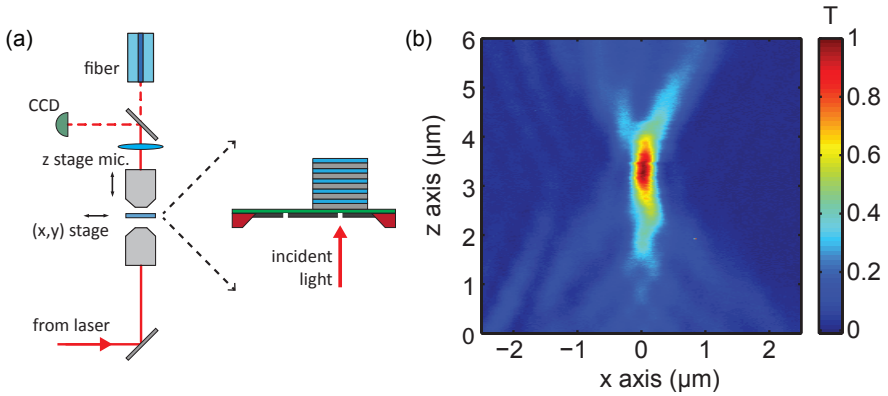

Figure 4.8: a, Sketch of the confocal microscope setup. The incident beam is weakly focussed on the object slit. The sample stage is scanned in the lateral x direction. The top collection arm of the microscope body is scanned in the vertical z direction. **b**, Normalized transmission as a function of lateral sample position x and vertical microscope body position z. A clear image of the slit is observed.

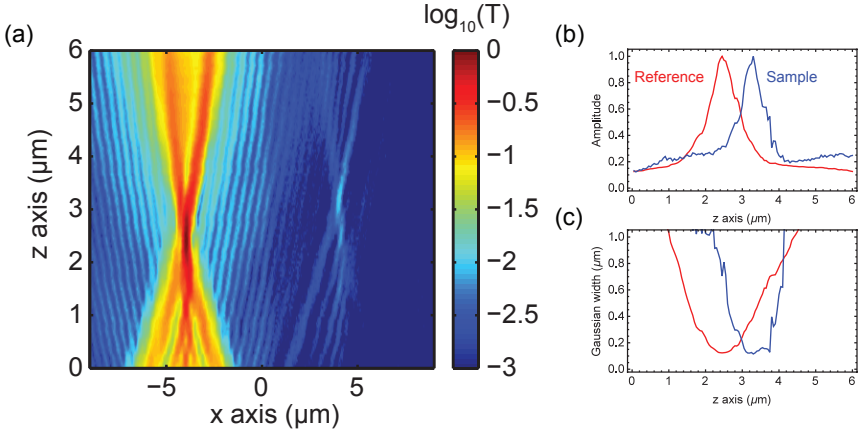

Figure 4.9: a, Confocal scan ($\lambda_0 = 364$ nm) of the signal of a reference slit (left) and sample slit (right) above the multilayer metamaterial. The normalized transmitted signal is plotted on a $\log_{10}$ scale. There is a large amplitude difference between reference and sample due to the reflection and absorption of the multilayer stack. Normalized amplitude (**b**) and width (**c**) of the fitted Gaussian profile as a function of z. A clear vertical offset of 790 nm is observed between the reference (red) and sample (blue) signal; the corresponding distance between lens surface and focus is 350 nm.

lens interface. This is agrees very well with the lens-image separation of 340 nm, calculated using $L = d_s + d_i$.

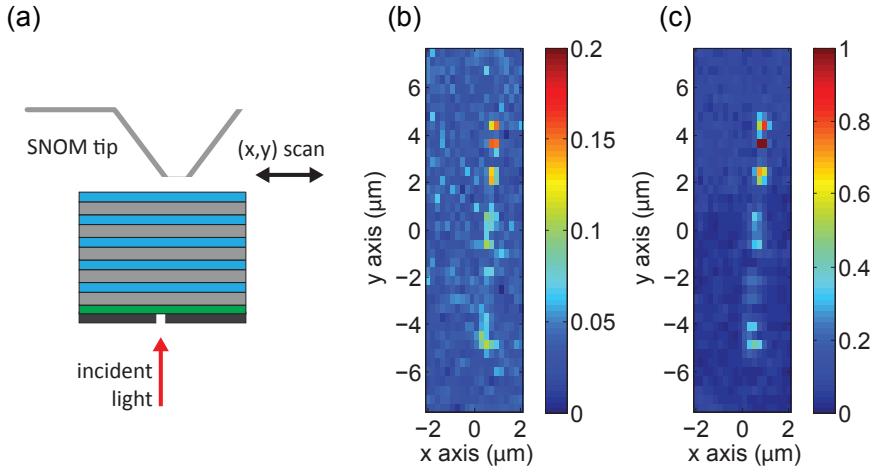

Figure 4.10: **a**, Sketch of the near field scanning optical microscope experiment. The sample is scanned beneath the hollow Al tip. **b**, Spatial image of the transmitted light intensity, at λ_0 = 364 nm, and with the NSOM tip in contact with the flat lens. Almost no signal is observed. **c**, The same spatial scan, with the NSOM tip suspended 220 nm above the flat lens. An image of the object slit is observed. Note the difference in intensity scales between (b) and (c).

To study the spatial structure of the transmitted signal in further detail, we perform near-field scanning optical microscopy (NSOM) using a hollow Al tip with a 150 nm diameter aperture (Witec). Figure 4.10a shows a sketch of this experimental geometry. The multilayer structure for these experiments was composed of four unit cells, with d_m = 57.3 nm and d_d = 25.8 nm. Calculations show that a focus is expected 190 nm above the lens surface. First, we position the near-field tip in contact with the multilayer surface, and scan the sample in the (x, y) dimensions. Figure 4.10b is a spatial map of the transmitted intensity. A contour of the slit geometry is observed, but at very low intensity. Next, the tip is retracted from the surface, and is suspended approximately 220 nm above the surface (as determined from the force-distance curve of the tip) and the same lateral scan is performed (Fig. 4.10c). When compared with the scan in contact mode, the signal-to-noise level is much higher. This is consistent with the expectation that the tip is closer to the image plane above the flat lens.

As is clear from Fig. 4.10c, the transmitted intensity shows strong variations across the slit length. We attribute these variations to scattering from Ag grains within the multilayer stack. Such grains are evident in the SEM image of the cross-section (Fig 4.6a). To optimize the flat lens, the Ag deposition conditions could be

fine tuned to reduce the effect of this grain structures. Recent work, using template stripping [83], using an adhesion layer [84, 85] or sputter coating at high deposition rates on a heated substrate [86], show that smoother Ag films can be experimentally realized.

4.6 Conclusions

In conclusion, we designed a planar multilayer geometry that acts as a flat lens. We use a hyperbolic metamaterial formed by a Ag/TiO_2 multilayer stack with a very small unit cell size as a starting point, and gradually increase the unit cell size far above the effective medium approximation limit. Using properly chosen layer thicknesses the isofrequency contour can be designed to be spherical in shape, with a radius equal to that for the contour in free space. This geometry shows all-angle negative refraction, and can therefore act as a flat lens. An optimized flat lens geometry based on a Ag/TiO_2 multilayer stack, with layer thicknesses $d_m = 53.2$ nm and $d_d = 25.0$ nm, is fabricated using physical vapor deposition. We use confocal microscopy at $\lambda_0 = 364$ nm to study the spatial shape of the image of a linear object slit placed below the flat lens. A clear focus is resolved above the lens with a full width half maximum of 350 nm. We find that the image is positioned 350 nm from the lens surface, as expected. Near-field scanning optical microscopy confirms the image is formed above the lens. The single-periodic design is fundamentally different from the double periodic design demonstrated earlier that is based on coupled plasmonic waveguides, and it is easier to fabricate. The flat lens has properties unlike normal lenses; such as the absence of an optical axis, it has a submicron thickness, and the ability to form an image in the 100 nm range from the lens surface.

5

Dielectric metamaterial anti-reflection coating for stratified media

We present the use of a dielectric metamaterial as a coupling layer to guide an incident plane wave into a planar metal-dielectric multilayer waveguide metamaterial with 100% efficiency at a single wavelength. We optimize the reflectivity of the interfaces between air, dielectric coupling layer and metal-dielectric waveguide metamaterial by properly designing and positioning the dielectric metamaterial which forms the coupling layer, to achieve destructive interference eliminating all reflection. Furthermore, we show how this coupling layer is efficient for a large range of angles of incidence.

5.1 Introduction

Optical metamaterials, structures of which the effective properties are derived from sub-wavelength elements, have attracted a lot of attention recently[68, 72]. One example of a metamaterial geometry is a stack formed by thin/metal dielectric multilayers. Such a geometry can be used to fabricate hyperbolic metamaterials [28, 45, 87–89], epsilon-near-zero metamaterials [90], or materials with a negative effective index of refraction [21, 56, 82, 91]. In many cases the special dispersive characteristics of these multilayer metamaterials are due to surface plasmon polaritons that propagate along the metal/dielectric waveguide array.

While the effective optical properties of these metamaterials can be very interesting, the coupling of light incident from air into the metal-dielectric waveguides is often quite poor. This is caused by the fact that the spatial electromagnetic field profile of the waveguide modes is not well matched to that of the incident plane wave. Many optical systems use anti-reflection coatings to enhance transmission, which rely on destructive interference between reflected light from the air-coating and coating-medium interfaces. For homogeneous planar media perfect transmission is achieved when the coating has an optical path length of a quarter wavelength and the refractive index equals $n_2 = \sqrt{n_1 n_3}$, where the indices refer to air (1), coating (2) and substrate material (3). However, for multilayer plasmonic waveguide metamaterials this approach does not apply, because using a homogeneous layer does not solve the problem of poor mode overlap.

Here, we propose a geometry consisting of a dielectric multilayer metamaterial oriented parallel to the incident beam, that is designed such that it enhances mode matching to the metamaterial. Using nanoscale structures to enhance incoupling has been demonstrated before [92, 93]; here we use the dielectric metamaterial not only for mode matching, but also as an antireflection interference coating [94]. We use a multilayer geometry because an analytical expression exists to determine the waveguide modes, which are solutions to the interface boundary conditions of the periodic unit cell. These waveguide modes have a specific propagation constant β and field profile. Previously, there has been a lot of work studying light propagation through such multilayer geometries [95–100]. In fact, a metal/air grating was first considered to explain the observed phenomenon of extraordinary optical transmission [101] theoretically [102].

As an example, we investigate the coupling between a plane wave incident from free space and a single-periodic metal-dielectric waveguide array (MDWA) that supports a single propagating, negative-index waveguide mode, to which a plane wave cannot couple at normal incidence. By appropriately designing a dielectric metamaterial as coupling layer we control modal overlap at the interface. By tailoring interference in the dielectric metamaterial layer we achieve a coupling efficiency of 100% at a single wavelength. Furthermore, we investigate how this enhanced coupling depends on the angle of incidence.

5.2 Geometry and coupling

Figure 5.1a shows a sketch of the geometry we consider. A periodic array of thin metal (with thickness d_m and permittivity ϵ_m) and thin dielectric (with thickness d_d and permittivity ϵ_d) layers forms our metamaterial with unit cell size a. We take the direction of periodicity as the x direction, and $x = 0$ to coincide with the center of the dielectric layer of the unit cell. The waveguides are extended in the y direction, and interfaces between different regions are normal to z.

The transmission and reflection amplitudes of a wave impinging on an interface

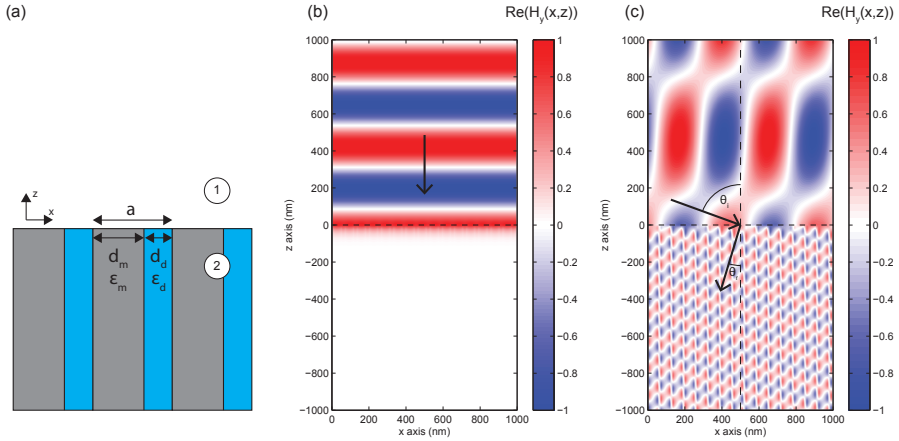

Figure 5.1: **a**, Sketch of metal-dielectric metamaterial geometry. **b**, Calculated field profile due to a plane wave ($\lambda_0 = 450$ nm) incident on the metal dielectric waveguide array ($d_m = 45$ nm, $\epsilon_m = -3.5$, $d_d = 20$ nm, and $\epsilon_d = 2.5^2$) at normal incidence. The spatial field profile shown is composed of 15 repetitions of the unit cell. **c**, Field profile due to a plane wave at an angle of incidence of 70°. Negative refraction is evident in the phase fronts, indicated by θ_i and θ_r.

at $z = 0$ can be calculated by making use of the continuity of tangential fields [103]:

$$\mathbf{E}^{(1)}(z=0) \times \hat{\mathbf{n}} = \mathbf{E}^{(2)}(z=0) \times \hat{\mathbf{n}} \tag{5.1a}$$

$$\mathbf{H}^{(1)}(z=0) \times \hat{\mathbf{n}} = \mathbf{H}^{(2)}(z=0) \times \hat{\mathbf{n}} \tag{5.1b}$$

Here the superscripts refer to the two half spaces. For homogeneous media this yields the Fresnel coefficients, however these cannot generally be applied to non-homogeneous layers. To calculate the reflection and transmission coefficients we expand the field in region j into its eigenmodes $|\psi_n^{(j)}\rangle$:

$$\mathbf{H}^{(j)}(x,z) = \sum_{n=0}^{\infty} a_n e^{i\beta_n z} |\psi_n^{(j)}\rangle \tag{5.2}$$

where β_n is the propagation constant of the n^{th} eigenmode and a_n is its complex amplitude. In free space this is simply the angular spectrum representation of plane waves: $|\psi_n^{(j)}\rangle = \exp(in\frac{2\pi}{a}x)/\sqrt{a}$. In the stratified medium the expansion is performed using the waveguide modes of the geometry, described by a typical field profile $|\psi_n^{(j)}\rangle = H_{y,n}^{(j)}(x)$. The field profile $H_{y,n}^{(j)}(x)$ is found by solving the interface boundary conditions in a periodic unit cell [29, 100]. These modes are defined such

that they are orthonormal under the pseudo-inner product [104, 105]:

$$\langle \psi_m^{(j)} | \psi_n^{(j)} \rangle_\varepsilon = \langle \psi_n^{(j)} | \frac{1}{\varepsilon_j(x)} | \psi_m^{(j)} \rangle = \int_0^a \frac{1}{\varepsilon_j(x)} (H_{y,n}^{(j)}(x))^* H_{y,m}^{(j)}(x) dx = \delta_{nm} \tag{5.3}$$

where $\varepsilon_j(x)$ is the dielectric constant. Using orthonormality, the continuity equation for **H** at the interface between free space and the multilayer waveguide can be written as (see appendix for details):

$$a_k^+ + a_k^- = \sum_{m=0}^{\infty} b_m^+ \langle \psi_k^{(1)} | \psi_m^{(2)} \rangle \tag{5.4}$$

Here a_k^+ and a_k^- are the incident and reflected amplitudes of the k^{th} plane wave, and b_m^+ is the amplitude of the guided mode in the multilayer structure travelling in the forward direction. This equation has two unknowns, a_k^- and b_m^+. A similar equation with the same unknowns can be found for continuity of **E**. Therefore, we can set up a matrix equation [100], where we truncate the expansion to a finite number, and solve for the unknown amplitudes by inverting the resulting matrix (see appendix).

From Eq. 5.4 it is straightforward to see that systems supporting only an anti-symmetric mode can not be excited by a symmetric mode such as a plane wave under normal incidence. In this case the overlap integral is always zero, and therefore the amplitude of the anti-symmmetric mode will be zero. An example of this is shown in Fig. 5.1, where we have designed a MDWA with a single propagating, anti-symmetric waveguide mode which is characterized by a negative mode index. Following the sketch in Fig. 5.1a, for this structure $d_m = 45$ nm, $\epsilon_m = -3.5$, $d_d = 20$ nm, and $\epsilon_d = 2.5^2$ for $\lambda_0 = 450$ nm. All other modes are either evanescent or anomalous [99, 106]. Fig. 5.1b shows the real part of the field distribution $H_y(x,z)$ near the interface, for an incident plane wave at normal incidence, calculated analytically using the aforementioned method. Evanescent modes are clearly visible near the interface; the field in the structure decays exponentially, which indicates that the propagating mode is indeed not excited. Therefore all light is reflected, leading to the standing wave pattern observed in the air region.

To excite an antisymmetric mode the symmetry of the incident wave has to be broken, which can be done by coming in at oblique incidence. Fig. 5.1c shows the calculated field distribution near the interface for a plane wave incident at 70 degrees. Two features are evident: due to a low coupling efficiency at the interface the incident plane wave is partially reflected, leading to the interference pattern observed in the free space region ($z > 0$ nm). Secondly, for this geometry the propagating waveguide mode is excited with a significant amplitude. As the waveguide mode has a negative mode index, the wavefronts visible in the figure refract negatively, as is indicated by the refraction angle θ_r. The waveguide mode index $\beta_1/k_0 = -3.12$ ($k_0 = 2\pi/\lambda_0$), leading to a refraction angle of $\theta_r = -17.5°$.

Figure 5.2a shows the amplitude of $H_y(x)$ along the metal-dielectric waveguide geometry for a single unit cell. The field is antisymmetric over the 20 nm thick dielectric core. This leads to very high field gradients, and limits the efficiency of coupling a plane wave to this waveguide mode. The reflectivity as a function of angle of incidence is shown in Figure 5.2b. As discussed above, $R = 1$ for normal incidence, and around an angle of 70°, incoupling is maximum at approximately 50%.

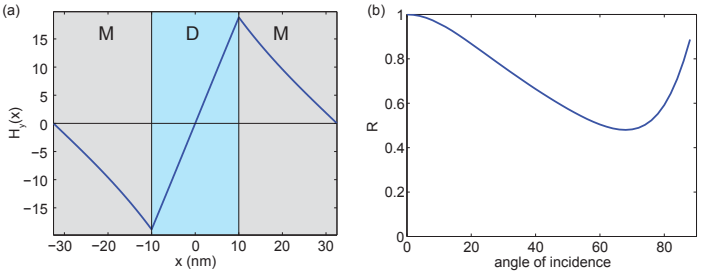

Figure 5.2: **a**, $H_y(x)$ for the negative-index waveguide mode (d_m = 45 nm, ϵ_m = −3.5, d_d = 20 nm, $\epsilon_d = 2.5^2$ and λ_0 = 450 nm). The field profile is anti-symmetric across the dielectric core. **b**, Calculated reflectivity versus angle of incidence. The reflectivity is 1 at normal incidence as the overlap between a plane wave and the anti-symmetric field profile is zero.

5.3 Perfect transmission

To improve the coupling into the MDWA for arbitrary angle of incidence, we use a dielectric metamaterial between the air half space and the MDWA as an intermediate coupling layer to tailor the overlap between the incident field and the MDWA waveguide mode. To achieve perfect transmission, we design the dielectric metamaterial to have a reflectivity at the air/coupling layer interface equal in amplitude to the reflectivity of the coupling layer/MDWA interface. A general expression for the reflectivity of a three layer system is:

$$r_{\text{total}} = r_{12} + \frac{t_{12} r_{23} t_{21} \exp(i n_2 k_0 2 d_2)}{1 - r_{23} r_{21} \exp(i n_2 k_0 2 d_2)} \tag{5.5}$$

Here, the subscripts 12 refer to an interface between medium 1 and 2. It can be shown that perfect destructive interference can be achieved when r_{12} and r_{23} are equal in magnitude, and the thickness d_2 is chosen correctly. Figure 5.3a shows a sketch of the proposed geometry; a multilayer with a high-permittivity dielectric layer with thickness d_{Hi} and permittivity ε_{Hi}, combined with a low-permittivity layer with thickness d_{Lo} and permittivity ε_{Lo}. If we take $\varepsilon_{\text{Hi}} = 4.5^2$ and $\varepsilon_{\text{Lo}} = 1$, we

find only one propagating mode. The field profile is shown in Fig. 5.3b. This mode is clearly symmetric, and as a result it can be excited efficiently from free-space.

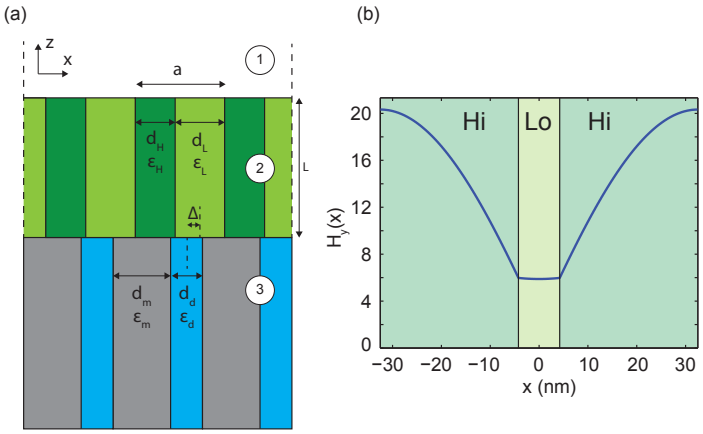

Figure 5.3: a, Sketch of the air / dielectric metamaterial / MDWA geometry. **b**, Field profile of the propagating mode in the dielectric metamaterial.

The unit cell size a of the dielectric metamaterial is matched to that of the metal-dielectric waveguide array ($a = 65$ nm). The filling fraction of the high-index dielectric: $\rho_{\mathrm{Hi}} = d_{\mathrm{Hi}}/a$ is varied, and the reflection coefficient of the air/dielectric metamaterial interface is calculated for every ρ_{Hi} (Fig. 5.4a). The reflectivity gradually changes from $R = 0$ when $\rho_{\mathrm{Hi}} = 0$ towards the reflectivity of a homogeneous layer with $\varepsilon = 4.5^2$ (blue line, $R = 0.4$) as $\rho_{\mathrm{Hi}} \to 1$. In the following, we first take an interface reflectivity of $R = 0.2$ as the desired design (gray dashed line), which corresponds to a filling fraction of $\rho_{\mathrm{Hi}} = 0.87$.

Next, we consider an interface between this dielectric metamaterial in the top half space and the aforementioned MDWA in the bottom half space. Because the propagating mode in the top medium is symmetric, it will not excite the antisymmetric negative index mode if the metamaterials are aligned symmetrically. However, if we introduce a displacement in the multilayer junction, the symmetry is broken and the negative index waveguide mode can be excited. We define this displacement Δ as the shift between the center of the low dielectric layer of the dielectric metamaterial with respect to the center of the dielectric slab in the MDWA (see Fig. 5.3a). Solving this interface problem using the modal expansion technique as in the above showed poor convergence. Gibbs oscillations at the metal-dielectric interface cause high order waveguide modes to have an unphysical high amplitude in the expansion. Therefore, to determine the coupling in this case, we use numerical finite-difference time domain simulations (Lumerical FDTD 8.7.3) to simulate the reflection of the propagating mode in the coupling layer from the interface.

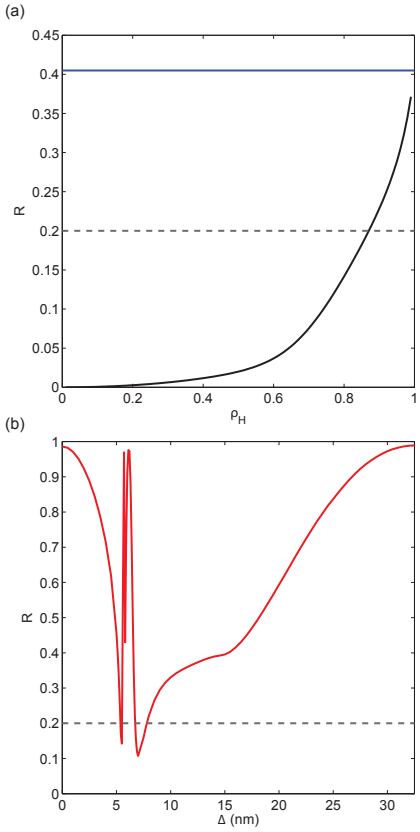

Figure 5.4: a, Reflectivity of the air/dielectric metamaterial interface as a function of high permittivity filling fraction at normal incidence. The permittivity is $\varepsilon_H = 4.5^2$ and $\varepsilon_L = 1$ respectively, and the unit cell size is $a = 65$ nm. **b**, Reflectity of the dielectric metamaterial/MWDA interface as a function of displacement.

The result is shown in Fig. 5.4b, where we plot the reflectivity $R(\Delta)$ as a function of displacement Δ. In the simulations, we use the geometry as described in the above, but now with $\varepsilon_m = -3.5 + 0.01\,i$, where the small imaginary part is required for the stability of the simulations. This small amount of loss in the metal does not significantly affect the coupling process. Note that systems with significant losses can also be treated by the modal expansion method by solving the boundary conditions also in an adjoint system [107].

As is clear from Fig. 5.4b the reflectivity is strongly modulated with displacement, with R in the range of $R = 0.1 - 1$. For a displacement between 5 and 7 nm, we observe very distinct variations in R. At these displacements, the interface between the high and low index region of the dielectric metamaterial crosses the

metal/dielectric interface of the MDWA, leading to strong fluctuations in coupling. At $\Delta = 0$ and 32.5 nm, the dielectric metamaterial is oriented symmetrically with respect to the dielectric core of our MDWA. In this case the overlap between the incident waveguide mode and the field profile of the propagating waveguide mode in the MDWA is zero, so the antisymmetric mode will be not be excited.

By shifting the dielectric metamaterial to $\Delta = 7.8$ nm, we observe an interface reflectivity of $R(7.8\text{nm}) = 0.2$. At this displacement, the coupling layer/MDWA interface reflectivity exactly matches the reflectivity of the air/coupling layer interface in amplitude. The phase shift upon reflection of the first interface may (and generally will) be different from the reflection at the second interface. This phase shift can be compensated for by changing the thickness of the coupling layer. When the reflections from both interfaces are equal in amplitude and π out of phase, destructive interference occurs, leading to zero net reflection. All light is then transmitted into the MDWA.

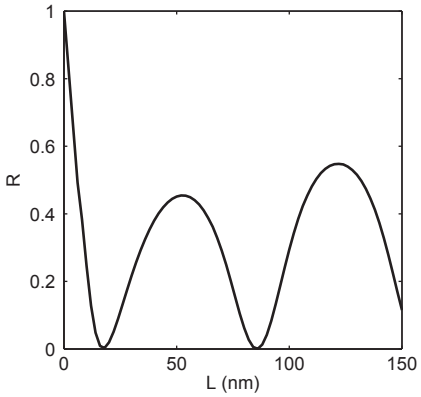

Figure 5.5: Simulated reflectivity (at $\lambda_0 = 450$ nm) of the coupling layer ($\varepsilon_{\text{Hi}} = 4.5^2$, $\varepsilon_{\text{Lo}} = 1$, $\rho_{\text{Hi}} = 0.87$)/ MDWA structure ($d_m = 45$ nm, $\epsilon_m = -3.5 + 0.01i$, $d_d = 20$ nm, $\epsilon_d = 2.5^2$) for $\Delta = 7.8$ nm with changing coupling layer thickness L. Clear oscillations are visible, corresponding to a standing wave in the coupling layer. The two peaks in reflection are not equal in amplitude due to the influence of evanescent waves in the dielectric metamaterial.

Figure 5.5 shows the simulated reflectivity for changing coupling layer thickness. A clear periodic modulation of reflectivity is observed, which is due to a standing wave in the coupling layer, caused by the propagating waveguide mode in the dielectric metamaterial. The amplitude of the peak in reflectivity changes between the two local maxima because evanescent waves in the dielectric metamaterial still contribute for small coupling layer height. The propagation constant of the waveguide mode at $\lambda_0 = 450$ nm in the dielectric metamaterial is $\beta_{DM} = 43.85\mu\text{m}^{-1}$, corresponding to a periodicity in reflectivity of $\pi/(\beta_{DM}) = 72$ nm, in agreement with what is observed in Fig. 5.5. From the figure we can determine the

required coupling layer thickness, and find a vanishing reflection coefficient: $R = 0$ for $L = 86$ nm. For such a dielectric metamaterial design, all light is coupled into the waveguide mode of the MDWA.

5.4 Angle dependence

In the previous section we have shown how a properly designed coupling layer can enhance the coupling into an asymmetric guided mode from 0 to 100%. Calculations were performed for normal incidence, for which no coupling into the MDWA occurs with no coupling layer present. Next, we investigate how the reflectivity of the structure with the coupling layer depends on angle of incidence. We use the same layer geometry as described above.

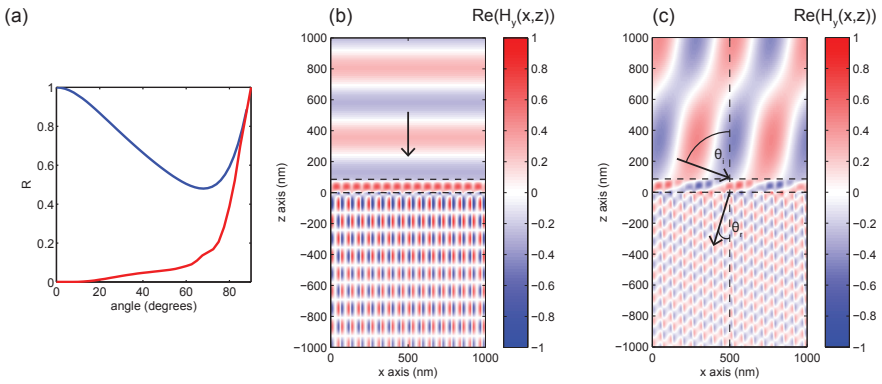

Figure 5.6: a, Reflectivity from the coupling layer on top of the MDWA, as a function of angle of incidence (red). As a reference, the reflectivity of the bare MDWA is also shown (blue). **b**, simulated field profile at normal incidence. As is clear, the incident plane wave now very effectively couples to the MDWA waveguide mode. **c**, field profiles for a plane wave at an angle of incidence of 70°.

Figure 5.6a shows the simulated reflectivity as a function of angle for the air/coupling layer/MDWA system (red). As described above, the reflectivity $R = 0$ for normal incidence. Interestingly, the reflection remains low for a large range of angles; $R < 0.15$ for $\theta_i < 70°$. The reason for this low reflection over a broad angular range is that the field overlap between the dielectric metamaterial and the MDWA is unaffected by changing the angle of incidence; both field profiles experience the same lateral phase gradient $\exp(ik_x x)$ supplied by the incident plane wave. The increase in reflection is caused by the fact that for larger angles of incidence the condition of perfect destructive interference is no longer fulfilled as the optical path length $\beta_{DM}L$ is changed, as β_{DM} depends on the angle of incidence. For comparison, the reflectivity of the bare MDWA structure is also shown as a function

of angle of incidence (blue), the geometry with coupling layer shows a higher coupling efficiency for all angles of incidence.

Figure 5.6b shows the real part of $H_y(x,z)$ for a plane wave at normal incidence. As can be seen, strongly modulated field amplitudes are observed in the dielectric metamaterial, which facilitate the coupling into the MDWA waveguide mode. The waveguide mode is weakly attenuated with propagation along z, due to the small imaginary part in ε_m. Figure 5.6c shows the field profile for a plane wave incident at 70°. Again coupling is enhanced (from 50% with no coupling layer to 85% with coupling layer), and the negative refraction of the phase fronts in the MDWA is clearly visible.

5.5 Conclusions

We have demonstrated a method to strongly enhance coupling between a plane wave and a planar multilayer metal-dielectric waveguide array using a dielectric metamaterial as a coupling layer. By optimizing the filling fraction, the relative displacement between dielectric metamaterial and MDWA, and the coupling layer thickness the incident plane wave was fully coupled into the waveguide mode. The strong coupling efficiency is observed for a broad range of angles; from 100% at normal incidence, it is as high as 85% at 70° angle of incidence. The concept of a dielectric metamaterial acting as a coupling layer enables efficient light coupling in negative index metamaterials, and can be applied generally to any geometry with a spatial field profile mismatch between the incident radiation and the metamaterial.

5.6 Appendix: expanding plane waves and waveguide modes

Here we describe the modal method used to numerically calculate the transmission and reflection from an interface between a homogeneous and a stratified medium, or between two stratified media. As in the main text of this chapter, we write the magnetic field as an expansion of its eigenmodes:

$$\mathbf{H}^{(j)}(x,z) = \sum_{n=0}^{\infty} a_n e^{i\beta_{n,j}z} |\psi_n^{(j)}\rangle \tag{5.6}$$

Using Ampere's law we find for $\mathbf{E}$:

$$\mathbf{E}^{(j)}(x,z) = \frac{i}{\varepsilon_{(j)}(x)} \sum_{n=0}^{\infty} a_n \beta_{n,j} e^{i\beta_{n,j}z} |\psi_n^{(j)}\rangle \tag{5.7}$$

Using the continuity equations 5.1 from the main text we then find two equations:

$$\sum_{m=0}^{\infty} (a_m^+ + a_m^-) |\psi_{m,1}\rangle = \sum_{n=0}^{\infty} b_n^+ |\psi_{n,2}\rangle \tag{5.8a}$$

$$\frac{i}{\varepsilon_1(x)} \sum_{m=0}^{\infty} \beta_{m,1} (a_m^+ - a_m^-) |\psi_{n,1}\rangle = \frac{i}{\varepsilon_2(x)} \sum_{n=0}^{\infty} b_n^+ \beta_{n,2} |\psi_{n,2}\rangle \tag{5.8b}$$

Here a_n and b_n are the mode amplitudes in medium 1 and 2 respectively, and the sign corresponds to forward of backward propagating amplitudes. Making use of the orthonormality of Eq. 5.3 we can write this as equations for the amplitudes a_m:

$$a_m^+ + a_m^- = \sum_{n=0}^{\infty} b_n^+ \langle \psi_{m,1} | \frac{1}{\varepsilon_1(x)} | \psi_{n,2} \rangle \tag{5.9a}$$

$$a_m^+ - a_m^- = \sum_{n=0}^{\infty} b_n^+ \frac{\beta_{n,2}}{\beta_{m,1}} \langle \psi_{m,1} | \frac{1}{\varepsilon_2(x)} | \psi_{n,2} \rangle \tag{5.9b}$$

To solve this system numerically we truncate the infinite series at a certain integer l, typically around 50. This leads to the matrix equation:

$$\begin{pmatrix} -\mathbf{I}_{l\times l} & \mathbf{B^{(1)}}_{m,n} \\ \mathbf{I}_{l\times l} & \mathbf{B^{(2)}}_{m,n} \end{pmatrix} \begin{pmatrix} \mathbf{a}^- \\ \mathbf{b}^+ \end{pmatrix} = \begin{pmatrix} \mathbf{a}^+ \\ \mathbf{a}^+ \end{pmatrix} \tag{5.10}$$

where $\mathbf{I_{l\times l}}$ is the identity vector and the elements of the $\mathbf{B}$ matrices are given by:

$$B_{m,n}^{(1)} = \langle \psi_{m,1} | \frac{1}{\varepsilon_1(x)} | \psi_{n,2} \rangle \tag{5.11a}$$

$$B_{m,n}^{(2)} = \frac{\beta_{n,2}}{\beta_{m,1}} \langle \psi_{m,1} | \frac{1}{\varepsilon_2(x)} | \psi_{n,2} \rangle \tag{5.11b}$$

To solve this system for the reflected and transmitted mode amplitudes, the matrix is simply inverted:

$$\begin{pmatrix} \mathbf{a}^- \\ \mathbf{b}^+ \end{pmatrix} = \begin{pmatrix} -\mathbf{I}_{l\times l} & \mathbf{B^{(1)}}_{m,n} \\ \mathbf{I}_{l\times l} & \mathbf{B^{(2)}}_{m,n} \end{pmatrix}^{-1} \begin{pmatrix} \mathbf{a}^+ \\ \mathbf{a}^+ \end{pmatrix} \tag{5.12}$$

In the case of the interface between free space and a stratified medium, these equations simplify to:

$$B_{m,n}^{(1)} = \langle \psi_{m,1} | \psi_{n,2} \rangle \tag{5.13a}$$

$$B_{m,n}^{(2)} = \frac{\beta_{n,2}}{k_z^{(m)}} \langle \psi_{m,1} | \frac{1}{\varepsilon_2(x)} | \psi_{n,2} \rangle \tag{5.13b}$$

where $k_z^{(m)}$ is the component of the free space wave vector along the z-direction for the m^{th} diffracted order. The free space eigenmodes are given by:

$$|\psi_{m,1}\rangle = \exp(i(k_x + m\frac{2\pi}{a})x) \tag{5.14}$$

In this case the summation runs over negative indices as well, such that one sums from $m = -l/2$ to $m = l/2$ (for even l).

6

Applications and outlook

This Chapter provides an overview of ideas that originate from the research projects presented in the previous chapters of this thesis. The flat lens experimentally realized in Chapter 4 operated in the ultra-violet spectral range. Here we show that by changing the layer materials and thicknesses, a flat lens operating in the infrared may be realized, with an electrically tunable transmission. Furthermore, by studying the internal wave propagation through metal dielectric multilayer structures, as was done in Chapter 3, we show how we can use a hyperbolic metamaterial to design a special cavity geometry that very efficiently localizes light. Finally, we design a multilayer geometry that acts as a broadband angular filter, operating in the visible range. This structure filters incident light on angle of incidence and polarization, and might be applied to enhance the performance of light emitting diodes.

6.1 Flat lens operating in the near-infrared telecom band

6.1.1 Introduction

In Chapter 4, a metal/dielectric multilayer stack was designed that showed angle-independent negative refraction of energy, enabling a flat lens operating in the UV. Negative refraction is a general phenomenon that relies on having a significant amount of field localized in the metallic regions, with the permittivity of the metal being negative. As such, the phenomenon of negative refraction, and with appropriate design also flat lensing, can be obtained for any wavelength at which the metal permittivity is negative, provided that absorption losses are not too high.

To illustrate this, we design a flat lens operating in the near-infrared. This spectral range is important for telecommunication applications, as very long signal propagation lengths are attainable due to favorable material properties of both semiconductors (e.g. Si and Ge) and dielectrics (e.g. glass optical fibers), enabling integrated optical circuits [108]. Incorporating flat lenses in photonic integrated circuits may enable novel forms of on-chip optical signal processing.

To design an infrared flat lens, we first consider the noble metals Ag and Au. As shown in Fig. 6.1 they have an very large negative real part (a) of the permittivity in the IR, as well as a relatively large imaginary part (b). Because of the strongly negative real part of the permittivity, fields will not penetrate deep into the metallic layer, and therefore the interaction with the metal is small. Additionally, due to the large imaginary part, any field that is localized in the metallic layer will be strongly absorbed, preventing efficient light propagation in the lens.

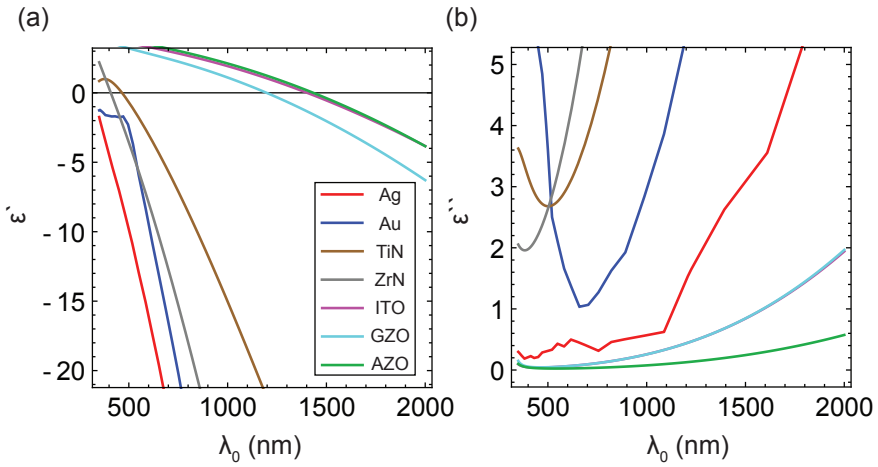

Figure 6.1: Real (**a**) and imaginary (**b**) part of the permittivity for different metallic materials. Optical constants for Ag and Au have been taken from [109]. The optical constants of the other materials are from [110].

Recently research has been directed at alternative materials with a moderate negative real part of the permittivity, in combination with a relatively small imaginary part [110, 111]. Figure 6.1 shows the permittivities of TiN, ZrN, and the transparent conductive oxides aluminum-doped zinc oxide (AZO), gallium-doped zinc oxide (GZO) and indium tin oxide (ITO) [112]. At the telecom band, near $\lambda_0 = 1550$ nm, AZO is the material with the lowest imaginary part and has a small negative real part: $\varepsilon_m = -0.689 + 0.269i$. We will combine this metallic material with a dielectric $\varepsilon_d = 2.5^2$, which is comparable to TiO_2, to design a flat lens.

6.1.2 IR Flat lens demonstration

To design a multilayer flat lens operating at $\lambda_0 = 1550$ nm, we calculate the isofrequency contour (IFC) $k_{Bl}(k_x)$ in the same way as was done in Chapter 4 for the UV spectral range. We perform this calculation for a range of layer thicknesses d_m and d_d, corresponding to the metal and dielectric layers respectively. In order to provide a comprehensible figure of merit, we calculate the deviation of $k_{Bl}(k_x)$ with the ideal $k_z(k_x) = \pi/a - \sqrt{k_0^2 - k_x^2}$, where a is the unit cell size. We determine the deviation by integrating the absolute difference between $k_{Bl}(k_x)$ and $k_z(k_x)$ between $k_x = 0$ and $k_x = k_0$, as given by Eq. 4.2.

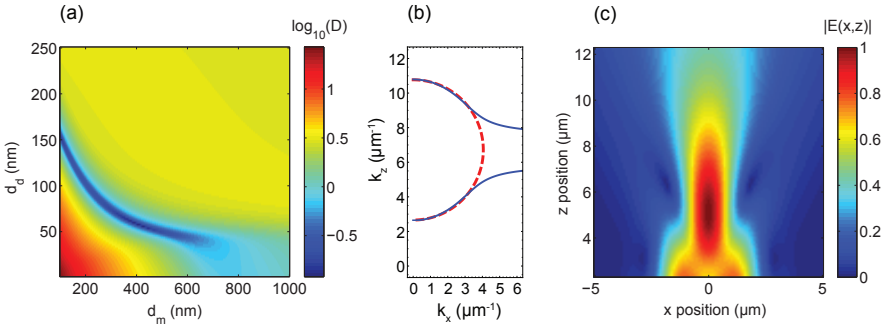

Figure 6.2: **a**, Deviation from ideal spherical IFC as a function of metal d_m and dielectric d_d layer thickness for a AZO/TiO_2 metamaterial at $\lambda_0 = 1550$ nm. **b**, IFC of the optimum geometry (blue) with: $d_m = 410$ nm and $d_d = 58$ nm. **c**, Result of a Green's tensor calculation showing the $|E(x,z)|$ spatial field amplitude calculated for a horizontal dipole placed above a slab of 5 unit cells of the optimum geometry. An elongated image is observed of the dipole.

Figure 6.2a shows the calculated deviation as a function of d_m and d_d. An optimum configuration is found with $d_m = 410$ nm and $d_d = 58$ nm, for which the deviation between ideal and calculated IFC is smallest. Figure 6.2b shows the IFC $k_{Bl}(k_x)$ (blue) corresponding to this optimum geometry, compared to the ideal spherical curve $k_z(k_x)$ (red). There are deviations between the IFC and the ideal case (red), which are especially pronounced at $k_x > 3\,\mu m^{-1}$, corresponding to an angle of approximately 48°. To demonstrate the imaging characteristics of a flat lens based on negative refraction in this multilayer structure, we consider a horizontal dipole source placed at $(x,z) = (0,-5)$ nm below a multilayer structure formed by 5 unit cells of this optimized geometry. Using Green's tensor calculations we can then determine the field profile on the other side of this multilayer stack. Fig. 6.2c shows the spatial field distribution above the surface at $z = 2.34\,\mu$m; as is clear, a focus is being formed above the infrared flat lens, corresponding to the image of the dipole source. The focus exhibits strong lateral confinement, with a FWHM of 1.7 μm.

6.1.3 Tunable flat lens

The use of a transparent conductive oxide (TCO) as a constituent of the flat lens design enables several new functionalities, as the permittivity of TCOs can be tuned locally by applying a positive electric bias [113]. An electric field across the TCO leads to a charge accumulation layer near the TCO/insulator interface. As the permittivity of AZO is described by a Drude model, a change in carrier density corresponds to a local change in permittivity.

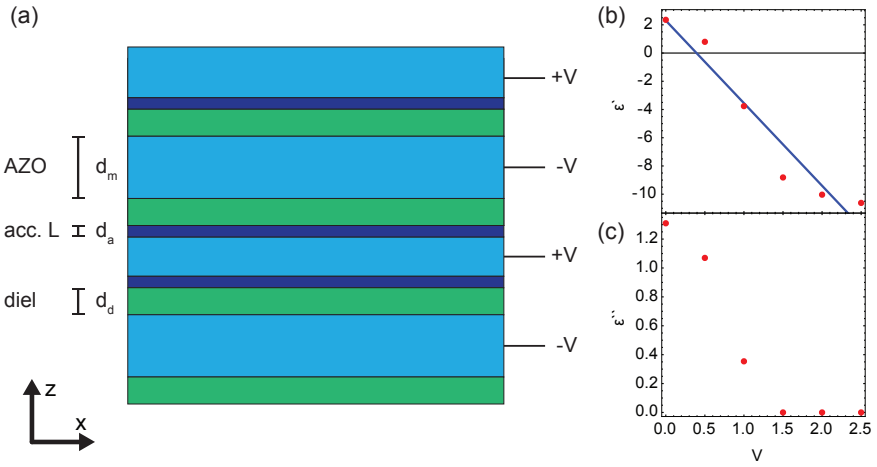

Figure 6.3: a, Tunable infrared flat lens design. Four unit cells of AZO/TiO_2 are considered, with an alternatingly positive and negative bias applied to the AZO, leading to an accumulation layer at the positively biased AZO interfaces. Blue corresponds to the biased AZO, where dark blue indicates the accumulation layers, and green layers are the TiO_2. **b**, Real and **c** imaginary part of the permittivity of ITO at $\lambda_0 = 1550$ nm, taken from [113]. The linear function fitted to the real part of the permittivity has a slope of $-5.9/V$.

Next, we investigate if the optical response of the flat lens can be changed dynamically by applying an electric bias. To this end, we imagine connecting subsequent AZO layers to either a positive or negative bias. Figure 6.3a shows the proposed multilayer design. For simplicity, in the following we will model the accumulation layer as a step-function, where the permittivity of the AZO within 5 nm of the interface is modulated by the potential. In reality, the charge accumulation depth profile will have an exponential shape. Note that no change in permittivity was experimentally observed for a negative bias [113]. Figure 6.3b,c shows the real and imaginary part of the permittivity of ITO at $\lambda_0 = 1550$ nm in the accumulation layer for varying potential, as experimentally observed by spectroscopic ellipsometry in [113]. A linear function fitted to the real part of the permittivity in Fig. 6.3b has a slope of $-5.9/V$. In the following we will apply this relation to the real part of the

experimental values of the permittivity of AZO, while keeping the imaginary part at the unperturbed value.

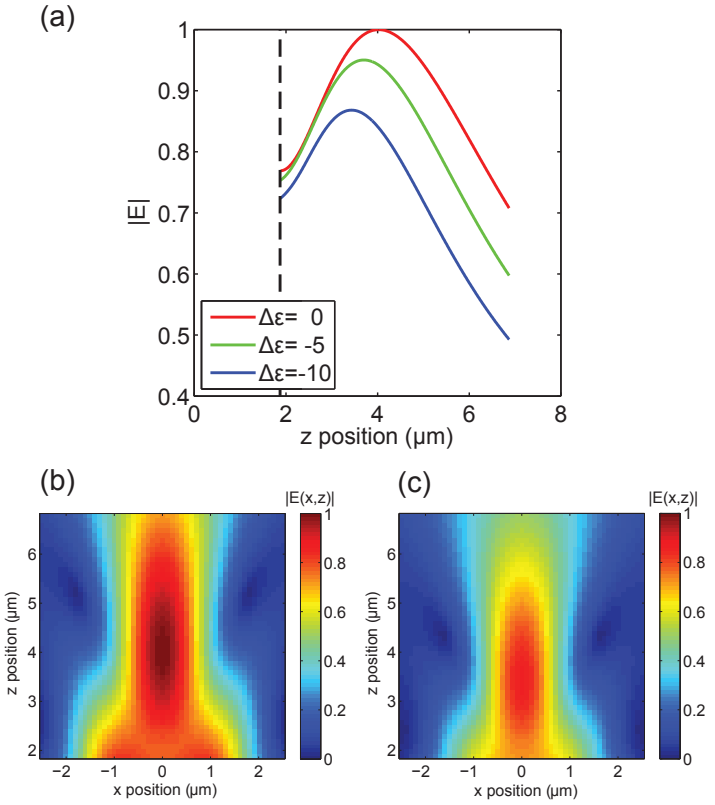

Figure 6.4: a, Absolute value of the electric field calculated along the optical axis above an AZO/TiO_2 flat lens operating in the infrared. The object is a horizontal dipole, placed 5 nm below the flat lens at $(x,z) = (0,-5)$ nm. The field amplitude is calculated above the lens surface (at $z = 1.872\,\mu$m, dashed line), for modulations of the permittivity: $\Delta\epsilon_m = 0$ (red), $\Delta\epsilon_m = -5$ (green) and $\Delta\epsilon_m = -10$ (blue). **b**, Image calculated when there is no potential on the flat lens. **c**, Image when the permittivity in the accumulation layer is modulated with $\Delta\epsilon_m = -10$.

Figure 6.4a shows the calculated electric field amplitude above the tunable flat lens, resulting from a horizontal dipole placed just below the multilayer structure at $(x,z) = (0,-5)$ nm. The electric field is calculated as a function of separation from the multilayer surface z, with $x = 0$. The lens consists of 4 unit cells corresponding to a surface at $z = 1.872\,\mu$m. The profile is calculated for three values of modulation of the permittivity in the accumulation layers: $\varepsilon_m = -0.689 + 0.269i$ (red), $\varepsilon_m = -5.689 + 0.269i$ (green) and $\varepsilon_m = -10.689 + 0.269i$ (blue) respectively, corresponding

to voltages between 0 and $2V$ (Fig. 6.3b). As can be seen, the peak in field amplitude at the focal point is modulated with 12%. The peak amplitude shifts 600 nm towards the flat lens interface. To illustrate the effect on the overall imaging performance of the flat lens, we show the image formed by the flat lens with no permittivity modulation in Fig. 6.4b, and with a permittivity modulation of $\Delta\epsilon_m = -10$ in Fig. 6.4c. The main effect visible is the reduction in amplitude, and the shift of the focal position towards the lens.

In the above, we have assumed strong permittivity changes of $\Delta\epsilon_m = -10$, based on the experimental data of [113]. Given such a strong modulation, the observed effect in imaging properties of the flat lens is relatively modest. We attribute this to the fact that the permittivity is only modulated close to the interface, while the light propagating through the flat lens interacts with the entire layer stack. A stronger interaction might be expected when light is coupled exclusively to surface waves [114]. Nonetheless, the design proposed here shows significant electrically controlled modulation in transmitted intensity, that could be used to modulate optical signals in a photonic integrated circuit operating in the infrared.

6.2 Hyperbolic metamaterial cavity

6.2.1 Introduction

As described in Chapter 4, propagation of light in hyperbolic metamaterials (HMMs) is described by permittivities of opposite sign for two orthogonal propagation directions. This extreme anisotropy leads to fascinating optical properties. Wave components with extremely high wavevectors, which are usually evanescent in vacuum, can propagate through a HMM. This is because the hyperboles in the dispersion relation (see Fig. 6.5a) only flatten off when k_z becomes comparable with π/a, where a is the unit cell size. Most hyperbolic metamaterial designs have an extremely small unit cell, which allows propagation of light with very high wavevectors.

Hyperbolic metamaterials can be used to fabricate nanoscale cavities [89, 115, 116], for which an anomalous scaling law is observed; the cavity resonance frequency is independent of cavity size. This phenomenon is exploited to fabricate deeply sub-wavelength cavities. So far, the details of internal wave propagation in these cavities have not been discussed to the best of our knowledge. Here, we predict a very fascinating relation between the internal wave propagation characteristics and the HMM cavity geometry.

The inspiration for this prediction comes from a very different research field; physical oceanography. It has been shown that internal gravity wave propagation in a uniformly stratified fluid is described by a hyperbolic dispersion relation, which implies that waves propagate in a direction with a fixed angle to the vertical [117, 118]. Interestingly, by appropriately designing a cavity with stratified water, it has been observed that following multiple internal reflections, these waves will eventu-

ally follow one specific path (an "attractor"), regardless of the original position and direction of the wave. Given how light propagates through a hyperbolic metamaterial, we expect a very similar phenomenon to occur for wave propagation through a hyperbolic optical metamaterial.

6.2.2 Internal wave propagation

In the following, we consider a HMM comprised of a stack of Ag and Ge thin films, as in [89], with the layers stacked in the z direction, and extended in the $x-y$ plane. For the Drude model given in that work, we find for a frequency of 220 THz ($\lambda_0 = 1363$ nm), $\epsilon_{\mathrm{Ag}} = -94.5 + 3.7i$, and we take $\epsilon_{\mathrm{Ge}} = 16$. Figure 6.5a shows the calculated IFC for this multilayer stack, for a unit cell of $a = 10$ nm, and a metal filling fraction of $\rho_{Ag} = 0.4$. The IFC is calculated for the center frequency at 220 THz (in green), and for a slightly lower frequency (red) and higher frequency (blue). The black circle plotted around the origin represents the IFC for a plane wave in vacuum at this frequency. If a dipole scatterer would be placed in the near field of the HMM medium, its wave vector components that are evanescent in air could couple into the HMM medium, and propagate inside the HMM. As an example, waves with $k_x = 50\,\mu m^{-1}$ are shown in Fig. 6.5a. The Poynting vector is indicated by the arrows, and as can be seen, light propagates in the metamaterial with an angle close to $\pm 45°$ or $\pm 135°$ with respect to the z-direction.

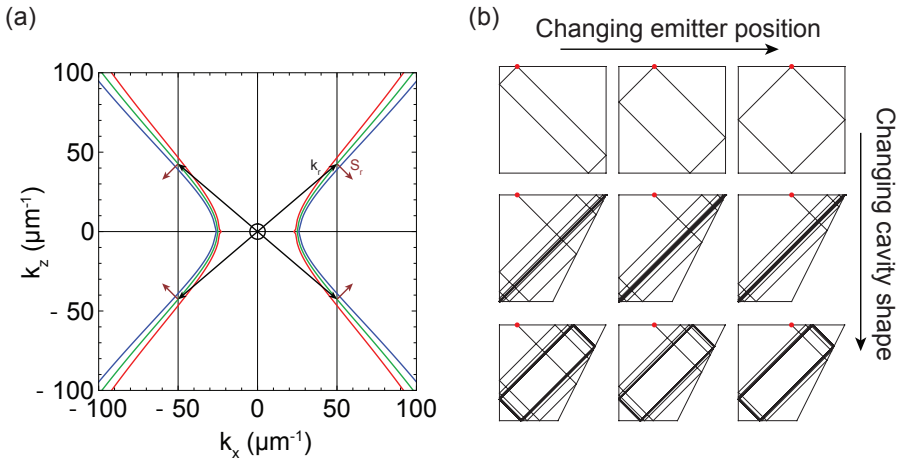

Figure 6.5: a, IFC calculated for a hyperbolic Ag/Ge metamaterial with a unit cell size $a = 10$ nm, $\rho_{Ag} = 0.4$ at 220 THz. The Poynting vector is oriented at $\pm 45°$ and $\pm 135°$. **b**, Cross sections are shown of hyperbolic metamaterial cavities in the $x-z$ plane. Ray tracing is performed for light emitters (red dots) at different positions, and for different cavity shapes.

If we now consider a cavity fabricated from this HMM, constructed by stacking

a limited number of unit cells in the z direction, and by limiting the extension of the layers in the $x-y$ plane, light with high spatial frequencies will be confined to the cavity due to total internal reflection. Inside the cavity, light only propagates at specific angles, as determined from the corresponding IFC. A cross-section in the $x-z$ plane of the HMM cavity is shown in Figure 6.5b. The top row shows a square cavity, with a dipole source (red dot) placed at different positions above the cavity. As radiation can only propagate under certain angles, the cavity mode will always be rectangular in shape, as is clear from the ray tracing shown in the top row. If the dipole source is placed at a different position, the cavity mode will have a different rectangular shape accordingly.

When we adapt the cavity shape, by displacing the bottom-right corner inward, as shown in the middle row, we see that the radiation will collapse onto the cavity diagonal. Interestingly, in this case, the path light collapses onto is independent of dipole position: all light in the cavity will eventually be guided onto the diagonal path, called an attractor [118]. The bottom row shows a different cavity shape, with a different size aspect ratio than the cavity in the middle row, for which light collapses onto a rectangular path.

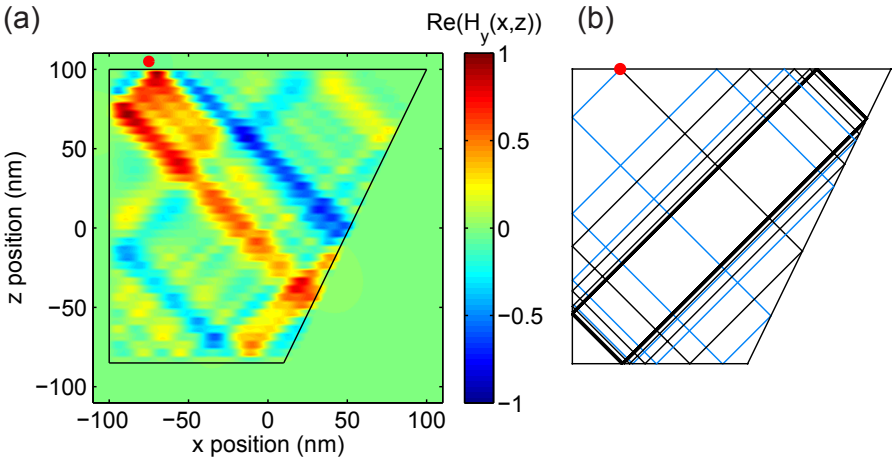

Figure 6.6: **a**, Simulated field distribution in a Ag/Ge hyperbolic metamaterial cavity with corners at: $(-100,-85)$, $(10,-85)$, $(100,100)$ and $(-100,100)$ (positions in nanometers). A horizontal dipole source is placed at $(-75,105)$. The $\mathrm{Re}(H_y(x,z))$ field component is shown. **b**, Ray tracing for this cavity geometry shows good agreement. Black (blue) lines; light emitted towards the right (left).

To visualize how waves propagate inside the HMM cavity, we perform a finite-difference time domain simulation of the propagation of light emitted by a horizontal dipole source placed at $(x,z) = (-75,105)$ nm, for a cavity with corners at $(-100,-85)$, $(10,-85)$, $(100,100)$ and $(-100,100)$ nm, and Ag and Ge layers with a permittivity as given above. Figure 6.6a shows the simulated field profile

$\mathrm{Re}(H_y(x,z))$ in the cavity. As can be seen, the field follows lines propagating at $\pm 45^\circ$ or $\pm 135^\circ$ to the normal, as expected. The individual Ag and Ge layers, stacked in the z direction, can also be resolved in the figure from the modulation in field amplitude. As is clear from the figure, the field is strongly absorbed, such that only the first few reflections in the cavity are resolved. However, the field clearly follows the expected path, based on ray tracing as shown in Fig. 6.6b. Interestingly, there seems to be no phase advance as light propagates along a ray, as seen from the almost constant value of the field component. We explain this effect by noting that the orientation of k and S is almost exactly perpendicular (see Fig. 6.5a), so as the energy flows in the direction of S, only a small phase advance should be observed.

The attenuation evident in Fig. 6.6a is caused by the absorption in the Ag layers, for which the imaginary part of the permittivity is very large. As noted in the previous section however, alternative materials such as transparent conductive oxides are available, which have much lower imaginary permittivity values in the IR. Furthermore, recent studies have shown that hexagonal boron nitride is a natural hyperbolic material in the mid-IR [119, 120], with a permittivity characterized by a negligible imaginary part. Such hyperbolic metamaterials would allow the waves to propagate much further in the cavity, leading to a stronger field enhancement along the attractor.

In the above, we have discussed the internal wave propagation inside a hyperbolic metamaterial. However, probing this internal field distribution in a three-dimensional cavity might prove difficult. A solution would be to use a hyperbolic metasurface, as was realized recently [86] in the form of a high quality Ag grating pattern. Such a hyperbolic metasurface provides an ideal platform to study the attractor in a hyperbolic metasurface cavity using the third dimension for optical experiments to probe the field pattern, using e.g. a near-field scanning optical microscope or cathodoluminescence microscopy. These techniques have a very high spatial resolution, enabling the observation of the attractor pattern in the cavity.

As can be seen in Fig. 6.6a, two rays leave the dipole, propagating at $\pm 135^\circ$ to the top surface normal, as expected. As was shown in [86], the direction of propagation in the hyperbolic metasurface is dependent on the polarization handedness, resulting in a plasmonic spin-Hall effect [121]. Similarly, the two rays visible in Fig. 6.6a should correspond to a different handedness. Reciprocally, this could entail that by exciting a rotating dipole in the near field of the hyperbolic metasurface cavity, all the energy is directly emitted in one direction determined by the polarization handedness, leading to a cavity mode which is non-degenerate. Therefore, this geometry allows us to very effectively harvest the evanescent components of a scattering element, and by tuning the exact cavity shape, the radiation profile can be steered. Accordingly, this platform can be used to route optical signals in a photonic integrated circuit.

6.3 Dielectric angular filter applied for light emission

6.3.1 Introduction

A well-known application of dielectric multilayers is in distributed Bragg reflectors (DBRs) [122], which act as mirrors for a specific wavelength range, depending on the material permittivities and layer thicknesses. Here, we discuss a special multilayer design that transmits TM-polarized light at the Brewster angle, while light with a different polarization and at different angles of incidence is reflected. Such an angular filter can be used to enhance the emission of light emitting diodes (LEDs) in a particular well defined angular range.

As a model system, we calculate the transmission coefficient of a multilayer structure consisting of 50 unit cells, where each unit cell has a defined size a_0, and the layers in the unit cell have: $\varepsilon_1 = 1$, $\varepsilon_2 = 2$, with $d_1\sqrt{\varepsilon_1} = d_2\sqrt{\varepsilon_2}$ and $d_1 + d_2 = a_0$. The transmission coefficient is calculated for TM polarized light as a function of wavelength and angle of incidence. Figure 6.7 shows the transmission coefficient $|t(\lambda_0, \theta_i)|$. We calculate the transmission coefficient for six different values of a_0, between 200 nm and 450 nm (a-f). Two observations are evident from the figure; first, there is a band of wavelength for which the multilayer stack shows high reflectance at normal incidence, and this band shifts to longer wavelength for larger values of a_0. Second, at the Brewster angle $\theta_{Br} = \tan^{-1}(\sqrt{\frac{\varepsilon_2}{\varepsilon_1}}) = 54.7°$ (dashed white line), the transmission $|t| = 1$ for all wavelengths.

By creating a supercell structure, where multilayer stacks with a different unit cell size a_0 are combined, an angular filter may be achieved operating for a broad band of wavelengths [123]. For such a geometry all wavelengths are reflected for all angles of incidence, except for TM polarized light at the Brewster angle. As an example, we consider a multilayer stack formed by 6 supercells, where each supercell consists of 8 unit cells. The unit cell size in supercell i is given as $a_i = a_0 r_0^{(i-1)}$, with rate $r_0 = 1.2$ and starting unit cell size $a_0 = 200$ nm for $i = 1-6$. In this case, the unit cell size a_i is gradually adjusted between $a_1 = 200$ nm for the bottom supercell and $a_6 = 500$ nm for the top supercell. As before, the unit cell parameters are given by: $\varepsilon_1 = 1$, $\varepsilon_2 = 2$, with $d_1\sqrt{\varepsilon_1} = d_2\sqrt{\varepsilon_2}$ and $d_1 + d_2 = a_0$. Because the multilayer structure now consists of reflectors designed to reflect different wavelengths, a broadband angular filter is realized.

Figure 6.8a shows the calculated transmission for TM-polarization as a function of wavelength and angle of incidence. As is clear, only light around the Brewster angle ($\theta = 54.7 \pm 10°$) is transmitted through the structure. This band can be made narrower by using more supercells, and by changing the rate r_0 to a value closer to 1. Interestingly, light that is TE-polarized (Fig. 6.8b) is reflected for all wavelengths and all angles of incidence. This principle was experimentally demonstrated [123] for a SiO_2/Ta_2O_5 multilayer structure. We now repeat the calculations for the more realistic parameters $\varepsilon_1 = 1.5^2$ and $\varepsilon_1 = 2.5^2$, to show that this idea may be applied using different materials. Figure 6.8(c-d) shows the calculated transmission for TM and TE polarized light respectively, for $r_0 = 1.15$, $a_0 = 120$ nm, and a multi-

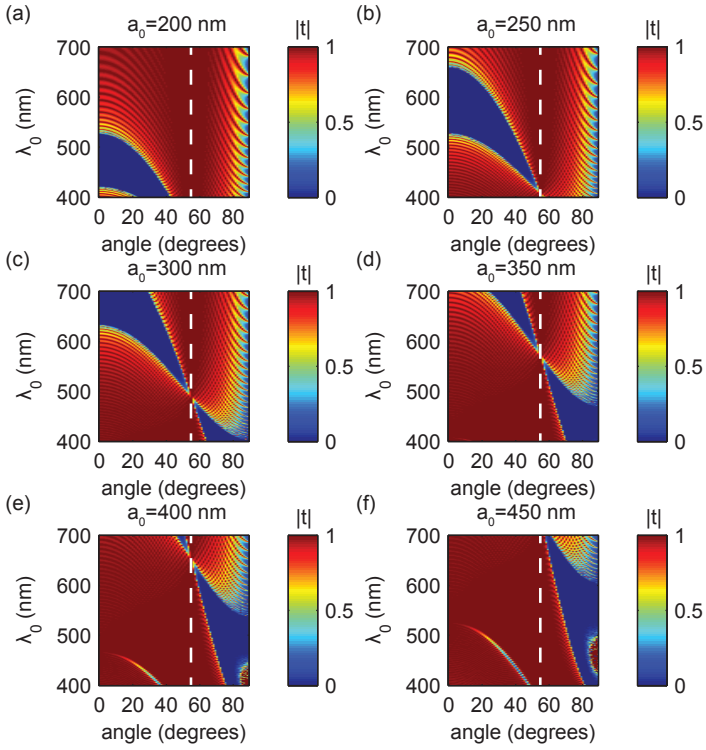

Figure 6.7: a-f, transmission coefficient as a function of wavelength and angle of incidence for different periodic unit cell size a_0. The transmission is calculated for TM-polarized light incident from air on a stack of 50 unit cells with $\varepsilon_1 = 1$, $\varepsilon_2 = 2$, $d_1\sqrt{\varepsilon_1} = d_2\sqrt{\varepsilon_2}$ and $d_1 + d_2 = a_0$. The Brewster angle is indicated by the vertical dashed line.

layer structure consisting of 8 supercells with 5 unit cells each. As can be seen, the stack again only transmits broadband light around the Brewster angle for TM-polarization.

6.3.2 Angular filter for light emission

One complication that arises when $\varepsilon_1 = 1.5^2$ is that the Brewster angle in such a multilayer system $\theta_{Br} = 59.0°$ cannot be reached for propagating waves in air, as the maximum angle of propagation in the ε_1 medium will then be limited by refraction at the air/multilayer interface: $\theta_{\max} = 41.8°$. Therefore, light propagating through such a stack would suffer total internal reflection, and light incident from outside the multilayer stack would also be reflected. One solution to this problem is to suspend the multilayer structure in a fluid which is index matched to ε_1, contained

in a square holder, as is sketched in Fig. 6.8e, and demonstrated in Ref. [123].

Such a solution is not very practical if we want to use the angular filters to control the directionality of the emission of light emitting diodes for instance. However, emission of light in a light emitting diode usually takes place in a high index medium [124]. Therefore, by directly covering the LED with an angular filter, as is sketched in Fig. 6.8f, light will be able to couple to the Brewster angle. To prevent total internal reflection at the top interface, we propose a triangular outcoupler, index matched to the low index dielectric layer with ε_1, which maintains the angle of propagation, and steers beams of light in opposite directions at well-determined angles.

An interesting aspect of the multilayer structures is that all light not at the Brewster angle, or not TM-polarized, is reflected back to the LED. Scattering elements could be incorporated in the LED to redistribute light, such that initially reflected light is scattered into the Brewster angle, enhancing outcoupling at a fixed angle. Alternatively, if a material is used with a very high radiative emission, more exotic schemes such as photon recycling [125] might lead to further improved angular emission efficiency.

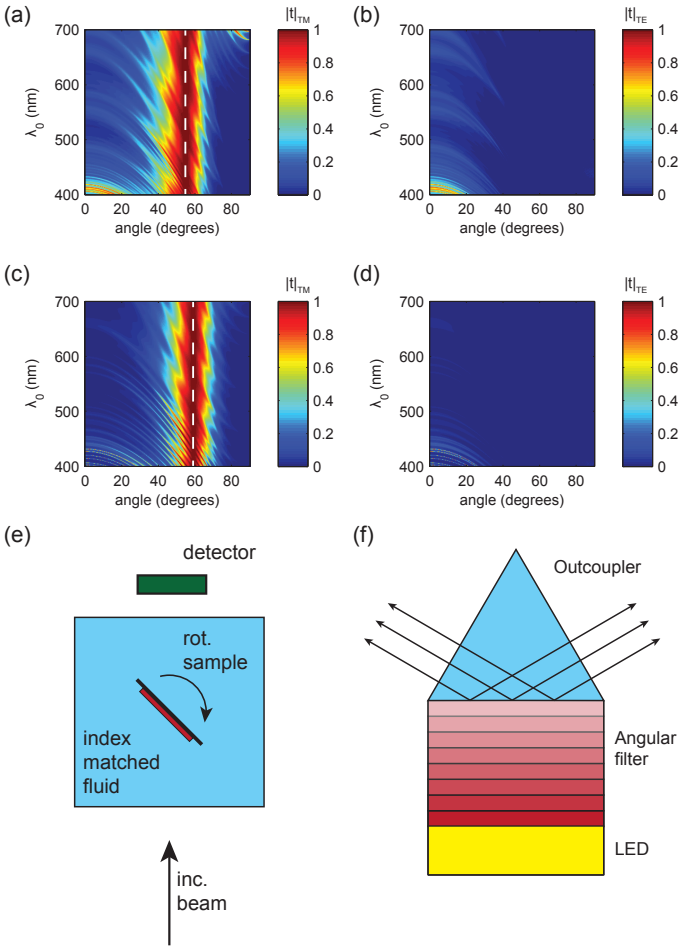

Figure 6.8: a,b, Transmission coefficient as a function of wavelength and angle of incidence for $\varepsilon_1 = 1$, $\varepsilon_2 = 2$. Shown is the transmission coefficient for TM (a) and TE (b) polarized light, for a supercell structure with $a_0 = 200$ nm and r_0=1.2. The Brewster angle is indicated by the vertical dashed line. **c,d**, transmission for a stack with $\varepsilon_1 = 1.5^2$ and $\varepsilon_1 = 2.5^2$, again for TM (c) and TE (d) polarization. Here, $a_0 = 120$ nm and $r_0 = 1.15$. **e**, Experimental geometry used in [123]; the multilayer stack is placed in an index matching fluid, and the sample is rotated with respect to the incident beam. **f**, Sketch of proposed geometry to control light emission using an integrated multilayer angular filter.

References

[1] W. Kock, *Metal-Lens Antenna,* Proc I.R.E. and Waves and Electrons **34**, 828 (1946).

[2] J. Brown, *Artificial dielectrics having refractive indices less than unity,* Proc of the IEE - Part IV **100**, 51 (1953).

[3] P. W. K. Rothemund, *Folding DNA to create nanoscale shapes and patterns,* Nature **440**, 297 (2006).

[4] A. Kuzyk, R. Schreiber, Z. Fan, G. Pardatscher, E.-M. Roller, A. Hogele, F. C. Simmel, A. O. Govorov, and T. Liedl, *DNA-based self-assembly of chiral plasmonic nanostructures with tailored optical response,* Nature **483**, 311 (2012), 10.1038/nature10889.

[5] V. G. Veselago, *The electrodynamics of substances with simultaneously negative values of epsilon and mu,* Sov. Phys. Usp. **10**, 509 (1968).

[6] J. Pendry, A. J. Holden, D. J. Robbins, and W. J. Stewart, *Magnetism from Conductors and Enhanced Nonlinear Phenomena,* IEEE Trans. Microw. Theory Tech. **47**, 2075 (1999).

[7] D. R. Smith, W. J. Padilla, D. C. Vier, S. C. Nemat-Nasser, and S. Schultz, *Composite Medium with Simultaneously Negative Permeability and Permittivity,* Phys. Rev. Lett. **84**, 4184 (2000).

[8] R. A. Shelby, D. R. Smith, and S. Schultz, *Experimental Verification of a Negative Index of Refraction,* Science **292**, 77 (2001).

[9] G. Dolling, C. Enkrich, M. Wegener, C. M. Soukoulis, and S. Linden, *Simultaneous negative phase and group velocity of light in a metamaterial,* Science **312**, 892 (2006).

[10] J. Valentine, S. Zhang, T. Zentgraf, E. Ulin-Avila, D. A. Genov, G. Bartal, and X. Zhang, *Three-dimensional optical metamaterial with a negative refractive index,* Nature **455**, 376 (2008).

[11] G. Dolling, M. Wegener, C. M. Soukoulis, and S. Linden, *Negative-index metamaterial at 780 nm wavelength,* Optics Letters **32**, 53 (2007).

[12] N. Liu, H. Guo, L. Fu, S. Kaiser, H. Schweizer, and H. Giessen, *Three-dimensional photonic metamaterials at optical frequencies,* Nat Mater **7**, 31 (2008).

[13] N. Yu, P. Genevet, M. A. Kats, F. Aieta, J.-P. Tetienne, F. Capasso, and Z. Gaburro, *Light Propagation with Phase Discontinuities: Generalized Laws of Reflection and Refraction,* Science **334**, 333 (2011).

[14] A. Silva, F. Monticone, G. Castaldi, V. Galdi, A. Alù, and N. Engheta, *Performing Mathematical Operations with Metamaterials,* Science **343**, 160 (2014).

[15] L. Huang, X. Chen, H. Mühlenbernd, H. Zhang, S. Chen, B. Bai, Q. Tan, G. Jin, K.-W. Cheah, C.-W. Qiu, J. Li, T. Zentgraf, and S. Zhang, *Three-dimensional optical holography using a plasmonic metasurface,* Nat Commun **4** (2013).

[16] W. L. Barnes, A. Dereux, and T. W. Ebbesen, *Surface plasmon subwavelength optics*, Nature **424**, 824 (2003).

[17] R. Zia, M. D. Selker, P. B. Catrysse, and M. L. Brongersma, *Geometries and materials for subwavelength surface plasmon modes,* Journal of the Optical Society of America A **21**, 2442 (2004).

[18] P. Tournois and V. Laude, *Negative group velocities in metal-film optical waveguides*, Opt. Commun. **137**, 41 (1997).

[19] H. J. Lezec, J. A. Dionne, and H. A. Atwater, *Negative Refraction at Visible Frequencies*, Science **316**, 430 (2007).

[20] J. A. Dionne, E. Verhagen, A. Polman, and H. A. Atwater, *Are negative index materials achievable with surface plasmon waveguides? A case study of three plasmonic geometries*, Opt. Express **16**, 19001 (2008).

[21] E. Verhagen, R. de Waele, L. Kuipers, and A. Polman, *Three-Dimensional Negative Index of Refraction at Optical Frequencies by Coupling Plasmonic Waveguides*, Phys. Rev. Lett. **105**, 223901 (2010).

[22] S. P. Burgos, R. de Waele, A. Polman, and H. A. Atwater, *A single-layer wide-angle negative-index metamaterial at visible frequencies*, Nat Mater **9**, 407 (2010).

[23] C. L. Cortes, W. Newman, S. Molesky, and Z. Jacob, *Quantum nanophotonics using hyperbolic metamaterials*, Journal of Optics **14**, 063001 (2012).

[24] A. Poddubny, I. Iorsh, P. Belov, and Y. Kivshar, *Hyperbolic metamaterials*, Nature Photonics **7**, 948 (2013).

[25] Z. Jacob, J. Y. Kim, G. V. Naik, A. Boltasseva, E. E. Narimanov, and V. M. Shalaev, *Engineering photonic density of states using metamaterials*, Applied Physics B **100**, 215 (2010).

[26] M. A. Noginov, H. Li, Y. A. Barnakov, D. Dryden, G. Nataraj, G. Zhu, C. E. Bonner, M. Mayy, Z. Jacob, and E. E. Narimanov, *Controlling spontaneous emission with metamaterials*, Optics Letters **35**, 1863 (2010).

[27] A. Salandrino and N. Engheta, *Far-field subdiffraction optical microscopy using metamaterial crystals: Theory and simulations*, Physical Review B **74**, 075103 (2006).

[28] Z. Liu, H. Lee, Y. Xiong, C. Sun, and X. Zhang, *Far-Field Optical Hyperlens Magnifying Sub-Diffraction-Limited Objects*, Science **315**, 1686 (2007).

[29] P. S. J. Russell, T. A. Birks, and F. D. Lloyd-Lucas, *Photonic Bloch Waves and Photonic Band Gaps*, Confined Electrons and Photons, Springer US, 1995.

[30] K. Sakoda and W. T. Rhodes, *Optical Properties of Photonic Crystals*, Springer, 2003.

[31] R. Ziolkowski, *Propagation in and scattering from a matched metamaterial having a zero index of refraction*, Physical Review E **70** (2004).

[32] M. Silveirinha and N. Engheta, *Tunneling of Electromagnetic Energy through Subwavelength Channels and Bends using ε-Near-Zero Materials*, Physical Review Letters **97** (2006).

[33] A. Alù, M. Silveirinha, A. Salandrino, and N. Engheta, *Epsilon-near-zero metamaterials and electromagnetic sources: Tailoring the radiation phase pattern*, Physical Review B **75** (2007).

[34] A. Alù and N. Engheta, *Light squeezing through arbitrarily shaped plasmonic channels and sharp bends*, Physical Review B **78** (2008).

[35] B. Edwards, A. Alù, M. Young, M. Silveirinha, and N. Engheta, *Experimental Verification of Epsilon-Near-Zero Metamaterial Coupling and Energy Squeezing Using a Microwave Waveguide*, Physical Review Letters **100** (2008).

[36] B. Edwards, A. Alù, M. G. Silveirinha, and N. Engheta, *Reflectionless sharp bends and*

corners in waveguides using epsilon-near-zero effects, Journal of Applied Physics **105** (2009).

[37] D. C. Adams, S. Inampudi, T. Ribaudo, D. Slocum, S. Vangala, N. A. Kuhta, W. D. Goodhue, V. A. Podolskiy, and D. Wasserman, *Funneling Light through a Subwavelength Aperture with Epsilon-Near-Zero Materials*, Physical Review Letters **107** (2011).

[38] C. Rizza, A. Di Falco, and A. Ciattoni, *Gain assisted nanocomposite multilayers with near zero permittivity modulus at visible frequencies*, Applied Physics Letters **99** (2011).

[39] S. Vassant, A. Archambault, F. Marquier, F. Pardo, U. Gennser, A. Cavanna, J. L. Pelouard, and J. J. Greffet, *Epsilon-Near-Zero Mode for Active Optoelectronic Devices*, Physical Review Letters **109** (2012).

[40] R. Liu, Q. Cheng, T. Hand, J. Mock, T. Cui, S. Cummer, and D. Smith, *Experimental Demonstration of Electromagnetic Tunneling Through an Epsilon-Near-Zero Metamaterial at Microwave Frequencies*, Physical Review Letters **100** (2008).

[41] E. J. R. Vesseur, T. Coenen, H. Caglayan, N. Engheta, and A. Polman, *Experimental Verification of n=0 Structures for Visible Light*, Physical Review Letters **110** (2013).

[42] J. Luo, P. Xu, and L. Gao, *Directive emission based on one-dimensional metal heterostructures*, J. Opt. Soc. Am. B **29** (2012).

[43] A. Alù and N. Engheta, *Boosting Molecular Fluorescence with a Plasmonic Nanolauncher*, Physical Review Letters **103** (2009).

[44] G. V. Naik, J. Liu, A. V. Kildishev, V. M. Shalaev, and A. Boltasseva, *Demonstration of Al:ZnO as a plasmonic component for near-infrared metamaterials*, Proc Natl Acad Sci U S A **109**, 8834 (2012).

[45] H. N. Krishnamoorthy, Z. Jacob, E. Narimanov, I. Kretzschmar, and V. M. Menon, *Topological transitions in metamaterials*, Science **336**, 205 (2012).

[46] Z. Jacob and V. M. Shalaev, *Plasmonics goes quantum*, Science **334**, 463 (2011).

[47] D. R. Smith and S. Schultz, *Determination of effective permittivity and permeability of metamaterials from reflection and transmission coefficients*, Physical Review B **65** (2002).

[48] V. G. Veselago and E. E. Narimanov, *The left hand of brightness: past, present and future of negative index materials*, Nat. Mater. **5**, 759 (2006).

[49] J. B. Pendry, *Negative Refraction Makes a Perfect Lens*, Phys. Rev. Lett. **85**, 3966 (2000).

[50] D. R. Smith, D. Schurig, M. Rosenbluth, S. Schultz, S. A. Ramakrishna, and J. B. Pendry, *Limitations on subdiffraction imaging with a negative refractive index slab*, Appl. Phys. Lett. **82**, 1506 (2003).

[51] P. Kolinko and D. R. Smith, *Numerical study of electromagnetic waves interacting with negative index materials*, Opt. Express **11**, 640 (2003).

[52] A. Grbic and G. V. Eleftheriades, *Overcoming the Diffraction Limit with a Planar Left-Handed Transmission-Line Lens*, Phys. Rev. Lett. **92**, 117403 (2004).

[53] C. M. Soukoulis and M. Wegener, *Past achievements and future challenges in the development of three-dimensional photonic metamaterials*, Nat. Photonics **5**, 523 (2011).

[54] C. García-Meca, J. Hurtado, J. Martí, A. Martínez, W. Dickson, and A. V. Zayats, *Low-Loss Multilayered Metamaterial Exhibiting a Negative Index of Refraction at Visible Wavelengths*, Phys. Rev. Lett. **106**, 067402 (2011).

[55] B. Kante, K. O'Brien, A. Niv, X. Yin, and X. Zhang, *Proposed isotropic negative index in three-dimensional optical metamaterials*, Phys. Rev. B **85**, 041103 (2012).

[56] G. Shvets, *Photonic approach to making a material with a negative index of refraction*,

Phys. Rev. B **67**, 035109 (2003).

[57] T. Xu, A. Agrawal, M. Abashin, K. J. Chau, and H. J. Lezec, *All-angle negative refraction and active flat lensing of ultraviolet light*, Nature **497**, 470 (2013).

[58] B. Lombardet, L. A. Dunbar, R. Ferrini, and R. Houdré, *Fourier analysis of Bloch wave propagation in photonic crystals*, J. Opt. Soc. Am. B **22**, 1179 (2005).

[59] M. Ghebrebrhan, M. Ibanescu, S. G. Johnson, M. Soljacic, and J. D. Joannopoulous, *Distinguishing zero-group-velocity modes in photonic crystals*, Phys. Rev. A **76**, 063810 (2007).

[60] M. G. Silveirinha, *Broadband negative refraction with a crossed wire mesh*, Phys. Rev. B **79**, 153109 (2009).

[61] M. Notomi, *Theory of light propagation in strongly modulated photonic crystals: Refractionlike behavior in the vicinity of the photonic band gap*, Phys. Rev. B **62**, 10696 (2000).

[62] S. Foteinopoulou, E. N. Economou, and C. M. Soukoulis, *Refraction in Media with a Negative Refractive Index*, Phys. Rev. Lett. **90**, 107402 (2003).

[63] L. D. Landau, E. M. Lifshitz, and L. P. Pitaevskii, *Electrodynamics of Continuous Media*, volume 8, Butterworth Heinemann, 1960.

[64] Y. Liu, G. Bartal, and X. Zhang, *All-angle negative refraction and imaging in a bulk medium made of metallic nanowires in the visible region*, Opt. Express **16**, 15439 (2008).

[65] C. Luo, S. G. Johnson, J. D. Joannopoulos, and J. B. Pendry, *All-angle negative refraction without negative effective index*, Phys. Rev. B **65**, 201104 (2002).

[66] R. Wangberg, J. Elser, E. E. Narimanov, and V. A. Podolskiy, *Nonmagnetic nanocomposites for optical and infrared negative-refractive-index media*, J. Opt. Soc. Am. B **23**, 498 (2006).

[67] J. Yao, Z. Liu, Y. Liu, Y. Wang, C. Sun, G. Bartal, A. M. Stacy, and X. Zhang, *Optical Negative Refraction in Bulk Metamaterials of Nanowires*, Science **321**, 930 (2008).

[68] V. M. Shalaev, *Optical negative-index metamaterials*, Nat Photon **1**, 41 (2007).

[69] P. Moitra, Y. Yang, Z. Anderson, I. I. Kravchenko, D. P. Briggs, and J. Valentine, *Realization of an all-dielectric zero-index optical metamaterial*, Nature Photonics **7**, 791 (2013).

[70] P. Belov, *Backward waves and negative refraction in uniaxial dielectrics with negative dielectric permittivity along the anisotropy axis*, Microwave and Optical Technology Letters **37**, 259 (2003).

[71] J. Schilling, *Uniaxial metallo-dielectric metamaterials with scalar positive permeability*, Physical Review E **74** (2006).

[72] D. R. Smith, P. Kolinko, and D. Schurig, *Negative refraction in indefinite media*, J. Opt. Soc. Am. B **21**, 1032 (2004).

[73] A. J. Hoffman, L. Alekseyev, S. S. Howard, K. J. Franz, D. Wasserman, V. A. Podolskiy, E. E. Narimanov, D. L. Sivco, and C. Gmachl, *Negative refraction in semiconductor metamaterials*, Nat Mater **6**, 946 (2007).

[74] C. Argyropoulos, N. M. Estakhri, F. Monticone, and A. Alù, *Negative refraction, gain and nonlinear effects in hyperbolic metamaterials*, Opt Express **21**, 15037 (2013).

[75] D. R. Smith, D. Schurig, J. J. Mock, P. Kolinko, and P. Rye, *Partial focusing of radiation by a slab of indefinite media*, Applied Physics Letters **84**, 2244 (2004).

[76] H. Liu, Q. Lv, H. Luo, S. Wen, W. Shu, and D. Fan, *Focusing of vectorial fields by a slab of indefinite media*, Journal of Optics A: Pure and Applied Optics **11**, 105103 (2009).

[77] H. Shin and S. Fan, *All-angle negative refraction and evanescent wave amplification*

using one-dimensional metallodielectric photonic crystals, Applied Physics Letters **89**, 151102 (2006).

[78] M. G. Silveirinha and A. B. Yakovlev, *Negative refraction by a uniaxial wire medium with suppressed spatial dispersion*, Physical Review B **81** (2010).

[79] M. G. Silveirinha, *Metamaterial homogenization approach with application to the characterization of microstructured composites with negative parameters*, Physical Review B **75** (2007).

[80] M. G. Silveirinha, *Poynting vector, heating rate, and stored energy in structured materials: A first-principles derivation*, Physical Review B **80** (2009).

[81] J. T. Costa, M. G. Silveirinha, and A. Alú, *Poynting vector in negative-index metamaterials*, Physical Review B **83** (2011).

[82] R. Maas, E. Verhagen, J. Parsons, and A. Polman, *Negative Refractive Index and Higher-Order Harmonics in Layered Metallodielectric Optical Metamaterials*, ACS Photonics **1**, 670 (2014).

[83] J. Hyuk Park, P. Nagpal, S.-H. Oh, and D. J. Norris, *Improved dielectric functions in metallic films obtained via template stripping*, Applied Physics Letters **100**, 081105 (2012).

[84] V. J. Logeeswaran, N. P. Kobayashi, M. S. Islam, W. Wu, P. Chaturvedi, N. X. Fang, S. Y. Wang, and R. S. Williams, *Ultrasmooth Silver Thin Films Deposited with a Germanium Nucleation Layer*, Nano Letters **9**, 178 (2009).

[85] W. Chen, M. D. Thoreson, S. Ishii, A. V. Kildishev, and V. M. Shalaev, *Ultra-thin ultra-smooth and low-loss silver films on a germanium wetting layer*, Optics Express **18**, 5124 (2010).

[86] A. A. High, R. C. Devlin, A. Dibos, M. Polking, D. S. Wild, J. Perczel, N. P. de Leon, M. D. Lukin, and H. Park, *Visible-frequency hyperbolic metasurface*, Nature **522**, 192 (2015).

[87] T. Tumkur, G. Zhu, P. Black, Y. A. Barnakov, C. E. Bonner, and M. A. Noginov, *Control of spontaneous emission in a volume of functionalized hyperbolic metamaterial*, Applied Physics Letters **99**, 151115 (2011).

[88] J. Kim, V. P. Drachev, Z. Jacob, G. V. Naik, A. Boltasseva, E. E. Narimanov, and V. M. Shalaev, *Improving the radiative decay rate for dye molecules with hyperbolic metamaterials*, Optics Express **20**, 8100 (2012).

[89] X. Yang, J. Yao, J. Rho, X. Yin, and X. Zhang, *Experimental realization of three-dimensional indefinite cavities at the nanoscale with anomalous scaling laws*, Nat Photon **6**, 450 (2012).

[90] R. Maas, J. Parsons, N. Engheta, and A. Polman, *Experimental realization of an epsilon-near-zero metamaterial at visible wavelengths*, Nature Photonics **7**, 907 (2013).

[91] X. Fan, G. P. Wang, J. C. W. Lee, and C. T. Chan, *All-Angle Broadband Negative Refraction of Metal Waveguide Arrays in the Visible Range: Theoretical Analysis and Numerical Demonstration*, Physical Review Letters **97**, 073901 (2006).

[92] P. Spinelli, M. A. Verschuuren, and A. Polman, *Broadband omnidirectional antireflection coating based on subwavelength surface Mie resonators*, Nat Commun **3**, 692 (2012).

[93] S. A. Mann, R. R. Grote, R. M. Osgood, and J. A. Schuller, *Dielectric particle and void resonators for thin film solar cell textures*, Optics Express **19**, 25729 (2011).

[94] J. van de Groep, P. Spinelli, and A. Polman, *Single-Step Soft-Imprinted Large-Area Nanopatterned Antireflection Coating*, Nano Letters **15**, 4223 (2015).

[95] M. G. Moharam and T. K. Gaylord, *Rigorous coupled-wave analysis of planar-grating diffraction*, Journal of the Optical Society of America **71**, 811 (1981).

[96] P. Sheng, R. S. Stepleman, and P. N. Sanda, *Exact eigenfunctions for square-wave gratings: Application to diffraction and surface-plasmon calculations*, Physical Review B **26**, 2907 (1982).

[97] M. G. Moharam, T. K. Gaylord, E. B. Grann, and D. A. Pommet, *Formulation for stable and efficient implementation of the rigorous coupled-wave analysis of binary gratings*, Journal of the Optical Society of America A **12**, 1068 (1995).

[98] P. Lalanne and G. M. Morris, *Highly improved convergence of the coupled-wave method for TM polarization*, Journal of the Optical Society of America A **13**, 779 (1996).

[99] B. Sturman, E. Podivilov, and M. Gorkunov, *Eigenmodes for metal-dielectric light-transmitting nanostructures*, Physical Review B **76**, 125104 (2007).

[100] B. Sturman, E. Podivilov, and M. Gorkunov, *Theory of extraordinary light transmission through arrays of subwavelength slits*, Physical Review B **77**, 075106 (2008).

[101] T. W. Ebbesen, H. J. Lezec, H. F. Ghaemi, T. Thio, and P. A. Wolff, *Extraordinary optical transmission through sub-wavelength hole arrays*, Nature **391**, 667 (1998).

[102] J. A. Porto, F. J. GarcÃŋa-Vidal, and J. B. Pendry, *Transmission Resonances on Metallic Gratings with Very Narrow Slits*, Physical Review Letters **83**, 2845 (1999).

[103] J. D. Jackson and R. F. Fox, *Classical Electrodynamics, 3rd ed*, American Journal of Physics **67**, 841 (1999).

[104] S. E. Kocabaş, G. Veronis, D. A. B. Miller, and S. Fan, *Modal analysis and coupling in metal-insulator-metal waveguides*, Physical Review B **79**, 035120 (2009).

[105] A. Zettl, *Sturm-liouville theory*, American Mathematical Soc., 2010.

[106] M. Foresti, L. Menez, and A. V. Tishchenko, *Modal method in deep metal-dielectric gratings: the decisive role of hidden modes*, Journal of the Optical Society of America A **23**, 2501 (2006).

[107] K. B. Dossou, L. C. Botten, A. A. Asatryan, B. C. P. Sturmberg, M. A. Byrne, C. G. Poulton, R. C. McPhedran, and C. M. de Sterke, *Modal formulation for diffraction by absorbing photonic crystal slabs*, Journal of the Optical Society of America A **29**, 817 (2012).

[108] E. Ozbay, *Plasmonics: Merging Photonics and Electronics at Nanoscale Dimensions*, Science **311**, 189 (2006).

[109] P. B. Johnson and R. W. Christy, *Optical Constants of the Noble Metals*, Physical Review B **6**, 4370 (1972).

[110] G. V. Naik, V. M. Shalaev, and A. Boltasseva, *Alternative Plasmonic Materials: Beyond Gold and Silver*, Advanced Materials **25**, 3264 (2013).

[111] A. Boltasseva and H. A. Atwater, *Low-Loss Plasmonic Metamaterials*, Science **331**, 290 (2011).

[112] G. V. Naik, J. Kim, and A. Boltasseva, *Oxides and nitrides as alternative plasmonic materials in the optical range [Invited]*, Optical Materials Express **1**, 1090 (2011).

[113] E. Feigenbaum, K. Diest, and H. A. Atwater, *Unity-Order Index Change in Transparent Conducting Oxides at Visible Frequencies*, Nano Letters **10**, 2111 (2010).

[114] H. W. Lee, G. Papadakis, S. P. Burgos, K. Chander, A. Kriesch, R. Pala, U. Peschel, and H. A. Atwater, *Nanoscale Conducting Oxide PlasMOStor*, Nano Letters **14**, 6463 (2014).

[115] J. Yao, X. Yang, X. Yin, G. Bartal, and X. Zhang, *Three-dimensional nanometer-scale optical cavities of indefinite medium*, Proceedings of the National Academy of Sciences **108**, 11327 (2011).

[116] Y. He, S. He, J. Gao, and X. Yang, *Nanoscale metamaterial optical waveguides with ultrahigh refractive indices*, Journal of the Optical Society of America B **29**, 2559 (2012).

[117] L. R. M. Maas and F.-P. A. Lam, *Geometric focusing of internal waves*, Journal of Fluid Mechanics **300**, 1 (1995).

[118] L. R. M. Maas, D. Benielli, J. Sommeria, and F.-P. A. Lam, *Observation of an internal wave attractor in a confined, stably stratified fluid*, Nature **388**, 557 (1997).

[119] P. Li, M. Lewin, A. V. Kretinin, J. D. Caldwell, K. S. Novoselov, T. Taniguchi, K. Watanabe, F. Gaussmann, and T. Taubner, *Hyperbolic phonon-polaritons in boron nitride for near-field optical imaging*, arXiv preprint arXiv:1502.04093 (2015).

[120] S. Dai, Q. Ma, T. Andersen, A. S. McLeod, Z. Fei, M. K. Liu, M. Wagner, K. Watanabe, T. Taniguchi, M. Thiemens, F. Keilmann, P. Jarillo-Herrero, M. M. Fogler, and D. N. Basov, *Subdiffractional focusing and guiding of polaritonic rays in a natural hyperbolic material*, Nat Commun **6** (2015).

[121] P. V. Kapitanova, P. Ginzburg, F. J. Rodríguez-Fortuño, D. S. Filonov, P. M. Voroshilov, P. A. Belov, A. N. Poddubny, Y. S. Kivshar, G. A. Wurtz, and A. V. Zayats, *Photonic spin Hall effect in hyperbolic metamaterials for polarization-controlled routing of subwavelength modes*, Nat Commun **5** (2014).

[122] E. Spiller, *Soft X-ray optics*, SPIE Optical Engineering Press Bellingham, WA, 1994.

[123] Y. Shen, D. Ye, I. Celanovic, S. G. Johnson, J. D. Joannopoulos, and M. SoljaÄĎiÄĞ, *Optical Broadband Angular Selectivity*, Science **343**, 1499 (2014).

[124] S. Nakamura, T. Mukai, and M. Senoh, *Candela class high brightness InGaN/AlGaN double heterostructure blue light emitting diodes*, Applied Physics Letters **64**, 1687 (1994).

[125] F. Stern and J. M. Woodall, *Photon recycling in semiconductor lasers*, Journal of Applied Physics **45**, 3904 (1974).

Summary

Metamaterials are artificially constructed materials composed of sub-wavelength building blocks that are designed to interact with light in ways that cannot be achieved with natural materials. Over the last years, improvements in nanoscale fabrication and in metamaterial design have led to the development of metamaterials based on resonant nanostructures for the microwave and infrared spectral range. Material absorption limits the realization of resonant metamaterials in the visible spectral range. Furthermore, increasing fabrication complexity limits the assembly of three-dimensional resonant metamaterials in the visible and UV spectral range, as the typical feature size smaller than the wavelength is reduced.

This thesis presents a three-dimensional metamaterial design composed of a metal-dielectric thin-film multilayer stack. Light propagation in the optical metamaterial can be controlled by the layer geometry. The multilayer design benefits from the numerous fabrication techniques which are readily available to realize multilayer structures. Furthermore, because light is coupled to guided waves in the metamaterial, rather than confined to a localized resonance, absorption losses are reduced. Because of these advantages, the realization of a three-dimensional metamaterial operating in the visible and UV spectral range becomes possible.

This thesis describes the propagation characteristics in three-dimensional multilayer metamaterials, in a wide range of geometries. The effective optical constants of the metamaterials and the dispersion of light are studied, addressing wavelength, angle and polarization dependence.

In Chapter 2, we designed a multilayer metamaterial composed of Ag and SiN thin films. When TE-polarized light is incident on such a multilayer structure along the plane of the layers, the effective permittivity is determined by the Ag and SiN permittivities, the metal filling fraction and the unit cell size. By tuning these parameters we realized a metamaterial that has a vanishing permittivity at a wavelength of choice in the UV/visible range; $\lambda_0 = 351 - 633$ nm, depending on the exact layer geometry.

In Chapter 3 we investigate the effective optical properties of a metal-dielectric multilayer stack, where light propagation is determined by coupled surface plasmon polaritons. As was theoretically proposed, such metamaterials can have an

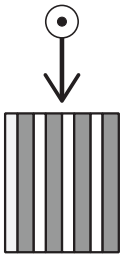

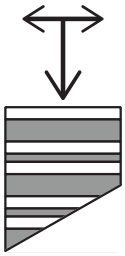

isotropic negative refractive index in the UV. When light propagates normal to the waveguides, the Bloch wave that travels through the metamaterial is composed of a series of harmonics. By analyzing the internal field profile, we find that most of the energy is carried by a higher-order harmonic. As a result, while energy refracts negatively in the metamaterial, the effective phase advance in this material is positive. Refraction experiments on a metamaterial prism sculpted from a deposited Ag/TiO_2 multilayer stack confirm this.

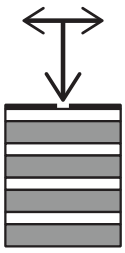

Exploiting these insights, in Chapter 4, we design a Ag/TiO_2 multilayer structure that shows negative refraction of energy for all angles of incidence, with an effective refractive index $n = -1$. Such a metal-dielectric multilayer stack acts as a flat lens. We fabricate the flat lens using physical vapor deposition. 100 nm slits milled through an opaque Cr masking layer using a focussed ion beam act as objects in the experiment. The image formed by the flat lens is resolved using confocal microscopy and a focus is observed 790 nm above the masking layer, corresponding to twice the flat lens thickness, as expected. The full-width half maximum of the focus is 350 nm, which agrees well with theoretical expectations. Near-field scanning optical microscopy directly shows the image above the lens surface.

In Chapter 3 and 4 we have mainly discussed how light propagates through the multilayer structure when it is incident normal to the layers. In Chapter 5, we theoretically investigate how light couples to a metal-dielectric waveguide array when light is incident from the side. The interface is then formed by a series of truncated waveguides, creating an inhomogeneous interface, which precludes the efficient incoupling of incident plane waves. To solve the boundary conditions, we expand the incident and reflected field into plane waves on the air side, and expand the field into waveguide eigenmodes in the metal and dielectric layers. We use this theory to design a dielectric coupling metamaterial, which covers this interface. The coupling layer can guide an incident plane wave with 100% efficiency into the negative index waveguide mode in the metal-dielectric waveguide array. Furthermore, we show how this coupling metamaterial also very effectively couples light into the waveguide array for a broad range of incident angles.

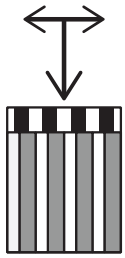

Finally, in Chapter 6 we present several potential applications based on new insights attained from the research presented in the previous chapters. We demonstrate a flat lens operating in the IR, which is a wavelength regime interesting for telecommunication applications. Furthermore, we show how the transmission of this design can be electrically modulated, allowing optoelectronic signal processing. A hyperbolic metamaterial, where light can propagate under fixed angles, is used to design a special cavity, which confines light to a fixed cavity path. Such a cavity enhances light-matter interactions, and can be used for routing optical signals in a photonic integrated circuit. Finally, we design a multilayer dielectric stack which acts as a angular filter, reflecting light of all wavelengths and angles of incidence, except TM-polarized light at the Brewster angle. We discuss how such a multilayer design can be used to enhance the angular emission of light emitting diodes, and describe how photon recycling might be used to create very efficient emitters.

Overall, this thesis provides insight in the propagation of light in metal-dielectric multilayer metamaterials. We demonstrate optical properties that do not exist in natural materials, such as a vanishing permittivity at a specific wavelength of choice, negative refraction of energy leading to a flat lens, and a structure with 100% coupling efficiency while not index matched to its surroundings. These properties are experimentally verified using phase-sensitive transmission measurements, angular refraction experiments and using confocal and near-field microscopy.

Samenvatting

Metamaterialen zijn kunstmatige materialen, samengesteld uit elementen die een typische lengteschaal hebben die kleiner is dan de golflengte van licht. Het doel van een metamateriaal is om door deze kunstmatige structuur optische interacties te verkrijgen die niet mogelijk zijn met natuurlijke materialen. Gedurende de laatste jaren hebben verbeteringen in nanoschaal fabricageprocessen en verbeteringen in het ontwerp van metamaterialen ertoe geleid dat metamaterialen gebaseerd op resonante nanostructuren zijn ontwikkeld voor microgolven en infraroodstraling. Absorptie in het materiaal beperkt de realisatie van metamaterialen die werken voor zichtbaar licht. Daarnaast wordt de fabricage van dergelijke metamaterialen steeds complexer, aangezien de typische lengteschaal van de elementen kleiner wordt samen met de golflengte van het licht waarvoor het metamateriaal bedoeld is.

Dit proefschrift presenteert een driedimensionaal metamateriaalontwerp gebaseerd op een multilaagstructuur met ultradunne metaal- en diëlectrische lagen. Lichtpropagatie in dit optische metamateriaal wordt bepaald door de geometrie van de lagen. Dit multilaagontwerp heeft als voordeel dat veel verschillende fabricagetechnieken reeds voorhanden zijn om dergelijke structuren te maken. Daarnaast zijn er minder absorptieverliezen in dit metamateriaal, omdat inkomend licht gekoppeld wordt aan oppervlaktegolven, in plaats van dat het gebonden wordt aan een lokale resonantie. Dankzij deze voordelen is het experimenteel realiseren van een dergelijk driedimensionaal metamateriaal dat werkt voor zichtbaar en ultraviolet licht mogelijk.

Dit proefschrift beschrijft de propagatiekarakteristieken in driedimensionale multilaagmetamaterialen voor verschillende geometrieën. De effectieve optische eigenschappen van deze metamaterialen en de dispersie van het licht worden bestudeerd, met aandacht voor de golflengte-, hoek-, en polarisatieafhankelijkheid.

In Hoofdstuk 2 ontwerpen wij een multilaag metamateriaal dat bestaat uit dunne lagen van zilver en siliciumnitride. Wanneer licht binnenvalt evenwijdig aan de lagen op deze multilaagstructuur, en het licht lineair gepolariseerd is met het elektrische veld georiënteerd langs de metaal/diëlectrische grensvlakken, dan wordt de effectieve permittiviteit van dit metamateriaal bepaald door

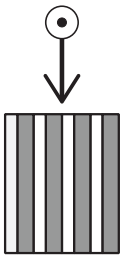

de permittiviteit van het zilver, het siliciumnitride, de fractie van het metaal, en de afmetingen van de eenheidscel. Door deze parameters te veranderen creëren we een metamateriaal dat een permittiviteit heeft die nul wordt voor een bepaalde golflengte in het ultraviolet en zichtbaar golflengtegebied: $\lambda_0 = 351 - 633$ nanometer, afhankelijk van de exacte samenstelling van het metamateriaal.

In Hoofdstuk 3 onderzoeken wij de effectieve optische eigenschappen van een metaal-diëlectrische multilaagstructuur, waarvoor lichtpropagatie bepaald wordt door gekoppelde oppervlakteplasmonpolaritonen. Zoals theoretisch is voorspeld vertoont een dergelijk metamateriaal een isotrope, driedimensionale negatieve brekingsindex in het ultraviolet. Wanneer licht zich voortplant in de richting die loodrecht staat op de golfgeleiders, dan beweegt het licht zich in de vorm van een Blochgolf, die bestaat uit een serie van harmonischen. Door de interne veldstructuur van het licht in het metamateriaal te bestuderen ontdekken wij dat de meeste energie in de Blochgolf gedragen wordt door een hogere-orde harmonische van de Blochgolf. Hierdoor zal het metamateriaal, dat negatieve breking van energie vertoont, toch een positieve fasetoename voor het licht veroorzaken. Dit theoretische resultaat bevestigen wij experimenteel door de brekingshoek van licht te meten dat afgebogen wordt door een prisma dat is gemaakt uit dit metamateriaal. Inderdaad blijkt de brekingshoek van het licht positief te zijn.

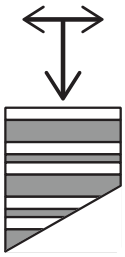

Gebruikmakend van deze verkregen inzichten ontwerpen wij in Hoofdstuk 4 een zilver titaniumdioxide multilaagstructuur die negatieve breking van energie vertoont voor alle hoeken van inval, met een effectieve brekingsindex $n = -1$. Een dergelijke metaal-diëlectrische multilaagstructuur vormt een vlakke lens. We construeren de vlakke lens met een vacuüm opdampkamer. 100 nanometer brede sleuven worden door een ondoorzichtige chroomlaag heen geëtst met behulp van een gefocusseerde ionenbundel, en deze sleuven worden gebruikt als objecten in het experiment. De afbeelding die gevormd wordt door de vlakke lens wordt bestudeerd met een confocale microscoop, en we zien een focus op 790 nanometer boven de chroomlaag. Deze afstand komt overeen met tweemaal de dikte van de vlakke lens, in overeenstemming met onze verwachtingen. De breedte van het focus is 350 nanometer, en dit komt overeen met theoretische voorspellingen. Met behulp van een nabije-veld microscoop nemen wij direct de afbeelding van een sleuf waar boven het lens oppervlak.

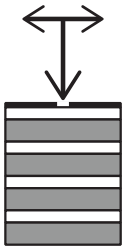

In Hoofdstuk 3 en Hoofdstuk 4 hebben we voornamelijk besproken hoe licht zich voortbeweegt door een multilaagstructuur wanneer de propagatierichting voornamelijk loodrecht op de lagen staat. In Hoofdstuk 5 onderzoeken we theoretisch hoe licht koppelt aan een metaal-diëlectrische multilaagstructuur wanneer het licht binnenkomt van de zijkant. Deze zijkant wordt gevormd door de beëindiging van de metalen en diëlectrische lagen, en daardoor is het gevormde oppervlak zeer inhomogeen. Hierdoor koppelt een binnenkomende vlakke golf slecht aan de golven die in de multilaagstructuur aanwezig zijn, en zal deze daardoor voornamelijk gereflecteerd worden. Om de randvoorwaarden op dit vlak op te lossen expanderen wij de inkomende en gereflecteerde golven in vlakke golven aan de kant van de lucht. In de multilaagstructuur expanderen we het veld

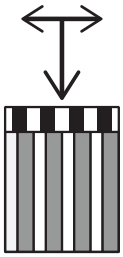

in orthonormale eigenmodes van de golfgeleiders. Met behulp van deze theorie ontwikkelen we een diëlectrisch koppelingsmetamateriaal dat op dit oppervlak wordt aangebracht. Deze koppelingslaag is in staat om een binnenkomende vlakke golf met 100% efficiëntie de multilaagstructuur binnen te geleiden. Daarnaast laten wij zien hoe deze koppelingslaag ook zeer efficiënt licht binnenlaat voor een groot bereik aan hoeken van inval.

Als laatste presenteren wij in Hoofdstuk 6 een aantal mogelijke toepassingen, gebaseerd op nieuwe inzichten die verkregen zijn tijdens het onderzoek dat gepresenteerd is in de voorgaande hoofdstukken. We demonstreren een vlakke lens die werkt voor infrarood licht, een golflengtegebied dat interessant is voor telecommunicatietoepassingen. Daarnaast laten we zien hoe de transmissie van deze vlakke lens elektrisch gemoduleerd kan worden, waardoor opto-elektronische signaalverwerking mogelijk is. Een hyperbolisch metamateriaal, waar licht zich voortplant onder bepaalde, vaste, hoeken, wordt gebruikt om een bijzondere trilholte te ontwikkelen, waarin licht opgesloten wordt, en een vast pad aflegt. Een dergelijke trilholte bevordert de interacties tussen licht en materiaal, en kan gebruikt worden voor het ruimtelijk sturen van optische signalen in een fotonisch geïntegreerd circuit. Als laatste ontwerpen we een diëlectrische multilaag, dat als een hoekfilter fungeert. Licht van alle golflengtes en alle hoeken van inval wordt gereflecteerd, behalve licht dat langs de Brewster hoek beweegt, en in het grensvlak gepolariseerd is. We bespreken hoe een dergelijk multilaagontwerp gebruikt kan worden om de hoekafhankelijke emissie van lichtuitstralende diodes te versterken, en door het recyclen van fotonen efficiënte lichtbronnen mogelijk maakt.

Samenvattend geeft dit proefschrift inzicht in hoe licht zich in metaal-diëlectrische multilaag metamaterialen voortbeweegt. We demonstreren optische eigenschappen die niet in natuurlijke materialen voorkomen, zoals een permittiviteit die naar nul gaat bij een golflengte naar keuze, negatieve breking van energie waarmee we een vlakke lens realiseren en een structuur waaraan licht met 100% efficiëntie kan koppelen, terwijl de structuur een andere brekingsindex dan de omgeving heeft. Deze eigenschappen zijn experimenteel bevestigd met behulp van fase-gevoelige transmissiemetingen, brekingshoekmetingen en confocale en nabije-veld microscopie.

List of publications

This thesis is based on the following publications:

- *Experimental realization of an epsilon-near-zero metamaterial at visible wavelengths*, R. Maas, J. Parsons, N. Engheta, and A. Polman, Nature Phot. **7**, 907 (2013). **(Chapter 2)**
- *Negative refractive index and higher-order harmonics in layered metallodielectric optical metamaterials*, R. Maas, E. Verhagen, J. Parsons, and A. Polman, ACS Phot. **1**, 670 (2014). **(Chapter 3)**
- *Planar metal/dielectric multilayer flat lens*, R. Maas, and A. Polman, in preparation. **(Chapter 4)**
- *Dielectric metamaterial anti-reflection coating for stratified media*, R. Maas*, S. Mann*, E. Garnett and A. Polman, in preparation. (*equal author contribution)**(Chapter 5)**

Other publications by the author:

- *Experimental realization of a polarization-independent ultraviolet/visible coaxial plasmonic metamaterial,* M. van de Haar, R. Maas, H. Schokker, and A. Polman, Nano Lett. **14**, 6356 (2014)

Acknowledgements

De afgelopen vier jaar van mijn promotie waren uitdagend, erg stimulerend en leuk. Dit omdat een onderzoek nooit alleen gedaan wordt, vandaar dit dankwoord. Tijdens mijn promotie heb ik de hulp en ondersteuning gehad van veel mensen om mij heen. Als eerste wil ik graag mijn promotor Albert Polman bedanken. Je bijzondere manier van college geven wekte in eerste instantie mijn interesse voor nanophotonics. Als begeleider wist je altijd de juiste vragen te stellen om mij te inspireren, en heb je een goede intuïtie in welke richting het onderzoek gestuurd moet worden. Deze eigenschappen, gecombineerd met een altijd positieve instelling zorgen ervoor dat er een goede sfeer in de groep is.

When I started my research at Amolf, my mentor was a young postdoc in our group, James Parsons. He had a background in nanophotonics, and possessed an extensive set of experimental skills, and thankfully also the patience to transfer this knowledge. At the FIB, a photo of an empty vacuum chamber still hangs from the computer, under which is written "Science is nothing without a sample, -JP", true words indeed. Apart from our good times in the lab, I will also always fondly remember throwing your couch out of the second floor window with Bas.

Mijn collega's in de groep Photonic Materials wil ik ook bedanken. De groepsbesprekingen leverden altijd interessante discussies op en we hebben vaak met een gezellige groep studiereizen ondernomen en conferenties bezocht. Ernst Jan, Piero, Toon, Claire, Marie Anne, Benjamin, Bonna, Lourens, Hinke, Julia en Bas wil ik daarvoor graag bedanken. Rutger Thijssen heeft tijdens zijn promotie een belangrijke rol gespeeld in de groep. Van elk onderdeel in het lab wist hij precies waar het oorspronkelijk voor bedoeld was, en waar je het allemaal nog meer voor zou kunnen gebruiken. Daarnaast kon hij je altijd helpen met het weer rechtbreien van een Labview spaghetti. Mark Knight has been the most recent addition to the group, and very active at that. Thank you for all your contributions and suggestions, as well as mighty fine pictures, and organizing the Amolf Puncheurs.

Part of the work presented here is due to collaborations with others. I would like to thank Nader Engheta for his endless stream of ideas, and for working together on a very interesting project. Een van de redenen waarom Amolf een hele mooie plek is om een promotieonderzoek te doen is de sterke ondersteuning. Hans Zeijlemaker,

Dimitry en Andries wil ik daar graag voor bedanken. Zij zorgen voor alle faciliteiten bij het Nanocenter, maar willen ook graag meedenken bij fabricageproblemen, en komen altijd even kijken als de Kameleon weer kuren heeft.

The Center for Nanophotonics is meer dan alleen een verzameling van verschillende onderzoeksgroepen. Dankzij de inzet van de groepsleiders is er een ware leerschool ontstaan, waarin nieuwe studenten worden opgeleid in het geven van duidelijke presentaties en waarin continue onderbroken worden tijdens je presentatie bijna een streven is geworden. De georganiseerde postersessies vormen een uitstekend platform om je onopgeloste problemen te etaleren, zolang je er maar een goed verhaal bij hebt. Ik wil Ewold in het bijzonder bedanken voor zijn hulp, in alle fasen van mijn onderzoek. Dankzij jouw eerdere werk kon ik beginnen aan een onderzoek waar veel gereedschappen en interessante aanknopingspunten al klaar lagen.

People who are critical, ask questions and actively engage in discussions are crucial for research. At Amolf there are plenty of such people, but I would like to specifically thank Martin, Clara, Lutz, Said, Felipe, Sebastian and Boris for their helpfulness when I stepped in their office to ask about something. Ik heb het een groot plezier gevonden om samen te werken met Sander. Ik ben blij dat we nu samen een project afronden waarvan we ooit dachten dat het in een maand gedaan zou zijn. Als laatste van Amolf wil ik Jorik bedanken. We kennen elkaar uit Utrecht en zijn tegelijk begonnen bij Amolf. Jouw manier van werken heeft altijd een grote indruk op me gemaakt, en als ik vast zat in mijn onderzoek kon ik altijd bij je terecht. Ik ben erg blij dat je mij als paranimf tijdens mijn verdediging bij wilt staan.

Een goede balans tussen onderzoek en ontspanning is natuurlijk erg belangrijk. De wekelijkse trainingen en wedstrijden van volleybal vormden een welkome en gezellige afwisseling van het zitten achter een bureau en het hangen boven een optische tafel in een donker lab. Daarnaast reken ik mij rijk met een vriendengroep die ontstaan is op de middelbare school op Texel en doet het me veel plezier dat Hans, waarmee ik ooit samen aan dezelfde studie ben begonnen, mijn paranimf is. Mijn ouders, zus en broertje hebben mij een kritische houding en nieuwsgierigheid geleerd. Karin, aan jouw steun en vertrouwen heb ik ongelofelijk veel gehad en ik heb veel zin om met jou een nieuw avontuur aan te gaan.

About the author

Born on the 4th of July, 1988, Ruben spent most of his youth on the beautiful island of Texel. After receiving his high school diploma from OSG De Hogeberg, he studied physics at Utrecht University, graduating cum laude in June 2011, with a thesis on optical metamaterials, supervised by Prof. Dr. Albert Polman in the Photonic Materials group in Amsterdam. He continued this project as a PhD researcher in July 2011 in the same group. The results are presented in this thesis. In his free time, Ruben enjoys playing volleyball, cycling, and looking for sunshine with his girlfriend.

The work described in this thesis was performed at the FOM-Institute AMOLF, Science Park 104, 1098 XG Amsterdam, The Netherlands.